

The NANOGrav 12.5 yr Data Set: Observations and Narrowband Timing of 47 Millisecond Pulsars

```
Md F. Alam<sup>1</sup>, Zaven Arzoumanian<sup>2</sup>, Paul T. Baker<sup>3</sup>, Harsha Blumer<sup>4,5</sup>, Keith E. Bohler<sup>6</sup>, Adam Brazier<sup>7</sup>,
            Paul R. Brook<sup>4,5</sup>, Sarah Burke-Spolaor<sup>4,5</sup>, Keeisi Caballero<sup>6</sup>, Richard S. Camuccio<sup>6</sup>, Rachel L. Chamberlain<sup>1</sup>, Shami Chatterjee<sup>7</sup>, James M. Cordes<sup>7</sup>, Neil J. Cornish<sup>8</sup>, Fronefield Crawford<sup>1</sup>, H. Thankful Cromartie<sup>7</sup>,
             Megan E. DeCesar<sup>9,10,40</sup>, Paul B. Demorest<sup>11</sup>, Timothy Dolch<sup>12</sup>, Justin A. Ellis<sup>13</sup>, Robert D. Ferdman<sup>14</sup>,
          Elizabeth C. Ferrara<sup>15</sup>, William Fiore<sup>4,5,16</sup>, Emmanuel Fonseca<sup>17</sup>, Yhamil Garcia<sup>6</sup>, Nathan Garver-Daniels<sup>4,5</sup>, Peter A. Gentile<sup>4,5</sup>, Deborah C. Good<sup>18</sup>, Jordan A. Gusdorff<sup>9</sup>, Daniel Halmrast<sup>12,19</sup>, Jeffrey S. Hazboun<sup>20</sup>,
    Kristina Islo 16, Ross J. Jennings 7, Cody Jessup 8,12, Megan L. Jones 16, Andrew R. Kaiser 4,5, David L. Kaplan 16,
       Luke Zoltan Kelley<sup>21</sup>, Joey Shapiro Key<sup>20</sup>, Michael T. Lam<sup>22,23</sup>, T. Joseph W. Lazio<sup>24</sup>, Duncan R. Lorimer<sup>4,5</sup>,
Luke Zoltan Kelley 1 , Joey Shapiro Key 2 , Michael T. Lam 23. T. Joseph W. Lazio 1, Duncan R. Lorimer 1, Jing Luo 25 , Ryan S. Lynch 26 , Dustin R. Madison 4,5,41 , Kaleb Maraccini 16, Maura A. McLaughlin 4,5 , Chiara M. F. Mingarelli 27,28 , Cherry Ng 29 , Benjamin M. X. Nguyen 1, David J. Nice 9 , Timothy T. Pennucci 30,31,41 , Nihan S. Pol 4,5 , Joshua Ramette 12,32 , Scott M. Ransom 9 , Paul S. Ray 3 , Brent J. Shapiro-Albert 4,5 , Navier Siemens 16,34 , Joseph Simon 4 , Renée Spiewak 5 , Ingrid H. Stairs 18 , Daniel R. Stinebring 3 , Kevin Stovall 11 , Joseph K. Swiggum 9,41 , Stephen R. Taylor 37 , Michael Tripepi 12,38 , Michael Vallisneri 24 , Sarah J. Vigeland 16 ,
                                                                             Caitlin A. Witt<sup>4,5</sup>, and Weiwei Zhu<sup>39</sup>
                                                                                        The NANOGrav Collaboration
                                 <sup>1</sup> Department of Physics and Astronomy, Franklin & Marshall College, P.O. Box 3003, Lancaster, PA 17604, USA
                                     X-Ray Astrophysics Laboratory, NASA Goddard Space Flight Center, Code 662, Greenbelt, MD 20771, USA Department of Physics and Astronomy, Widener University, One University Place, Chester, PA 19013, USA
                                 <sup>4</sup> Department of Physics and Astronomy, West Virginia University, P.O. Box 6315, Morgantown, WV 26506, USA
             <sup>5</sup> Center for Gravitational Waves and Cosmology, West Virginia University, Chestnut Ridge Research Building, Morgantown, WV 26505, USA Center for Advanced Radio Astronomy, University of Texas-Rio Grande Valley, Brownsville, TX 78520, USA
                     <sup>7</sup> Cornell Center for Astrophysics and Planetary Science and Department of Astronomy, Cornell University, Ithaca, NY 14853, USA
                                                             Department of Physics, Montana State University, Bozeman, MT 59717, USA
                                            Department of Physics, Lafayette College, Easton, PA 18042, USA; megan.decesar@nanograv.org

10 George Mason University, Fairfax, VA 22030, USA

    National Radio Astronomy Observatory, 1003 Lopezville Road, Socorro, NM 87801, USA
    Department of Physics, Hillsdale College, 33 E. College Street, Hillsdale, MI 49242, USA
    Infinia ML, 202 Rigsbee Avenue, Durham, NC 27701, USA

                                                              <sup>14</sup> School of Chemistry, University of East Anglia, Norwich, NR4 7TJ, UK
                                                                      NASA Goddard Space Flight Center, Greenbelt, MD 20771, USA
<sup>16</sup> Center for Gravitation, Cosmology and Astrophysics, Department of Physics, University of Wisconsin-Milwaukee, P.O. Box 413, Milwaukee, WI 53201, USA
                                              Department of Physics, McGill University, 3600 University Street, Montreal, QC H3A 2T8, Canada
                    Department of Physics and Astronomy, University of British Columbia, 6224 Agricultural Road, Vancouver, BC V6T 1Z1, Canada 19 Department of Mathematics, University of California, Santa Barbara, CA 93106, USA
                                                    <sup>20</sup> University of Washington Bothell, 18115 Campus Way NE, Bothell, WA 98011, USA
                   <sup>21</sup> Center for Interdisciplinary Exploration and Research in Astrophysics (CIERA), Northwestern University, Evanston, IL 60208, USA
                                               School of Physics and Astronomy, Rochester Institute of Technology, Rochester, NY 14623, USA
                                   23 Laboratory for Multiwavelength Astrophysics, Rochester Institute of Technology, Rochester, NY 14623, USA
                         Laboratory for Multiwavelengin Astrophysics, Rochester Institute of Technology, Rochester, IV 17023, COA

24 Jet Propulsion Laboratory, California Institute of Technology, 4800 Oak Grove Drive, Pasadena, CA 91109, USA

25 Department of Astronomy & Astrophysics, University of Toronto, 50 Saint George Street, Toronto, ON M5S 3H4, Canada

26 Green Bank Observatory, P.O. Box 2, Green Bank, WV 24944, USA
                                  <sup>27</sup> Center for Computational Astrophysics, Flatiron Institute, 162 5th Avenue, New York, New York, 10010, USA
                                 <sup>28</sup> Department of Physics, University of Connecticut, 196 Auditorium Road, U-3046, Storrs, CT 06269-3046, USA
                      <sup>29</sup> Dunlap Institute for Astronomy and Astrophysics, University of Toronto, 50 St. George Street, Toronto, ON M5S 3H4, Canada
                                               <sup>0</sup> National Radio Astronomy Observatory, 520 Edgemont Road, Charlottesville, VA 22903, USA <sup>31</sup> Institute of Physics, Eötvös Loránd University, Pázmány P.s. 1/A, 1117 Budapest, Hungary
                       Department of Physics, Massachusetts Institute of Technology, 77 Massachusetts Avenue, Cambridge, MA 02139-4307, USA

33 Space Science Division, Naval Research Laboratory, Washington, DC 20375-5352, USA

34 Department of Physics, Organ State University, Corpullis, OR 07321, USA
                                                              Department of Physics, Oregon State University, Corvallis, OR 97331, USA
                 35 Centre for Astrophysics and Supercomputing, Swinburne University of Technology, P.O. Box 218, Hawthorn, Victoria 3122, Australia
                                                          Department of Physics and Astronomy, Oberlin College, Oberlin, OH 44074, USA
                                <sup>37</sup> Department of Physics and Astronomy, Vanderbilt University, 2301 Vanderbilt Place, Nashville, TN 37235, USA
                                                            Department of Physics, The Ohio State University, Columbus, OH 43210, USA
      <sup>39</sup> National Astronomical Observatories, Chinese Academy of Science, 20A Datun Road, Chaoyang District, Beijing 100012, People's Republic of China
```

Received 2020 May 13; revised 2020 October 22; accepted 2020 November 2; published 2020 December 21

⁴⁰ Resident at US Naval Research Laboratory, Washington, DC 20375, USA.

⁴¹ NANOGrav Physics Frontiers Center Postdoctoral Fellow.

Abstract

We present time-of-arrival (TOA) measurements and timing models of 47 millisecond pulsars observed from 2004 to 2017 at the Arecibo Observatory and the Green Bank Telescope by the North American Nanohertz Observatory for Gravitational Waves (NANOGrav). The observing cadence was three to four weeks for most pulsars over most of this time span, with weekly observations of six sources. These data were collected for use in low-frequency gravitational wave searches and for other astrophysical purposes. We detail our observational methods and present a set of TOA measurements, based on "narrowband" analysis, in which many TOAs are calculated within narrow radio-frequency bands for data collected simultaneously across a wide bandwidth. A separate set of "wideband" TOAs will be presented in a companion paper. We detail a number of methodological changes, compared to our previous work, which yield a cleaner and more uniformly processed data set. Our timing models include several new astrometric and binary pulsar measurements, including previously unpublished values for the parallaxes of PSRs J1832-0836 and J2322+2057, the secular derivatives of the projected semimajor orbital axes of PSRs J0613-0200 and J2229+2643, and the first detection of the Shapiro delay in PSR J2145-0750. We report detectable levels of red noise in the time series for 14 pulsars. As a check on timing model reliability, we investigate the stability of astrometric parameters across data sets of different lengths. We also report flux density measurements for all pulsars observed. Searches for stochastic and continuous gravitational waves using these data will be subjects of forthcoming publications.

Unified Astronomy Thesaurus concepts: Millisecond pulsars (1062); Pulsar timing method (1305); Radio pulsars (1353); Pulsars (1306); Gravitational waves (678); Binary pulsars (153); Astrometry (80); Astronomy databases (83); Radio astronomy (1338); Rotation powered pulsars (1408); Time series analysis (1916); Flux calibration (544)

1. Introduction

High-precision timing of millisecond pulsars (MSPs) produces a wealth of both astrophysics and basic physics, including strong constraints on the dense matter equation of state (e.g., Lattimer 2019), unique tests of theories of gravity (e.g., Renevey 2019), and the potential to soon detect nanohertz-frequency gravitational waves (e.g., Taylor et al. 2016; Perrodin & Sesana 2018). The North American Nanohertz Observatory for Gravitational Waves (NANOGrav; Ransom et al. 2019) is a collaboration pursuing long-term goals of detecting and characterizing gravitational waves using the timing data from an array of high-precision MSPs (a.k.a. a pulsar timing array or PTA). Such efforts promise a wide variety of astrophysical results at virtually all scales from the solar system to the cosmological (e.g., Burke-Spolaor et al. 2019).

This paper describes the current public release of NANO-Grav data, the "12.5 yr Data Set," which we have collected over 12.5 yr (2004 July to 2017 June) using the Arecibo Observatory and the Green Bank Telescope. The data and analyses described here are built on and extend those found in our previous data releases for our 5 yr (Demorest et al. 2013, herein NG5), 9 yr (Arzoumanian et al. 2015, herein NG9), and 11 yr (Arzoumanian et al. 2018b, herein NG11) data sets. The present release includes data from 47 MSPs.

We have taken two approaches to measuring pulse arrival times in the 12.5 yr data set, which we report in two separate papers. In the present paper, we follow the procedures of our earlier data sets: we divide our observations made across wide radio-frequency bands into narrow-frequency subbands and determine pulse times of arrival (TOAs) for each subband, resulting in a large number of measurements ("narrowband TOAs") for each observation. An alternative approach, wideband timing (Liu et al. 2014; Pennucci et al. 2014; Pennucci 2019), extracts a single TOA and dispersion measure (DM) for each observation, resulting in a more compact data set of "wideband TOAs." We analyze the 12.5 yr data set using wideband timing in Alam et al. (2020).

Analyses to search the 12.5 yr data set for signals indicative of gravitational waves will be presented elsewhere. Analyses of our previous-generation data set, NG11, for stochastic, continuous, and bursting gravitational waves can be found in Arzoumanian et al. (2018a), and Aggarwal et al. (2019, 2020), respectively.

NANOGrav is part of the International Pulsar Timing Array (IPTA; Hobbs et al. 2010), and the 12.5 yr data set will become part of a future IPTA data release (Perera et al. 2019) along with data from the European Pulsar Timing Array (Desvignes et al. 2016) and the Parkes Pulsar Timing Array (PPTA; Kerr et al. 2020).

The plan for this paper is as follows. In Section 2, we describe the observations and data reduction. In Section 3, we describe timing models fit to the TOAs for each pulsar, including both deterministic astrophysical phenomena and stochastic noise terms. In Section 4, we compare timing models generated with the longstanding TEMPO⁴² pulsar timing software package with those generated using the new PINT⁴³ package (Luo et al. 2019, 2020). We list astrometric and binary parameters that have been newly measured with NANOGrav data in Section 5. In Section 6, we compare astrometric measurements between the present paper and previous data sets. In Section 7, we highlight five binary pulsars for which new post-Keplerian parameters have been measured or for which extensive testing was needed to obtain their timing solution. In Section 8, we present flux density measurements for each pulsar at two or more radio frequencies. In Section 9, we summarize the work. In the Appendix, we present the timing residuals and DM variations for all pulsars in this data set.

The NANOGrav 12.5 yr data set files include narrowband TOAs developed in the present paper, wideband TOAs developed in Alam et al. (2020), parameterized timing models for all pulsars for each of the TOA sets, and supporting files such as telescope clock offset measurements. The data set

https://github.com/nanograv/tempo

⁴³ https://github.com/nanograv/PINT

presented in the present paper has been preserved on Zenodo at doi:10.5281/zenodo.4312297.44

2. Observations, Data Reduction, and Times of Arrival

Here we describe the telescope observations and data reduction used to produce our "narrowband" TOA data set. The procedures we used are nearly identical to those in NG9 and NG11. We therefore provide only a brief overview of analysis details that were fully presented in NG9 and NG11, noting changes from those procedures where applicable. The "wideband" TOAs contained within our data set use intermediate data products resulting from the procedures described in the subsections below but use a different TOA calculation algorithm as described in Alam et al. (2020).

2.1. Data Collection

The data presented here were collected between 2004 July through 2017 June. Timing baselines of individual pulsars range from 2.3 to 12.9 yr. Compared to NG11, this data set adds 1.5 yr of data and two MSPs: J1946+3417 and J2322 +2057. The sources and observing epochs are summarized in Figure 1.

Data were collected at the 305 m Arecibo Observatory (Arecibo or AO) and the 100 m Robert C. Byrd Green Bank Telescope (GBT). Twenty-six pulsars were observed with Arecibo. These include all pulsars in our program within the Arecibo decl. range of $0^{\circ} < \delta < +39^{\circ}$. Twenty-three pulsars were observed with the GBT. This includes all pulsars in our program outside the Arecibo decl. range, along with two pulsars also observed with Arecibo, PSRs J1713+0747 and B1937+21, for which we have continuous data sets at both telescopes for the length of the observing program. All sources were observed with an approximately three-week cadence at Arecibo or four-week cadence at the GBT (herein referred to as "monthly" observations). In addition, six sources were observed weekly to increase sensitivity to continuous waves from individual foreground GW sources (Arzoumanian et al. 2014): PSRs J0030+0451, J1640+2224, J1713+0747, J1909 -3744, J2043+1711, and J2317+1439 (herein referred to as "high-cadence" observations). For each pulsar in the highcadence program, the observations were taken at the same telescope using the same methodologies as for the monthly observations, with the exception of the weekly GBT data, which covered only the 1.4 GHz frequency band.

Some interruptions in the data sets are evident in Figure 1. The most prominent of these were caused by telescope painting at Arecibo (2007), earthquake damage at Arecibo (2014), and azimuth track refurbishment at the GBT (2007).

With few exceptions, each pulsar at each epoch was observed with at least two receivers widely separated in observing frequency in order to measure and remove interstellar propagation effects, including variations in DM (Section 3.2). Such multireceiver observations were made on the same day at Arecibo or within a few days at the GBT. Exceptions to the two-receiver convention were made for the high-cadence GBT observations and for occasions at either

telescope when a receiver was not available for technical reasons. Our criteria for using such data are described in Section 2.5.

Telescope receivers and data collection systems employed for this project are described in Table 1 of NG9. At the GBT, we used both the 820 MHz and 1.4 GHz receivers for monthly observations, but only the 1.4 GHz receiver for the high-cadence observations. At Arecibo, all sources were observed with the 1.4 GHz receiver and a second receiver, either 430 MHz or 2.1 GHz, with the choice of receiver based on the pulsar's spectral index and timing precision in each frequency band. Some pulsars that were initially observed with 430 MHz were later moved to 2.1 GHz, or vice versa, due to additional evaluation finding that a given pulsar is better timed at one frequency or the other. One pulsar, PSR J2317 +1439, was initially observed at 327 and 430 MHz, but it is now observed at 430 MHz and 1.4 GHz, and no other use of the 327 MHz receiver has been made.

Two generations of back-end instrumentation were used for data collection. The ASP and GASP systems (64 MHz of bandwidth; Demorest 2007) at Arecibo and the GBT, respectively, were used for approximately the first six years of NANOGrav data acquisition. We transitioned to PUPPI (at Arecibo) and GUPPI (at Green Bank) in 2012 and 2010, respectively. PUPPI and GUPPI have been used for all subsequent data collection, including all new data in the present paper. They can process up to 800 MHz bandwidths (DuPlain et al. 2008; Ford et al. 2010) and significantly improved our timing precision relative to ASP and GASP. During the transition from ASP/GASP to PUPPI/GUPPI, we made precise measurements of the time offsets between the instruments (Appendix A of NG9). We continue to use the offset measurements from NG9.

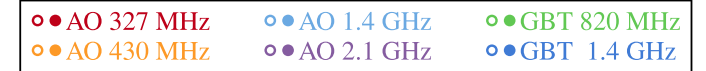
These instruments divide the telescope passband into narrow spectral channels, undertake coherent dedispersion of the signals within each channel, evaluate self- and cross-products to enable recovery of four Stokes parameters, and fold the resulting time series in real time using a nominal pulsar timing model. Thus, the raw data are in the form of folded pulse profiles as a function of time, radio frequency, and polarization. The raw profiles have 2048 phase bins, a frequency resolution of 4 MHz (ASP/GASP) or 1.5 MHz (GUPPI/PUPPI), and subintegrations of 1 s (PUPPI at 1.4 and 2.1 GHz) or 10 s (all other receiver/back-end combinations).

Observations were calibrated in two steps. Prior to each pulsar observation, we inject a pulsed-noise signal into the receiver path for use in calibrating the signal amplitudes. The pulsed-noise signals, in turn, are calibrated approximately monthly via a series of on- and off-source observations on an unpolarized continuum radio source of known flux density. Details of the continuum source are given in Section 8.

2.2. ASP/GASP Times of Arrival

We collected data using the ASP and GASP instruments through 2012 and 2010, respectively. There are no new ASP/GASP data in this data release. For these data, we used TOAs generated in NG9 without modification. These TOAs were computed using procedures similar to those for PUPPI/GUPPI data described below. The ASP/GASP TOAs incorporate time offsets relative to the PUPPI/GUPPI instruments as described in NG9.

⁴⁴ All of NANOGrav's data sets are available at http://data.nanograv.org, including the data set presented here, which is the "v4" version of the 12.5 yr data set. Raw telescope data products are also available from the same website. Version "v4" of the 12.5 yr data set has also been preserved on Zenodo at doi:10.5281/zenodo.4312297.



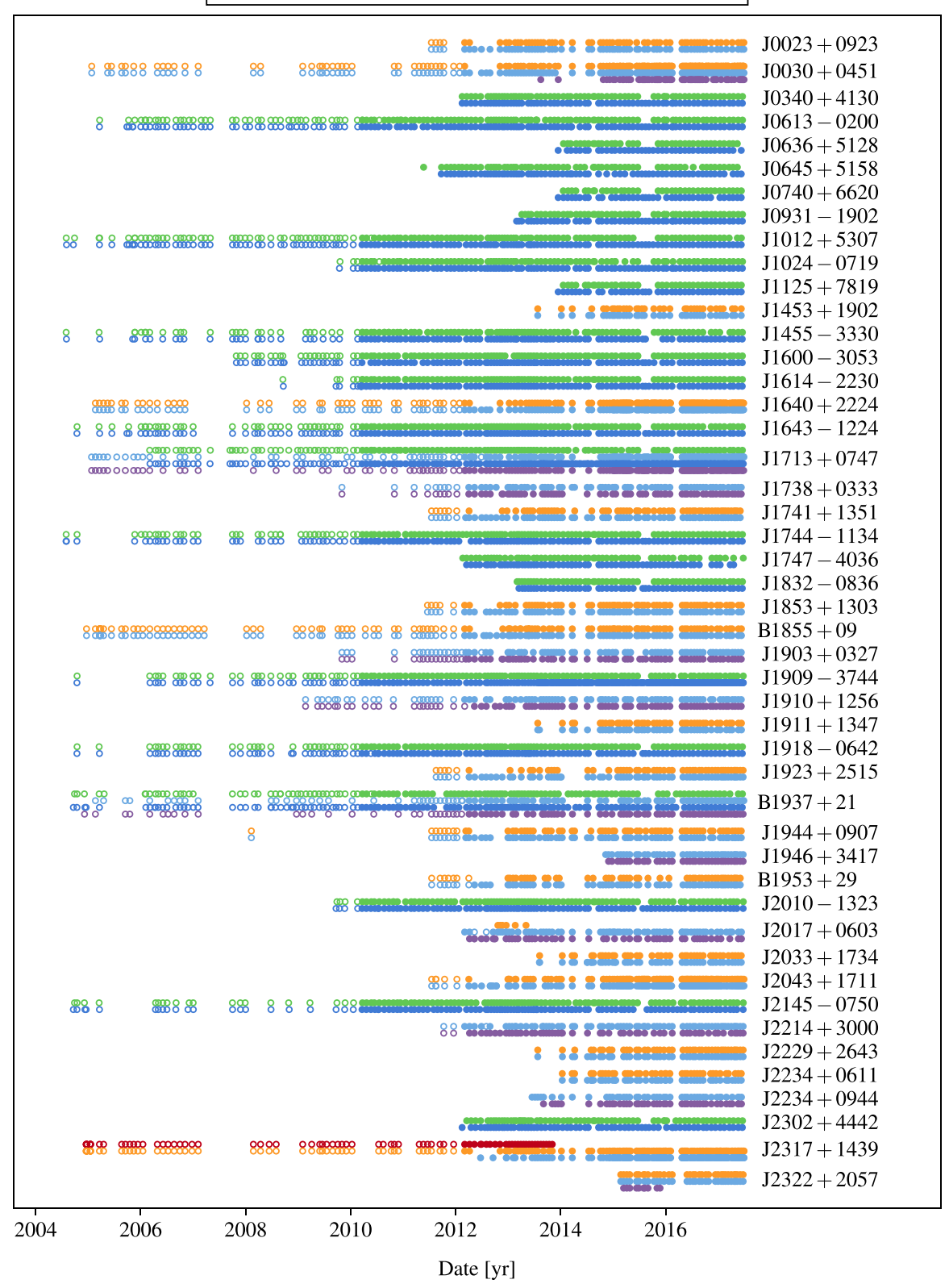


Figure 1. Epochs of all observations in the data set. The observatory and observing frequency are indicated by color: Arecibo observations are red (327 MHz), orange (430 MHz), light blue (1.4 GHz), and purple (2.1 GHz). GBT observations are green (820 MHz) and dark blue (1.4 GHz). The data acquisition system is indicated by symbol: open circles are ASP or GASP, and filled circles are PUPPI or GUPPI.

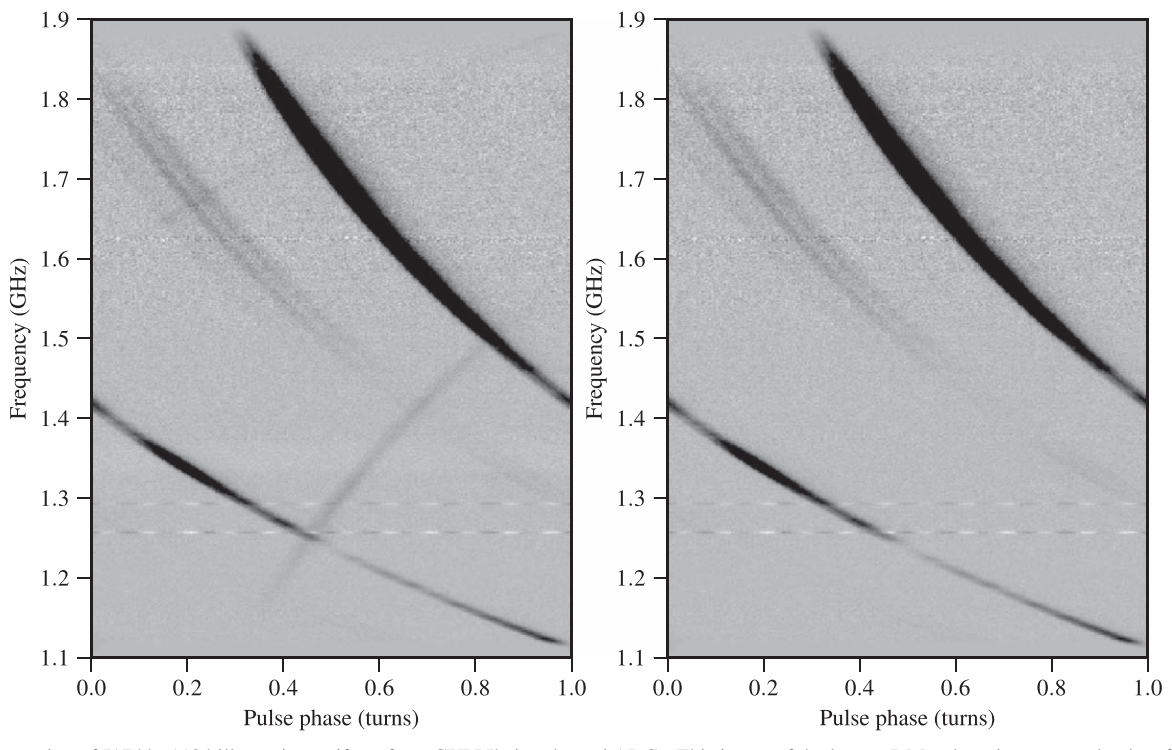


Figure 2. Observation of J1744+1134 illustrating artifacts from GUPPI's interleaved ADCs. This is one of the lowest-DM pulsars in our sample; therefore, the effect is easily visible. Dispersion has not been removed, so the true pulsar signal arrives earlier at higher radio frequencies. The image artifact can be seen as the faint, apparently negatively dispersed, signal "reflected" about the band center frequency of 1.5 GHz. No interference excision has been applied to these data; the spurious narrowband signals visible between 1.2 and 1.3 GHz are RFI. The plot color scale has been saturated at 10% of the maximum data value. The left panel shows the raw data, while the right panel shows the same data after the correction procedure has been applied.

During the transition between the ASP/GASP and PUPPI/GUPPI instruments, parallel data were collected on two instruments, resulting in two (redundant) sets of TOAs. In these situations, we use only the PUPPI/GUPPI TOAs, but we retain the commented-out ASP/GASP TOAs in the data set, flagging these TOAs in a method similar to the cut TOAs described in Section 2.5.

2.3. PUPPI/GUPPI Data Reduction

In this section, we describe the processing of PUPPI/GUPPI folded pulse profiles described above to remove various artifacts, to calibrate the data amplitudes, and to produce more compact data sets which were then used for TOA generation.

2.3.1. Artifact Removal

GUPPI and PUPPI employ an interleaved analog-to-digital conversion (ADC) scheme to achieve their wide bandwidths. Rather than a single ADC running at the Nyquist sampling rate of 2B (for a bandwidth B), two converters are running in parallel at rate B, offset in time from each other by half a cycle. If the gain of the two converters is not identical, or if there is a timing skew such that the time offset is not exactly $(2B)^{-1}$, an image rejection artifact will appear in the data. This looks like a copy of the input signal, frequency-reversed about the center of the sampled band (Figure 2, left panel). For pulsar data, this artifact appears negatively dispersed and therefore can be distinguished from most typical radio-frequency interference (RFI). The amplitude of the image signal depends on the magnitude of the gain mismatch or timing skew. Gain mismatch results in a constant image ratio versus frequency, while the ratio from the timing skew increases with frequency

within the sampled band. Kurosawa et al. (2001) present a detailed analysis of this effect in interleaved sampler systems and derive analytic expressions for the ratio of image to true signal as a function of the mismatch parameters.

If not corrected, the presence of these artifacts will result in a frequency-dependent systematic TOA bias. The effect is largest at those points in the band where the image pulse crosses the true pulse. Low-DM, slow-spinning pulsars with wide pulse profile shapes are the most affected, while for high-DM sources, dispersion will smear out the image relative to the pulsar signal within each channel, reducing its impact. For J2145-0750, a 1% image ratio could shift some individual channel TOAs by up to 1 μ s, while for J1909–3744, the effect is 40 ns and confined to smaller parts of the band. On average, this effect will cancel out when averaged over the full wide band, with equal amounts of positively and negatively shifted channels; however, this depends on the details of bandpass shape and scintillation pattern. In NG11 and previous data sets, there was no effort to mitigate these images. In the present work, we introduce a new procedure to remove the images.

Using data from several bright pulsars in our sample, we measured the relative amplitudes of the pulsar and image signals as a function of frequency, bandwidth, and observing epoch. We find that the observed effect is consistent with a pure timing skew, with a typical value of $\sim 30 \, \mathrm{ps}$. This results in image ratios ranging from 0.5% to 4% across the band. The timing skew values are consistent between pulsars for a given back-end setup. The values vary with time, showing occasional step-like changes at dates corresponding to known maintenance procedures such as replacement of a faulty ADC board or synthesizer. Based on this observed behavior, we developed a

piecewise constant in time model for the skew value that can be used to correct the data.

With the known skew values, we calculate the image ratio as a function of frequency following Kurosawa et al. (2001). For all input data, we apply this ratio to a frequency-reversed copy of the data and subtract the result, giving a corrected data set (Figure 2, right-hand panel). Based on the scatter of the measured skew values, we conservatively estimate that this correction is good to at least the 10% level, therefore reducing image artifacts by one order of magnitude.

This procedure relies on having data measured continuously across the full sampled bandwidth, as normally was the case in our observations. However, in the PUPPI data set occasional instrumental failures resulted in portions of the band not being recorded. In these cases, it is not possible to apply the correction to the corresponding subband "mirrored" about the band center. Nevertheless, we elected to include such data in the data set. In the TOA-flagging system described below, TOAs generated from such data are marked using the <code>-imguncorr</code> flag.

2.3.2. Calibration and Integration in Time and Frequency

After removing artifact images, we performed standard data reduction procedures as described in NG11, with one additional step of excising RFI from the calibration files as well as from the data files; this additional step led to improvements in TOA measurements, especially at 2.1 GHz with PUPPI. The remaining steps of calibrating, reducing, and excising RFI from the data were the same as in NG11. Data were frequency-averaged into channels with bandwidths between 1.5 and 12.5 MHz, depending on the receiver. We time-averaged the calibrated and cleaned profiles into subintegrations up to 30 minutes in length, except in the few cases of binary pulsars with very short orbital periods; in those cases, we averaged the data into subintegrations no longer in duration than 2.5% of the orbital period in order to maintain time resolution over the orbit.

2.4. PUPPI/GUPPI Time-of-arrival Generation

We generally followed the methods described in NG9 and NG11 to calculate narrowband TOAs, but with an improved algorithm to calculate TOA uncertainties. The uncertainties were calculated by numerical integration of the TOA probability distribution presented in Equation (12) of NG9, Appendix B. This mitigates the underestimation of uncertainties calculated by conventional methods in the low-signal-to-noise regime.

We used previously generated template pulse profiles for the 45 pulsars from NG11, generating new templates only for the two pulsars newly added to this data set. To make the template profiles, we iteratively aligned and averaged together the reduced data profiles and applied wavelet smoothing to the final average profile. With these templates, we measured TOAs from the reduced GUPPI and PUPPI profiles, and collated them with the existing GASP and ASP TOAs from NG9.

2.5. Cleaning the Data Set for Improved Data Quality

Calculated TOAs can be biased by a variety of observational problems, including imperfections in instrumentation, flawed calibration, RFI, or other nonastrophysical influences. In past data releases, we have ensured a high level of data quality by

systematically removing RFI, excluding low-signal-to-noise ratio (S/N) TOAs (see details in NG9), removing outliers identified by Bayesian analysis of residuals (see details in NG11), and manual inspection of the data sets. These same procedures were carried out for the present data set, along with a series of new cleaning techniques described below.

The remainder of this section details these quality-control measures, which led to the removal of uninformative or suspect TOAs, as well as entire observations in some cases. The data quality analysis steps were typically iterative in nature. For example, the "bad DMX range" criterion described below was rechecked after any change in the data set made for other reasons.

All TOAs removed by these procedures are included in the data set files. They are marked as comments in the TOA files, and each excluded TOA includes a flag indicating the reason for its exclusion. The exclusion methods, flags, and statistics of removed TOAs are summarized in Table 1. After all TOA cutting was complete, the final narrowband data set had 415,173 TOAs.

2.5.1. Signal-to-noise Ratio Cut

As in NG9 and NG11, we removed TOAs that were generated from pulse profiles with S/N < 8. These TOAs contain little information and, at the very lowest S/N values, can be miscalculated due to the dominance of noise over any pulsar signal that is present. We maintained this S/N cutoff in the present work.

2.5.2. Bad DM Range Cut

As detailed in Section 3.2, our timing models include a stepwise model for variation in DM, in which DM is allowed to have independently varying values in time intervals. The time intervals range in length from 0.5 to 15 days, depending on the telescope and instrumentation. In order to achieve DM measurements of reasonable precision, we require that the maximum-to-minimum frequency ratio of TOAs with each of these time ranges satisfies $\nu_{\rm max}/\nu_{\rm min} > 1.1$. Data within any DM time range that did not meet this criterion were removed.

As with NG11, this criterion led to the removal of some data that had been incorporated in NG9, in particular lengthy subsets of single-receiver data from a few pulsars initially observed as part of a non-NANOGrav timing program and later merged into our data set.

2.5.3. Outlier TOA Cut

We used the automated outlier-identification algorithm of Vallisneri & van Haasteren (2017) to estimate the probability $p_{i,\text{out}}$ that each individual TOA is an outlier, based on the initial 12.5 yr timing models. The $p_{i,\text{out}}$ are defined in Equation (6) of Vallisneri & van Haasteren, where Equations (1)–(5) provide definitions of the parameters in Equation (6). The $p_{i,\text{out}}$ estimate is fully consistent with the Bayesian inference of all noise parameters of the pulsar being analyzed. As in NG11, we removed all TOAs with $p_{i,\text{out}} > 0.1$, resulting in a total of 1,022 TOAs being removed from the full 12.5 yr data set. This outlier probability threshold was chosen based on the

⁴⁵ We note that this outlier analysis step was incorporated as an additional step toward the end of the pipeline in NG11, after the TOA sets had already been manually edited. For the current data set, we followed the S/N thresholding step with this outlier analysis and only later manually edited the TOA data set.

Table 1
TOA Removal Methods

Flag	No. of TOAs Removed	Reason for TOA Removal	Notes (Including Differences with the Wideband Data Set Procedures)
-cut snr	92,290	(Section 2.5.1) Profile data used to generate TOA does not meet the signal-to-noise ratio threshold	S/N < 8 for narrowband TOAs, $S/N < 25$ for wideband TOAs
-cut badepoch	11,650	(Sections 2.5.4, 2.5.5, 2.5.6) Observation is significantly corrupted by instrumentation issues or RFI	Identified by human inspection; these observations are not included in the wideband data set
-cut dmx	10,874	(Section 2.5.2) Ratio of maximum to minimum frequency in an observing epoch (in a single DMX bin) $\nu_{\rm max}/\nu_{\rm min} < 1.1$	$\nu_{\rm max}$ and $\nu_{\rm min}$ are TOA reference frequencies in the narrowband data set and are separately calculated for each TOA in the wideband data set
-cut simul	5194	(Section 2.2) ASP/GASP TOA acquired at the same time as a PUPPI/ GUPPI TOA	Removed at the last stage of analysis from both narrowband and wideband data sets
-cut epochdrop	2384	(Section 2.5.7) Entire epoch removed based on F test $p < 10^{-6}$	Epochs identified in the narrowband data set analysis are also removed from the wideband data set
-cut outlier10	1022	(Section 2.5.3) TOA has outlier probability $p_{i,\text{out}} > 0.1$	This particular outlier analysis applies only to the narrowband data set
-cut orphaned	490	(Section 2.5.9) Insignificant data volume	A small number of TOAs originate from test observations in different receiver bands; these observations are not included in the wideband data set
-cut manual	70	(Section 2.5.8) The TOAs corresponding to individual pulse profiles are corrupted by instrumentation or RFI, but were not identified and removed via S/N threshold or outlier probability cuts	Identified by human inspection; both narrowband and wideband data sets have a small volume of manually excised TOAs, but they were determined independently

Note. The flags are listed here in order of the number of narrowband TOAs that were removed from the data set via each method. All cut TOAs are provided as commented-out TOAs in the ASCII-text TOA files; excluding these, there are 415,173 narrowband TOAs in the data set.

inspection of a subset of pulsars, from which we found that $p_{i,\text{out}}$ has an extremely bimodal distribution: nearly all TOAs had $p_{i,\text{out}} < 0.1$ or $p_{i,\text{out}} > 0.9$. The $p_{i,\text{out}} > 0.1$ threshold for TOA removal is thus empirically motivated and additionally remains consistent with the threshold used in NG11.

We note that the outlier analysis was not run iteratively as timing models were updated. Such an iterative procedure was tested on several pulsars, and it was found that the updated outlier results had very minor, if any, differences from the original outlier results. This finding is likely explained by the fact that the results of the outlier runs are already marginalized over the linearized timing model parameters, with very large priors. Thus, a different set of outliers from a subsequent analysis would only be expected if the original outliers had taken the timing model outside its linear range, or if so many data points were excluded after the initial analysis that the noise profile changed and new, previously obscured outliers were revealed. Based on our empirical findings from the iterative outlier analysis runs on a subset of pulsars, and on this theoretical explanation, we chose to only run the outlier analysis once at the beginning of the timing analysis for the full data set.

2.5.4. Manual Removal of Individual Observations Guided by Outlier TOAs

The outlier analysis was used as a guide in identifying observing epochs in which most or all TOAs may have been corrupted by instrumentation issues or by excessive RFI. If a single observation had more than five TOAs with $p_{i,\text{out}} > 0.1$, we reviewed the corresponding observing log and examined the data manually to determine if there were instrumental problems or RFI that rendered the observation unusable. In such cases, all TOAs from the affected observations were removed.

2.5.5. Corrupt Calibration Cut

As described above, pulsar observations were preceded by measurements using an artificial pulsed-noise signal injected in the telescope signal path, and the same pulsed-noise-signal method was used during continuum calibrator observations. We searched for anomalies in the pulsed-noise-signal measurements; these could result from instrumentation failures or from use of incorrect noise signals in an individual observation.

The following are specific anomalies that were identified in the calibration files. (1) A pulsed-noise amplitude that was unusually high or low (88 affected observations). (2) Crosspolarization flux calibration amplitudes deviating significantly from the mean locus of amplitudes for a given receiver/backend combination (65 observations affected and removed, due to corrupted continuum source observations on MJDs 57229 and 57249). (3) Pulsed calibrator phase not smoothly varying with frequency (one observation was removed solely for this reason, but this was also seen in observations flagged for other reasons). (4) Polarization fraction, $f_{UV} = [(U^2 + V^2)/I^2]^{1/2}$, deviating from expected values. For pulsars with high intrinsic polarization ($f_{UV} \sim 1$), a small number of observations had significantly lower estimated \hat{f}_{UV} values (typically $\hat{f}_{UV} < 0.3$) that signified corrupted data, and a small number of profiles had $f_{UV} > 1$, suggesting a problem with the digitization levels (23) affected observations).

2.5.6. Flux Measurement Cut

Extremely high or low apparent flux density values can result from incorrect calibration or digitization levels. We therefore searched for outlier flux densities as a proxy for calibration errors not detected through the means listed above. We manually examined such observations and removed them as needed. Only one observation was identified and removed by this method, but this analysis informed the development of our other quality-check methods. A detailed flux density analysis is in Section 8.

2.5.7. Epoch F-test Cut

We tested for the presence of otherwise-undetected bad data for each pulsar by removing data from one observing epoch at a time and examining its impact on the timing residuals. This method is effectively an outlier analysis for full observing epochs rather than for individual TOAs. We compared the chisquare of the timing residuals before and after data removal, χ_0^2 and χ^2 , respectively, using an F statistic,

$$F = \frac{(\chi_0^2 - \chi^2)/(n_0 - n)}{(\chi^2/n)},\tag{1}$$

where n_0 and n are the number of degrees of freedom in the original and epoch-removed analyses. We removed data for epochs for which the F test reported a chance probability $p < 10^{-6}$ ($\sim 5\sigma$). This process was run iteratively. We examined the profiles and calibration files for a subset of the observations that were flagged in this way and found that a majority of these observations were faulty in obvious ways (calibration errors, extreme RFI, etc.).

2.5.8. Manual TOA Cut

After completing the above data quality checks, uninformative or outlying TOAs were still present in the data sets of some pulsars. A total of 70 additional TOAs were removed after visual inspection. These were TOAs whose timing residuals appeared to be outliers but were not flagged by the outlier analysis (typically a small number of pulse profiles had been corrupted by narrow-frequency RFI, such that TOAs in a subset of the full bandwidth had to be removed but the rest of the profile or epoch was not adversely affected) or TOAs with very large uncertainties and large timing residuals (usually resulting from a low-S/N TOA measurement, just above our cutoff threshold, or RFI).

2.5.9. Orphan Data Cut

For a few pulsars, in addition to the receivers normally used for observations, a small number of observations were made with a different receiver, typically for testing purposes near the start of observations of this source. We cut such TOAs in the same manner as data that were cut for other reasons.

2.5.10. Wideband TOA Residual Check

We note that for the methods described above, in some cases it was difficult to determine if data were corrupted (e.g., the residuals from a given epoch may have been larger than expected, but no evidence of an issue with the calibration or profile data was found upon inspection). In those cases, we also examined the residual profiles generated from fitting wideband

TOAs, which use high-fidelity, evolving profile models in the matched-template algorithm. For example, the residual profile may reveal that the evolving profile model did not adequately represent the profile during that observation, suggesting a problem with the data that was not found using other methods. Inspection of the wideband residual profiles thus aided in identifying and removing more corrupted data in the narrowband data set. Using the evolving profile models as a means to identify corrupted data profiles is an ongoing development.

3. Timing Analysis

The cleaned TOA data set for each pulsar was fit with a physical timing model, with the TEMPO timing software used for the primary analysis. The timing models were checked using the TEMPO2⁴⁶ and PINT⁴⁷ packages. PINT (Luo et al. 2019, 2020) was developed independently of TEMPO and TEMPO2 and thus provides a particularly robust independent check of the timing models (Section 4). Our expectation is to transition to PINT as the primary timing software for future data sets due to its modularity and its use of modern programming tools, including coding in Python.

An overarching development in the current release is our use of standardized and automated timing procedures. In previous NANOGrav data releases, two core portions of the data analysis were already automated: data reduction (calibration, RFI removal, time- and frequency-averaging) and TOA generation, all of which was done using nanopipe⁴⁸ (Demorest 2018); and checking for timing parameter significance (e.g., as in NG11). For the 12.5 yr data set, we standardized and automated the timing procedure using Jupyter notebooks. These notebooks did not replace the often iterative nature of pulsar timing. Rather, once a reasonable timing solution was found for a pulsar, it was input into the notebook, which ran through an entire standard analysis that included checking for parameter significance (Section 3.1) and performing noise modeling (Section 3.3). This process allowed for systematic and transparent addition or removal of timing and noise parameters, and ensured that the final timing models were assembled in a standardized way. Additional benefits of automating the timing analysis in this way are that it makes NANOGrav timing analysis more accessible to new students or researchers, and much of the automated process can also be applied to other (non-PTA) pulsar timing work.

3.1. Timing Models and Parameters

Timing fits were done using the JPL DE436 solar system ephemeris and the TT(BIPM2017) timescale. As in previous releases, we used a standard procedure to determine which parameters are included in each pulsar's timing model. Always included as free parameters were the intrinsic spin and spin-down rate, and five astrometric parameters (two position parameters, two proper motion parameters, and parallax), regardless of measurement significance. We used ecliptic coordinates for all astrometric parameters to minimize parameter covariances. For binary pulsars, five Keplerian parameters were also always fit: (i) the orbital period (P_b) or orbital frequency (F_b), (ii) the projected semimajor axis (x), and (iii)–(v) either the eccentricity (e), longitude of periastron (ω), and

epoch of periastron passage (T_0) , or two Laplace-Lagrange parameters (ϵ_1, ϵ_2) and the epoch of the ascending node (T_{asc}) .

The particular binary model chosen was based on orbital characteristics, including the presence of post-Keplerian parameters. For low-eccentricity orbits, we used the ELL1 model, which approximates the orbit using the Laplace-Lagrange parameterization of the eccentricity with ϵ_1 and ϵ_2 (Lange et al. 2001). In all cases in which we used ELL1, the model deviated from a more precise timing model by at most 25 ns at any point in the orbit. The pulsars in this data set that satisfy this criterion for the use of the ELL1 model all have $e < 10^{-5}$, although we did not apply an explicit eccentricity criterion for this binary model. If Shapiro delay was marginally present in a low-eccentricity system, we used ELL1H, which incorporates the orthometric parameterization of the Shapiro delay (Freire & Wex 2010) into the ELL1 model; note that the ELL1H model employs the h_3 and h_4 parameters, as opposed to h_3 and $\varsigma = h_4/h_3$ of the DDFWHE model (Freire & Wex 2010; Weisberg & Huang 2016), which is for high-eccentricity systems and is not used in any timing models in this data set. For pulsars with higher eccentricity, we used the DD binary model (Damour & Deruelle 1985, 1986; Damour & Taylor 1992), and for PSR J1713+0747, we used DDK (Kopeikin 1995, 1996), which allows us to measure annual orbital parallax. For PSR J1713+0747, a TEMPO2-compatible timing model that uses the T2 binary model instead of DDK is also included in the data release. For some short-period binaries ($P_b \lesssim 0.5$ days), we used orbital frequency and one or more orbital frequency derivatives, rather than the period and period derivative, to better describe the orbit and allow for simple testing of additional orbital frequency derivatives.

We determined parameter significance via an F test, with the requirement that p < 0.0027 ($\sim 3\sigma$) for a parameter to be included in the timing model. This requirement does not apply to the five astrometric and five Keplerian binary parameters that are always included in the fit (for very low-eccentricity binaries, the eccentricity parameters ϵ_1 and ϵ_2 may not be measured at a significant level for many years). We specifically tested for the significance of additional frequency-dependent pulse shape or evolution parameters ("FD" parameters; see NG9). We allowed FD1 through FD5 to be fit and require that all FD parameters up to the highest-order significant FD parameter be included in the fit, even if the lower-order parameters are not found to be significant. For example, if FD4 is significant but FD3 is not, then FD3 would still be included in the timing model.

For binary pulsars, we tested for the secular evolution of binary parameters (e.g., \dot{x} , $\dot{\omega}$, or \dot{P}_b), higher-order orbital frequency derivatives if using orbital frequency rather than period, and Shapiro-delay parameters. For binaries modeled by ELL1 without previously measured Shapiro-delay parameters, we converted the binary model to ELL1H and tested the significance of h_3 and h_4 . If both h_3 and h_4 were significant, it raised the possibility of measuring the traditional Shapiro-delay parameters (orbital inclination i and companion mass m_c) directly from the timing model fit. Thus, for pulsars with significant detections of h_3 and h_4 , we also tested the use of the traditional Shapiro-delay parameters with the ELL1 model: if i and m_c converged to physically meaningful and significantly measured values, and if the use of these parameters significantly improved the fit according to a $\Delta \chi^2$ test, then we included i and m_c in the timing model; otherwise, we

https://bitbucket.org/psrsoft/tempo2

⁴⁷ See https://github.com/nanograv/PINT and Luo et al. (2019).

⁴⁸ https://github.com/demorest/nanopipe

continued to use h_3 and h_4 . Compared with NG11, these significance tests resulted in the inclusion of one or more new binary parameters for 19 pulsars, and the exclusion of previously included parameters for 3 pulsars (Section 5).

Constant phase "jumps" were included as fit parameters to account for unknown offsets between data subsets collected with different receivers and/or telescopes. For data subsets collected with the same receiver and telescope but different back-end instruments, the measured offsets between GASP and GUPPI, and ASP and PUPPI, from NG9 are included in the TOA data set (with flag "-to" on the TOA lines) rather than in the timing model.

We included white- and red-noise models as described in Section 3.3. We derived best-fit timing model parameter values using a generalized-least-squares fit that uses the noise-model covariance. It is important that the noise model be included when testing for parameter significance, especially if a pulsar shows significant red noise; for several pulsars, one or more parameters were found to be significant when TEMPO was run without generalized-least-squares fitting, but were no longer significant when the noise model was included. Thus, the *F*-test significance tests described above were always performed with generalized-least-squares fitting.

A summary of TOA statistics, basic timing parameters, noise parameters, and other statistics are provided in Tables 2 and 3.

3.2. Dispersion Measure Variations

Variations in dispersion measure are caused by the relative motion of the Earth-pulsar sightline through the ionized interstellar medium (IISM) as well as the Earth's motion through the ionized solar wind and lead to variations in pulse arrival times. It is therefore necessary to include short-timescale DM variations in the timing model (Jones et al. 2017).

We used the piecewise-constant model called DMX in both TEMPO and PINT to measure the short-timescale DM variations in our data set. All Arecibo data were grouped into DMX windows of 0.5 days, because observations of any given pulsar normally use two receivers back to back. For the GBT, observations with separate receivers are made on different days; we grouped GASP data into 15-day time ranges, and we grouped GUPPI data into 6.5-day time ranges in order to include data from multiple receivers in most DMX windows. We imposed a minimal frequency range criteria for each DMX window; this is described in Section 2.5.2.

If within these DMX time ranges we found that the expected solar wind contribution to the epoch-specific DM induced a timing variation of more than 100 ns, those time ranges were further divided into 0.5-day windows (thus effectively measuring the DMX for a single observing day). We used a toy model as in NG11 to estimate the expected solar-wind-induced time delays: the solar wind electron density is modeled as $n_e = n_0 (r/r_0)^{-2}$ (where r is the distance from the Sun and n_0 is the electron density at $r_0 = 1$ au) and use a representative value of $n_0 = 5$ cm⁻³ (e.g., Splaver et al. 2005). (A similar value of 7.9 cm⁻³ was found by Madison et al. 2019, with NG11 data). Additionally, for PSR J1713+0747, it was necessary to break up the DMX time range surrounding its second chromatic event (Lam et al. 2018a): the DM changes so rapidly that using only a single DMX value over the full length of the event introduces significant noise into the data set. The original DMX time range spanned MJD 57508.36–57512.3;

we divided this time range into two ranges, spanning MJD 57508.36–57510.36 and 57510.36–57512.3.

3.3. Noise Modeling

The noise model used in this analysis is nearly identical to that of NG9 and NG11. The primary difference is that in this work we used the new PTA analysis software ENTERPRISE⁴⁹ (Ellis et al. 2019). In all cases, the final noise model assumes Gaussian noise after all outlier TOAs and otherwise corrupted TOA data have been removed from the data set.

Noise in the timing residuals is modeled as additive Gaussian noise with three white-noise components and, if significantly detected, one red-noise component. For convenience, here we provide a qualitative description of the noise model; for more details, we refer the reader to NG9 and NG11. The four noise components are:

- 1. EFAC, E_k : measured TOA uncertainties σ_i may be underestimated. A separate EFAC parameter, E_k , is therefore used for each combination of pulsar, back end, and receiver, indexed by k, to account for any systematics in TOA measurement uncertainties; hence, σ_i becomes $\sigma_{i,k}$. For the majority of NANOGrav pulsars, $E_k \sim 1$, suggesting that our observing and analysis procedures are resulting in near-true TOA uncertainty estimates.
- 2. EQUAD, Q_k : within ENTERPRISE, the EQUAD term is added in quadrature to the EFAC-scaled TOA uncertainty, i.e., $\sigma'_{i,k} = (E_k^2 \sigma_{i,k}^2 + Q_k^2)^{1/2}$. This term accounts for any uncorrelated systematic white noise that is present in addition to the statistical uncertainties in the TOA calculations. As with EFAC, we use a separate EQUAD parameter, Q_k , for each combination of pulsar, back end, and receiver, indexed by k. TEMPO uses a different whitenoise formulation such that the maximum likelihood EQUAD values contained within the timing models in this data release were obtained via the conversion $Q_{k,\text{Tempo}} = Q_k/E_k$.
- 3. ECORR: this parameter describes a short-timescale noise process that has no correlation between observing epochs but is completely correlated between TOAs that were obtained simultaneously at different observing frequencies (see Appendix C of NG9 for details). Wideband noise processes such as pulse jitter (Osłowski et al. 2011; Shannon et al. 2014; Lam et al. 2016) are accounted for by ECORR.
- Red noise: any steep-spectrum noise components are modeled as a single stationary Gaussian process, whose spectrum we parameterize by a power law,

$$P(f) = A_{\text{red}}^2 \left(\frac{f}{1 \text{ yr}^{-1}}\right)^{\gamma_{\text{red}}},\tag{2}$$

where f is a given Fourier frequency in the power spectrum and A_{red} is the amplitude of the red noise at reference frequency 1 yr^{-1} .

For each pulsar, we incorporated all noise components and timing model parameters into a joint likelihood using ENTER-PRISE and sampled the posterior distribution using the sampler PTMCMC (Ellis & van Haasteren 2017). The red-noise prior

⁴⁹ https://github.com/nanograv/enterprise

Table 2
Basic Pulsar Parameters and TOA Statistics

Source	P	dP/dt	DM	P_b		Median Scaled To	OA Uncertainty ^a (με	s)/Number of Epo	ochs	Span
Source	(ms)	(10^{-20})	$(pc cm^{-3})$	(day)	327 MHz	430 MHz	820 MHz	1.4 GHz	2.1 GHz	(yr)
J0023+0923	3.05	1.14	14.3	0.1		0.063 62	•••	0.556 68	•••	6.0
J0030+0451	4.87	1.02	4.3	•••	•••	0.214 175	•••	0.424 187	1.558 71	12.4
J0340+4130	3.30	0.70	49.6		•••		0.868 68	2.108 71		5.3
J0613-0200	3.06	0.96	38.8	1.2	•••		0.109 134	0.582 135		12.2
J0636+5128	2.87	0.34	11.1	0.1			0.279 39	0.579 42		3.5
J0645+5158	8.85	0.49	18.2				0.297 67	0.836 74		6.1
J0740+6620	2.89	1.22	15.0	4.8			0.445 38	0.651 40		3.5
J0931-1902	4.64	0.36	41.5				1.030 51	1.777 53		4.3
J1012+5307	5.26	1.71	9.0	0.6			0.403 135	0.725 143		12.9
J1024-0719	5.16	1.86	6.5		•••		0.520 90	0.981 94		7.7
J1125+7819	4.20	0.69	12.0	15.4	•••		0.974 40	2.024 42		3.5
J1453+1902	5.79	1.17	14.1		•••	1.141 35	•••	2.120 40	•••	3.9
J1455-3330	7.99	2.43	13.6	76.2	•••		1.100 115	1.937 117	•••	12.9
J1600-3053	3.60	0.95	52.3	14.3	•••	•••	0.271 113	0.227 115	•••	9.6
J1614-2230	3.15	0.96	34.5	8.7	•••	•••	0.374 96	0.593 107	•••	8.8
J1640+2224	3.16	0.28	18.5	175.5		0.048 180		0.375 189		12.3
J1643-1224	4.62	1.85	62.3	147.0			0.288 131	0.499 131		12.7
J1713+0747	4.57	0.85	15.9	67.8			0.188 129	0.077 451	0.061 186	12.4
J1738+0333	5.85	2.41	33.8	0.4				0.520 71	0.901 68	7.6
J1741+1351	3.75	3.02	24.2	16.3		0.142 63		0.352 73		5.9
J1744-1134	4.07	0.89	3.1		•••		0.155 130	0.237 128		12.9
J1747-4036	1.65	1.31	153.0				1.033 61	1.160 65		5.3
J1832-0836	2.72	0.83	28.2				0.596 53	0.524 53		4.3
J1853+1303	4.09	0.87	30.6	115.7		0.353 67		0.593 72	•••	6.0
B1855+09	5.36	1.78	13.3	12.3		0.208 117		0.211 124		12.5
J1903+0327	2.15	1.88	297.5	95.2				0.443 75	0.511 78	7.6
J1909-3744	2.95	1.40	10.4	1.5			0.066 126	0.124 269		12.7
J1910+1256	4.98	0.97	38.1	58.5				0.338 82	0.767 83	8.3
J1911+1347	4.63	1.69	31.0			0.590 42		0.157 46		3.9
J1918-0642	7.65	2.57	26.5	10.9			0.518 126	0.901 128		12.7
J1923+2515	3.79	0.96	18.9			0.259 55	0.510 120	1.023 67		5.8
B1937+21	1.56	10.51	71.1				0.007 127	0.014 220	0.018 86	12.8
J1944+0907	5.19	1.73	24.4			0.278 63		0.825 73		9.3
J1946+3417	3.17	0.32	110.2	27.0		0.270 03		0.414 40	0.547 39	2.6
B1953+29	6.13	2.97	104.5	117.3		0.255 54		0.815 65		5.9
J2010-1323	5.22	0.48	22.2		•••	0.233 34	0.412 94	0.983 96	•••	7.8
J2017+0603	2.90	0.80	23.9	2.2		0.195 6		0.425 67	0.537 50	5.3
J2033+1734	5.95	1.11	25.1	56.3	•••	0.194 40	•••	1.163 46	0.557 50	3.8
J2043+1711	2.38	0.52	20.8	1.5		0.079 137		0.281 151		5.9
J2145-0750	16.05	2.98	9.0	6.8	•••	0.077 137	0.289 111	0.650 116	•••	12.8
J2214+3000	3.12	1.47	22.5	0.4			0.269 111	0.743 72	1.059 57	5.7
J2229+2643	2.98	0.15	22.7	93.0		0.324 45		1.096 47	1.05) 57	3.9
J2234+0611	3.58	1.20	10.8	32.0		0.324 43	•••	0.221 45		3.4
J2234+0011 J2234+0944	3.63	2.01	17.8	0.4	•••	0.429 41	•••	0.314 45	0.746 44	4.0
J2302+4442	5.19	1.39	13.8	125.9			1.200 69	2.413 68	0.740 44	5.3
J2302+4442 J2317+1439	3.45	0.24	21.9	2.5	0.085 79	0.068 188	1.200 09	0.642 141		12.5
J2317+1439 J2322+2057	4.81	0.24	13.4	2.3		0.291 35	•••	1.021 34	1.431 10	2.3
J2322+2037			13.4 g factor ^b (ASP		0.6	0.291 33	0.8	0.8	0.8	2.3
			g factor (ASP actor ^b (GUPPI			0.5		2.5	2.1	
	INUIIII	iai scaiiig ii	acioi (GUPPI,	(I OFFI)	0.7	0.5	1.4	2.3	4.1	

Notes.

bandwidths and integration time. We note that in NG11, we incorrectly calculated the tabulated TOA uncertainties due to a scripting error. This generally led to overestimates of the uncertainty at lower frequencies and underestimates at higher frequencies. The error only applied to values shown in Table 1 of NG11 and did not affect the released data or any other results in the paper. We have corrected this error in the present work.

distribution was log-uniform, while all other prior distributions were uniform. Because the model without red noise is nested within the general model (corresponding to a red-noise

amplitude of zero), we used the Savage–Dickey ratio to estimate the Bayes factor favoring the presence of red noise (Dickey 1971). For pulsars with red-noise Bayes factor *B* above

^a For this table, the original TOA uncertainties were scaled by their bandwidth-time product $\left(\frac{\Delta \nu}{100 \text{ MHz}} \frac{\tau}{1800 \text{ s}}\right)^{1/2}$ to remove variation due to different instrument bandwidths and integration time. We note that in NG11, we incorrectly calculated the tabulated TOA.

^b TOA uncertainties can be rescaled to the nominal full instrumental bandwidth as listed in Table 1 of Arzoumanian et al. (2015) by dividing by the scaling factors given here.

Table 3
Summary of Timing Model Fits

Source	Number		Nu	mber of	Fit Parame	eters ^a		rms ^b	(μs)		Red Noise	c	Figure
Source	of TOAs	S	A	В	DM	FD	J	Full	White	$A_{\rm red}$	$\gamma_{\rm red}$	$log_{10} B$	Numbers
J0023+0923	12516	3	5	9	67	4	1	0.285				1.21	6
J0030+0451	12543	3	5	0	190	4	2	25.157	0.200	0.003	-6.3	>2	7
J0340+4130	8069	3	5	0	74	4	1	0.446				-0.21	8
J0613-0200	13201	3	5	8	139	2	1	0.486	0.178	0.123	-2.1	>2	9
J0636+5128	21374	3	5	6	44	1	1	0.640				-0.09	10
J0645+5158	7893	3	5	0	79	2	1	0.207				-0.20	11
J0740+6620	3328	3	5	7	44	1	1	0.132				-0.17	12
J0931-1902	3712	3	5	0	57	0	1	0.452				-0.15	13
J1012+5307	19307	3	5	6	142	4	1	0.999	0.272	0.406	-1.6	>2	14
J1024-0719	9792	4	5	0	100	2	1	0.334				-0.08	15
J1125+7819	4821	3	5	5	43	3	1	0.862				0.09	16
J1453+1902	1555	3	5	0	39	0	1	0.606				-0.13	17
J1455-3330	8408	3	5	6	122	2	1	0.656				-0.14	18
J1600-3053	14374	3	5	8	128	2	1	0.245				0.55	19
J1614-2230	12775	3	5	8	114	2	1	0.177				-0.24	20
J1640+2224	9256	3	5	8	188	4	1	0.177				-0.20	21
J1643-1224	12798	3	5	6	141	2	1	2.645	0.534	1.498	-1.4	>2	22
J1713+0747	37698	3	5	8	325	5	3	0.101	0.069	0.030	-1.3	>2	23
J1738+0333	6977	3	5	5	78	1	1	0.276				-0.24	24
J1741+1351	3845	3	5	8	73	2	1	0.156				-0.24 -0.08	25
J1744-1134	13380	3	5	0	136	4	1	0.130	0.307	0.155	-2.2	>2	26
J1747-4036	7572	3	5	0	71	1	1	6.343	1.414	0.709	-2.2 -3.3	>2	27
J1832-0836	5364	3	5	0	58	0	1	0.343		0.709	-3.3	-0.05	28
J1853+1303	3544	3	5	8	72	0	1	0.187	0.110	0.140	-2.2	-0.03 >2	29
B1855+09	6464	3	5	7	125	3	1	1.757	0.110	0.140	-2.2 -3.4	>2	30
J1903+0327	4854	3	5	8	82	1	1	2.668	0.337	1.482	-3.4 -1.6	>2	31
J1909-3744	22633	3	5	9	223	1	1	0.334	0.313	0.028	-1.0 -2.7	>2 >2	32
	5012	3	5	6	88	1	1	0.334	0.001	0.028	-2.7	-0.06	33
J1910+1256	2625	3	5	0		2	1	0.187					
J1911+1347		3		7	46	5	1		•••	•••		0.20 0.02	34
J1918-0642	13675		5		133			0.299	•••	•••			35
J1923+2515	3009	3	5	0	67	1	1	0.269				-0.15	36
B1937+21	17024	3	5	0	204	5	3	2.277	0.103	0.099	-3.3	>2	37
J1944+0907	3931	3	5	0	73	2	1	0.365	•••	•••	•••	0.12	38
J1946+3417	3016	3	5	8	41	1	1	0.468	•••	•••	•••	1.77	39
B1953+29	3421	3	5	6	65	2	1	0.475		•••	•••	1.05	40
J2010-1323	13306	3	5	0	108	1	1	0.244		•••	•••	-0.22	41
J2017+0603	2986	3	5	7	73	0	2	0.076	•••	•••	•••	-0.22	42
J2033+1734	2691	3	5	5	46	2	1	0.561	•••	•••	•••	-0.12	43
J2043+1711	5624	3	5	7	151	4	1	0.151	•••	•••	•••	1.41	44
J2145-0750	13961	3	5	7	123	2	1	1.467	0.328	0.347	-2.1	>2	45
J2214+3000	6269	3	5	5	77	1	1	0.402	•••	•••	•••	-0.17	46
J2229+2643	2442	3	5	6	47	2	1	0.194	•••	•••	•••	-0.18	47
J2234+0611	2475	3	5	7	45	2	1	0.061		•••	•••	0.60	48
J2234+0944	5892	3	5	5	51	2	1	0.160	•••	•••	•••	-0.13	49
J2302+4442	7833	3	5	7	75	1	1	0.716	•••	•••	•••	-0.15	50
J2317+1439	9835	3	5	6	210	3	2	8.798	0.253	0.007	-6.4	>2	51
J2322+2057	2093	3	5	0	35	4	2	0.235	•••	•••	•••	-0.13	52

Notes.

a threshold of B>100, we included the red-noise parameters in the final timing models; for the rest of the pulsars, we reran their analyses without red noise. This exercise typically did not affect the detectability of other parameters, but in a small number of cases, the presence or absence of red noise did affect marginal timing parameters like \dot{x} , ϵ_1 , or ϵ_2 (see the discussion of the PSR J1909–3744 binary model in Section 7).

The Savage–Dickey ratio fails to estimate a finite Bayes factor for heavily preferred red-noise models with a finite-length chain of samples. Indeed, for all of the pulsars with above-threshold red noise, B was large enough that it was not robustly estimated. As such, we simply report the $\log_{10} B$ for those pulsars in Table 2 as >2. Further details on the red-noise characterization are provided in NG9 and NG11, and

^a Fit parameters: S = spin; A = astrometry; B = binary; DM = dispersion measure; FD = frequency dependence; J = jump.

b Weighted rms of epoch-averaged postfit timing residuals, calculated using the procedure described in Appendix D of NG9. For sources with red noise, the "Full" rms value includes the red-noise contribution, while the "White" rms does not.

^c Red-noise parameters: A_{red} = amplitude of red-noise spectrum at $f = 1 \text{ yr}^{-1}$ measured in μ s $\text{yr}^{1/2}$; γ_{red} = spectral index; B = Bayes factor (">2" indicates a Bayes factor larger than our threshold $\log_{10} B > 2$, but which could not be estimated using the Savage–Dickey ratio). See Equation (2) and Appendix C of NG9 for details.

Table 4
Noise Parameter Comparison for 11 yr Data Subset

Noise Parameter	# Decreased ^a	# Increased ^a	Mean Difference ^b
EFAC	109	30	-0.044
EQUAD	60	79	$-0.013~\mu s$
ECORR	79	60	$-0.017~\mu { m s}$

Notes.

Appendix C of NG9 provides a complete description of the Bayesian inference model.

Fourteen pulsars were found to have red noise with B > 100; this includes all 11 sources with detected red noise in NG11. Of the three MSPs with newly detected red noise (J1744–1134, J1853+1303, and J2317+1439), two of them are among the longest-observed pulsars in the data set.

The Bayes factors for the pulsars in which red noise was not detected are listed in Table 3. Several pulsars have subthreshold Bayes factors sufficiently larger than 1, such that we may expect those pulsars to display red noise above our defined threshold with several more years of data. A more detailed noise analysis of each pulsar is beyond the scope of this work, but will be performed as part of the gravitational wave analyses for the data set in a forthcoming work.

3.4. Improved Noise Parameters over the 11 yr Data Set

Our data reduction methods (Section 2.3) and data cleaning methods (Section 2.5) are designed to minimize nonastrophysical noise sources in the data set. Minimizing these noise sources is important because both white noise and red noise have important consequences for the detection of nanohertz gravitational waves (Siemens et al. 2013; Lam et al. 2016, 2018b; Hazboun et al. 2020).

Here we test the methods used in the present work with our previous-generation NG11 data set to see whether the refined methods result in a reduction of noise. To make this comparison with NG11, we use a subset of the present data set that corresponds to the pulsars and date range of NG11, i.e., a data set equivalent to "generating a NG11 data set with procedures of the present work." A full noise analysis was done on this data subset, consistent with the analyses done in NG11. This sliced analysis has the advantage of using the same time span of data, which avoids biases from searching for different frequencies of a steep spectral-index red process. Using the same time span also keeps the number of TOAs in a receiver +back-end combination similar so there is no bias in determining white-noise parameters with largely differing numbers of TOAs. While a refit to the timing model is out of the scope of such a comparison, the data sets are otherwise similar except for the various data pipeline improvements referenced above. For the pulsars considered for this analysis, there were 139 pulsar-receiver-back-end combinations analyzed, and the changes in their white-noise parameters are shown in Table 4. The most dramatic change is seen in the EFAC parameters, where 109 parameters had EFAC values smaller than in NG11, with a mean difference of -0.044. Both

the mean EQUAD and ECORR also decrease, but by smaller amounts. The changes in red noise are more subtle, with some pulsars showing mildly increased support for steep spectral-index noise processes. These will be discussed in detail in the forthcoming paper presenting our results from GW analyses.

4. Comparison of TEMPO and PINT Timing Models

The NANOGrav 12.5 yr data analysis results are crosschecked by the new timing package PINT (version 0.5.7), which has a completely independent code base from TEMPO and TEMPO2. In this section, we present a comparison between the PINT and TEMPO timing results for the narrowband TOA data set. This comparison focuses on the discrepancies of the postfit parameter values. We used timing models produced by TEMPO as the initial input models for PINT, and refit the TOAs with PINT's general least-squares fitter. Then, the best-fit parameters from these two packages were compared against each other. The noise parameters obtained by the ENTERPRISE analysis (Section 3.3) were not altered by PINT, thus we do not compare the noise parameters. ⁵⁰ To describe the changes of parameter values with an intuitive, standardized quantity, we divide the parameter value differences by the TEMPO uncertainties. We have compared 5417 parameters in total; 3929 best-fit parameter values from PINT deviate from the TEMPO values by less than 5% of their TEMPO uncertainties. Among the rest, 1442 parameters' PINT results changed by less than 50% of their TEMPO uncertainties (for example, changes of the order 10^{-14} – 10^{-10} Hz for spin frequencies, or 10^{-11} – 10^{-3} days for orbital periods), and 46 parameters' discrepancies are more significant than 50%.

A majority of the outstanding discrepancies (>50% of TEMPO uncertainty) can be explained by different implementations in the two software packages. Thirty-two of these outlier parameters belong to the two pulsars that have the largest amplitude of red noise, J1643-1224 and J1903+0327. TEMPO effectively uses a lower cutoff frequency in the spectrum describing red noise, which will make the uncertainties on the spin frequency and its derivative larger. This implementation difference also causes the discrepancies seen in the spin frequency and spin frequency derivative parameters and uncertainties for other pulsars with red noise. For instance, PSR J2317+1439's spin frequency has the largest difference, 61% of its TEMPO uncertainty (corresponding to a change of $\approx 2 \times 10^{-11}$ Hz); it also has the steepest red-noise index in the data set, $\gamma_{\rm red} = -6.5$. Another implementation difference is that PINT uses a different definition for the longitude of ascending node ("KOM" parameter) in the DDK binary model. Thus, 10 parameters from PSR J1713+0747, which uses the DDK binary model, showed discrepancies greater than 50% of their original TEMPO uncertainty. Other known implementation differences, which can induce small systematic offsets or differences on the order of $\sim 10 \, \text{ns}$, are summarized in Luo et al. (2020). However, the reasons for the remaining three parameters with larger differences— h_4 of PSR J1853+1303,

^a The number of noise parameters whose values decreased or increased in the 11 yr "slice" of the 12.5 yr data set, compared with their values from the 11 yr data set (Section 3.4).

^b Weighted mean difference in noise parameters. These are computed as the difference between the 11 yr data set values and the 11 yr "slice" values, weighted by the errors on the 11 yr data set values.

⁵⁰ We ran ENTERPRISE using both TEMPO and PINT on a small subset of pulsars from this data release in order to obtain posterior distributions of the noise parameters independently using both timing packages. Using a Kolmogorov–Smirnov test to compare the resulting distributions for a given pulsar, we found that all noise parameter posterior distributions were statistically consistent between the PINT- and TEMPO-mode runs of ENTERPRISE.

Table 5New NANOGrav 12.5 yr Parallax Measurements

PSR	Parallax (mas)	Previous Measurement (mas)	Technique	Reference
J0636+5128	1.37 ± 0.23	4.9 ± 0.6	Timing	Stovall et al. (2014)
J1012+5307	1.13 ± 0.35	$1.21^{+0.03}_{-0.08}$	VLBI	Ding et al. (2020)
J1832-0836	0.48 ± 0.13	•••		
J1853+1303	0.48 ± 0.14	1.0 ± 0.6	Timing	Gonzalez et al. (2011)
B1937+21	0.28 ± 0.05	$0.40\pm0.16^{\mathrm{a}}$	Timing	Reardon et al. (2016)
J2010-1323	0.41 ± 0.12	$0.48^{+0.17}_{-0.12}$	VLBI (VLBA)	Deller et al. (2019)
J2322+2057	0.98 ± 0.26	<4.8	Timing	Nice & Taylor (1995)

Note.

 $T_{\rm asc}$ of PSR J1918–0642, and the ecliptic longitude λ of PSR J1640+2224—are still under investigation.

5. Newly Measured Timing Parameters in the NANOGrav Data Set

Comparing the present data set with NG11, we find a number of astrometric and binary timing parameters that were not previously measured at a significant level (as defined by the *F* test in Section 3) with NANOGrav data. Here we highlight those parameters and compare with any previously published values from other teams.

5.1. Newly Significant Astrometric Parameters

The NANOGrav 12.5 yr data release includes seven new measurements of annual trigonometric parallax compared to NG11 (Table 5), although in contrast to NG11, the parallax measurements for PSRs J0740+6620 and J2234+0944 are no longer significant (but see Cromartie et al. 2020 for the former). In addition, both components of the proper motion are newly measured for PSR J1747-4036, along with one component for PSRs J0023+0923, B1937+21, and J2017+0603. (For the latter three MSPs, the other proper motion component was already measured in previous data sets.)

In Table 5, we compare the new NANOGrav parallax values with prior parallax measurements for the same objects. The previous parallaxes for PSRs J1012+5307, J1853+1303, and J2010-1323 are consistent with our measurements, while spanning the gamut of measurement techniques (timing, VLBI, and optical companion parallax from Gaia). For PSR J0636+5128, the NANOGrav data span \sim 3.5 yr as opposed to only \sim 1.5 yr available to Stovall et al. (2014). The parallax for PSR B1937+21 published in the first PPTA data release (DR1; Reardon et al. 2016) is consistent with that presented here.

5.2. Newly Significant Binary Parameters

Several orbital parameters not detected in prior NANOGrav data releases have been measured in the 12.5 yr data set. Of particular interest in our data set are new measurements of the secular evolution of projected orbital semimajor axis (\dot{x}) and of the orthometric parameters $(h_3$, and h_4 or $\varsigma = h_4/h_3)$ that parameterize the Shapiro delay (Freire & Wex 2010). We measure \dot{x} for four additional pulsars relative to NG11: PSRs J0613-0200, B1953+29, J2145-0750, and J2229+2643. We now measure both h_3 and h_4 in the timing model of PSR J1853+1303, for which only h_3 was measured with significance in NG11. We measure the first indication of

Shapiro delay in PSR J2145-0750 with a measurement of h_3 . Additionally, for the newly added pulsar PSR J1946+3417, we measure $\dot{\omega}$ and Shapiro-delay parameters that are consistent with those reported by Barr et al. (2017).

Checking the literature and the Australia Telescope National Facility (ATNF) pulsar catalog⁵¹ (Manchester et al. 2005, version 1.63), we find no previously measured values of \dot{x} for PSRs J0613-0200 or J2229+2643. For PSR J2145-0750, our measurement of $\dot{x}=(5.8\pm1.0)\times10^{-15}$ lt-s s⁻¹ is consistent at the \sim 2 σ level with that of Reardon et al. (2016). Our measurement of h_3 for PSR J2145-0750 is the first indication of Shapiro delay for this pulsar and aids in constraining the companion mass (Section 7). The timing model for PSR J1853 +1303 in the ATNF pulsar catalog contains h_3 and h_4 , with values consistent with those found in this work and previously in NG11 (for h_3).

In addition to secular and Shapiro-delay parameters, we also measure one new Laplace–Lagrange eccentricity component (ϵ_1 or ϵ_2) in PSRs J0023+0923, J1738+0333, and J2214+3000 with $\gtrsim 3\sigma$ significance. We also find that although \dot{P}_b for PSR J0636+5128 and $\dot{\omega}$ for J1600-3053 were detected at a significant level in NG11, they are not measured significantly in the present data set, and so are no longer included in the timing models for these pulsars.

6. Consistency of Astrometric Parameters across Data Sets

As noted previously, our pulsar timing analyses always include five astrometric parameters as free parameters: two sky position parameters, two components of proper motion, and annual trigonometric parallax. Detailed analyses of the astrometry of NANOGrav pulsars, including comparisons with VLBI measurements, were presented in Matthews et al. (2016) and NG11, thus we do not repeat such a detailed analysis in the present work. Comparisons of astrometric measurements obtained via different measurement methods (e.g., Table 5) are potentially useful for such purposes as tying astrometric reference frames (Wang et al. 2017), using measurements made by one method as priors in analysis of other data, etc. To make use of pulsar astrometric measurements, it is important that they be robust, accurate, and stable over time. To test the stability of our astrometric measurements, we compare the parallax and proper motion measurements between the current and previous NANOGrav data releases (with newly detected astrometric parameters specifically highlighted in the previous section).

^a For PSR B1937+21, we quote the timing parallax measurement from Reardon et al. (2016) that was corrected for the Lutz-Kelker bias (Verbiest et al. 2012).

⁵¹ https://www.atnf.csiro.au/research/pulsar/psrcat/

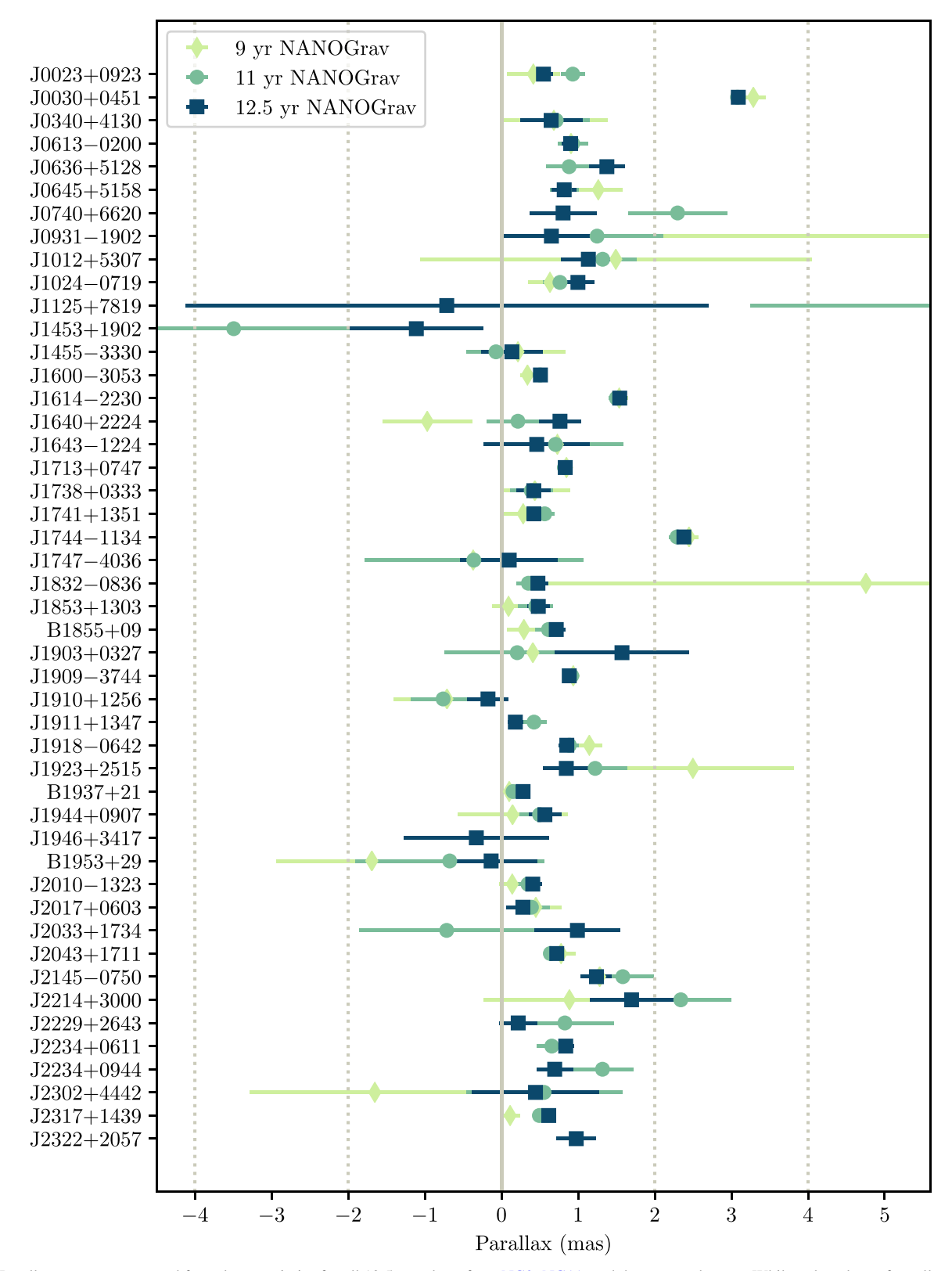


Figure 3. Parallax measurements and formal uncertainties for all 12.5 yr pulsars from NG9, NG11, and the current data set. While only values of parallax greater than zero are physically meaningful, all formally fit values are shown here; the preponderance of positive values serves to verify that a real physical parameter is being measured. Two outlier values from previous data releases fall beyond the right edge of the plot, as indicated by the error bars.

For pulsar timing, the position (and hence proper motion) is naturally parameterized in terms of ecliptic coordinates. As the timing data span increases, the proper motion is expected to be measured with increasing accuracy, and the covariance between proper motion and parallax should rapidly decrease. Figure 3 shows the measured parallaxes in the 12.5 yr data release, as well as previous (NG9 and NG11) measurements, where available. The number of measurements has increased

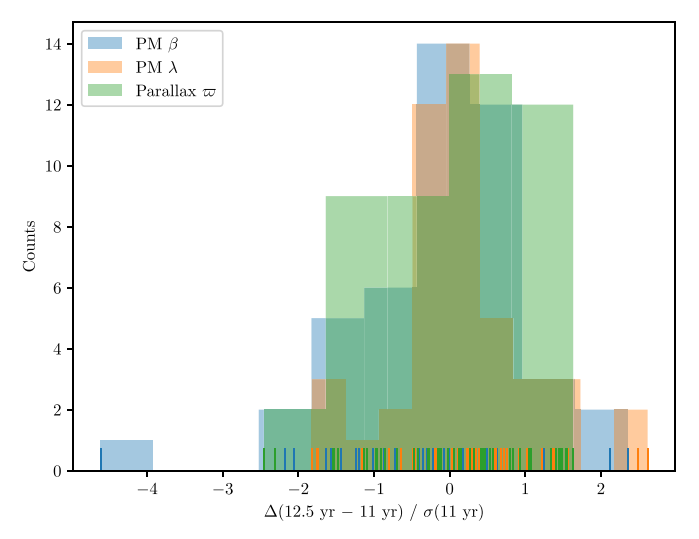


Figure 4. Comparison of astrometric measurements across NG11 and the current 12.5 yr data set. The differences in proper motion $(\mu_{\beta}, \mu_{\lambda})$ and parallax ϖ are shown in units of the uncertainty in the 11 yr measurement (σ_{11}) . The figure shows binned histograms of each type of measurement, with all individual measurements superimposed as short vertical lines at the bottom of the figure. The value of μ_{β} for PSR J2214+3000 is an outlier at -4.6σ ; the rest are reasonably consistent, as discussed in the text.

(see Section 5.1 below), and the formal significance has generally improved.

However, a comparison of the changes in astrometric parameters between the current and previous (11 yr) data releases might suggest that some caution is warranted. In Figure 4, we show histograms of the differences in proper motion (μ_{β} and μ_{λ}) and parallax (ϖ) between the current (12.5 yr) and NG11 data releases, with the differences scaled by the estimated uncertainty for the 11 yr parameters (i.e., $(P_{12.5}-P_{11})/\sigma_{11}$, where $P=\{\mu_{\beta},\mu_{\lambda},\varpi\}$).

The single obvious outlier is the measurement of μ_{β} for PSR J2214+3000, at $-4.6\sigma_{11}$. For pulsars near the ecliptic plane, the ecliptic latitude β is poorly constrained by timing in comparison to the ecliptic longitude λ , and we expect the accuracy of μ_{β} measurements to be correspondingly worse. That alone cannot explain the discrepancy for J2214+3000, at $\beta = 37^{\circ}.7$. The other notable fact about this source is that it is one of four black widow pulsars in our data set, along with J0023+0923, J0636+5128, and J2234+0944. Like the other black widows in our sample, it does not exhibit eclipses (Ransom et al. 2011), and, as with J2234+0944, it does not show orbital variability (Arzoumanian et al. 2018b; Bak Nielsen et al. 2020). In NG11, we noted difficulty fitting a noise model to this pulsar, possibly related to excess noise in mid to late 2013. Imperfect noise modeling, combined with covariance between noise parameters and astrometric parameters, may contribute to the change in reported μ_{β} value.

Besides J2214+3000, the astrometric parameters appear generally consistent between the 11 yr and 12.5 yr measurements, with $\sim\!85\%$ of the measurements differing by less than $\pm 1.5\sigma_{11}$. Even though NG11 is a subset of the 12.5 yr data release, such measurement differences are not unreasonable. Due to the additional processing of the 12.5 yr data, as described in Section 2.5, in combination with a longer baseline that further downweights the earlier, less constraining data, such changes in the astrometric parameters can be expected.

7. Binary Analysis of Selected Pulsars

In NG11, we presented a summary of modeling methods and results for binary pulsars in the data set presented therein; we do not repeat such detailed descriptions here. Instead, we highlight five binary pulsars for which additional description or analysis is warranted. PSR J0740+6620 is an extremely highmass MSP for which a more up-to-date timing solution is published in Cromartie et al. (2020); for PSRs J1909–3744 and J2234+0611, significant testing was required to obtain the timing models presented in this work, and we use the newly measured Shapiro-delay parameters of PSRs J1853+1303 and J2145–0750 to place mass and geometry constraints on these systems.

7.1. PSR J0740+6620

In the course of analyzing the 12.5 yr data set, we found that the significance of the Shapiro delay in PSR J0740+6620 had dramatically increased from its initial detection in NG11. The constraints on m_c , $\sin i$, and the pulsar mass (m_p) from the nominal 12.5 yr data set motivated additional, targeted observations for improving the Shapiro-delay measurement. By combining 12.5 yr NANOGrav timing data with additional data obtained during specific orbital phases optimally sensitive to Shapiro delay, Cromartie et al. (2020) found an improved pulsar mass of $m_p = 2.14^{+0.10}_{-0.09} M_{\odot}$ (68.3% credible region), representing the most massive, precisely measured neutron star known to date.

7.2. PSR J1853+1303

Both h_3 and h_4 of the orthometric parameterization of the Shapiro delay (Freire & Wex 2010) for PSR J1853+1303 are significant. Our new measurements ($h_3 = 0.18 \pm 0.04 \, \mu s$, $h_4 = 0.17 \pm 0.05 \, \mu s$) are consistent with those first presented in NG11. We tested whether $\sin i$ and m_c could be independently measured using TEMPO, as described in Section 3.1, but this test was not successful.

The orthometric parameters h_3 , h_4 , and ς are related to the traditional post-Keplerian Shapiro-delay parameters as

$$\varsigma = \sqrt{\frac{1 - \cos i}{1 + \cos i}},\tag{3}$$

$$h_3 = r\varsigma^3, \tag{4}$$

$$h_4 = h_3 \varsigma, \tag{5}$$

where $r=m_{\rm c}T_{\odot}$ is the "range" of the delay, $m_{\rm c}$ is the companion mass, and $T_{\odot}\simeq 4.93~\mu{\rm s}$. This parameterization constrains the orbital inclination to $i=85^{\circ}\pm14^{\circ}$ (we quote the 1σ uncertainty, derived from error propagation beginning with the 1σ parameter uncertainties from the TEMPO timing model). The orthometric parameters are not yet sufficiently well measured to place meaningful bounds on r and, therefore, the companion mass, which we calculate to be consistent with zero (at the 1σ confidence level). More insight into the physical properties of this system may be gained by explicit gridding of the posterior distribution in future work.

7.3. PSR J1909-3744

The value of \dot{x} for PSR J1909–3744 has been measured or constrained by several groups. Verbiest et al. (2009) found

 $\dot{x}=(5\pm4)\times 10^{-16}~{\rm lt\text{-s}\,s^{-1}},$ while Desvignes et al. (2016) found $\dot{x}=(0.6\pm1.7)\times 10^{-16}~{\rm lt\text{-s}\,s^{-1}}.$ In NG11, we found $\dot{x}=(-4\pm1)\times 10^{-16}~{\rm lt\text{-s}\,s^{-1}}.$ Using the 12.5 yr data set for PSR J1909–3744, we have further constrained its value to $(-2.9\pm0.8)\times 10^{-16}~{\rm lt\text{-s}\,s^{-1}}.$

As in NG9 and NG11, we detect red noise in PSR J1909 -3744. In this work, we find \dot{x} and the red-noise terms in the timing model to be covariant. In particular, the presence or absence of \dot{x} in the timing model had a significant effect on the red-noise amplitude: the amplitude was significantly lower when \dot{x} was included in the model compared to when \dot{x} was not included. Additionally, if \dot{x} was initially excluded from the timing model such that the red-noise amplitude assumed its higher value, then adding \dot{x} to the model while red noise was also included resulted in a nonmeasurement of \dot{x} according to our F-test criterion. While not common, this covariant behavior is not unexpected, as \dot{x} is a secular parameter that evolves slowly, as does red noise.

The value of \dot{x} can be inferred from the changing geometry due to the relative motion between the pulsar system and Earth (Kopeikin 1995),

$$\dot{x}_{k} = x\mu \cot i \sin(\Theta_{\mu} - \Omega), \tag{6}$$

where $\sin i$ is constrained from the Shapiro delay, giving $i=86^{\circ}.39$ or $93^{\circ}.61$; the magnitude of proper motion $\mu=36.94\,\mathrm{mas\,yr^{-1}}$; the position angle of the proper motion (Θ_{μ}) is derived from timing measurements of proper motion; and Ω is the longitude of the ascending node. In the case where annual orbital parallax is detected, the three-dimensional geometry of the system can be constrained, such that the values of i and Ω are measured definitively (as opposed to having two possible values of i and four possible values of Ω).

We attempted to directly fit for i and Ω using the DDK model in TEMPO, but the fit did not converge. Therefore, we instead performed the following test to determine whether we were likely measuring a physically reasonable value of \dot{x} in the absence of a significant detection of annual orbital parallax. Using the T2 model in TEMPO2,⁵² we fixed i at each of its two possible values, ⁵³ and then ran TEMPO2 over a grid of Ω values. From this gridding test, we found the best-fit $(i, \Omega) = \{(86^{\circ}.39, 350^{\circ}), (93^{\circ}.61, 170^{\circ})\}$ and used them to calculate \dot{x}_k . In all cases, $\dot{x}_k \approx -3 \times 10^{-16}$ lt-s s⁻¹, consistent with the value we measure from timing.

This result suggests that the \dot{x} we measure with TEMPO for PSR J1909–3744 is robust and should be included in the model rather than being absorbed by red noise. As noted above, it is also consistent with and an improvement upon our \dot{x} measurement from NG11. We have therefore included this \dot{x} value in our timing model for this pulsar.

7.4. PSR J2145-0750

We can place loose constraints on the geometry of the PSR J2145-0750 system using the proper motion and h_3 measurements. An upper bound on the orbital plane inclination

can be calculated by inverting Equation (6) and attributing the measured \dot{x} to the proper motion (e.g., Fonseca et al. 2016):

$$i_{\text{max}} = \arctan \frac{x\mu}{|\dot{x}_{\text{obs}}|},\tag{7}$$

yielding $i_{\rm max}=74^{\circ}\pm5^{\circ}$. We can then combine Equations (3) and (4) to obtain $r_{\rm min}$, yielding a lower bound on the companion mass, $m_{\rm c,min}=r_{\rm min}/T_{\odot}=0.08\pm0.03\,M_{\odot}$. Much more robust system constraints have previously been made with a combination of optical imaging, VLBI parallax, and radio timing: $i=21^{+7}_{-4}$ deg and $m_{\rm c}=0.83\pm0.06\,M_{\odot}$ (Deller et al. 2016), and $i=34^{+5}_{-7}$ deg and $m_{\rm p}=1.3^{+0.4}_{-0.5}\,M_{\odot}$ (Fonseca et al. 2016). We will place improved constraints on the geometry and mass of the PSR J2145–0750 system in future studies with longer timing baselines.

7.5. PSR J2234+0611

The eccentric orbit and high timing precision of J2234 +0611 allowed Stovall et al. (2019) to measure a large number of binary-related effects from this system, including one orthometric Shapiro-delay parameter (h_3) and annual orbital parallax. Together, these measurements allowed Stovall et al. to unambiguously determine the three-dimensional geometry of the system, giving $i \approx 138^\circ.7$ and $\Omega \approx 44^\circ.$ These parameters correspond to $\dot{x}_k = (-2.78 \pm 0.07) \times 10^{-14}$ lt-s s⁻¹.

In this work, we find that i and Ω are not constrained, and we do not obtain a significant measurement of h_3 . There are two likely reasons that we are not able to reproduce the measurements of Stovall et al. First, their data set is a superset of that presented here, with an additional ~ 1.5 yr in their timing baseline. Second, Stovall et al. fix i and $\varsigma = h_4/h_3$ based on the derived value of $s = \sin i$ from the DDGR binary model; they then constrain Ω by running TEMPO over a grid in i, Ω , and $m_{\text{tot}} = m_{\text{p}} + m_{\text{c}}$, where i and Ω are held constant at each step. Based on our F-test criterion for including post-Keplerian parameters, we instead fit for \dot{x} (which is related to annual orbital parallax and its secular variation shown in Equation (6)); its value, $(-2.8 \pm 0.2) \times 10^{-14}$ lt-s s⁻¹, is consistent with that found by Stovall et al.

8. Flux Densities

The algorithm used to calculate TOAs in our narrowband data (Section 2.4) also yields the amplitudes of the pulsed signals relative to the amplitudes of the template profiles used for timing. Through suitable calibration and normalization of the template profiles, these amplitudes can be used to estimate the period-averaged flux densities of the pulsed signals. In this section, we describe our flux density calculations. The results are summarized in Table 6.

For the flux density analysis, we used only GUPPI and PUPPI data. The narrower bands of GASP and ASP made them less suitable for the cross-checks described below and would have yielded less robust measurements.

8.1. Absolute Calibration

As described in Section 2, each individual observation was preceded by a pulsed-cal measurement using an artificial noise signal. The pulsed-cal measurements were used to calibrate the amplitude scale of the pulsar observations. The noise signals themselves were calibrated by measuring them in on- and off-source observations of a standard continuum calibrator radio

⁵² We used TEMPO2 instead of TEMPO because the T2 model, which can be used to model the effects described by Kopeikin (1995, 1996) for low-eccentricity systems, does not exist in TEMPO. PSR J1909–3744 has a very low eccentricity, so using an ELL1-type model is preferable to, e.g., DD.

⁵³ We chose to fix *i* at its two possible values rather than also running a grid over *i* values because $\sin i$ is well constrained for this pulsar, at $\sin i = 0.99794 \pm 0.00007$. Thus, we could expect the best-fit \dot{x}_k to also have small errors, allowing us to determine whether it is consistent with the secular \dot{x} found by TEMPO.

Table 6 Flux Densities

PSR		S_{430}			S_{800}				S_{1400}			S_{2000}			
	Obs.	16 ^a	(mJy) 50 ^a	84 ^a	16 ^a	(mJy) 50 ^a	84ª	16 ^a	(mJy) 50 ^a	84 ^a	16 ^a	(mJy) 50 ^a	84 ^a	Spectra Index ^b	
0023+0923	AO	1.93	2.50	3.95				0.21	0.32	0.54			•••	-1.74	
0030+0451	AO	2.34	5.80	23.12				0.85	1.12	1.60	0.48	0.60	0.78	-1.39	
0340+4130	GB				1.14	1.42	1.89	0.45	0.54	0.60				-1.73	
0613-0200	GB			•••	5.45	6.66	8.12	1.81	2.17	2.48				-2.00	
0636+5128	GB				1.64	2.08	2.90	0.73	0.94	1.18				-1.42	
0645+5158	GB				0.47	0.76	2.02	0.17	0.29	0.86				-1.72	
0740+6620	GB				1.11	2.19	6.06	0.43	0.27	1.71				-1.46	
931-1902	GB				1.41	1.90	2.60	0.60	0.84	1.24				-1.46	
012+5307	GB				3.19	6.93	16.46	1.46	2.90	6.09				-1.56	
024-0719	GB		•••	•••	1.43	2.92	7.48	0.74	1.36	2.56	•••		•••	-1.37	
125+7819	GB			•••	1.39	2.58	5.20	0.55	0.90	1.70			•••	-1.88	
453+1902	AO	1.11	1.64	2.81	1.39	2.36	5.20	0.33	0.30	0.48				-1.86	
455-3330	GB	1.11	1.04	2.01	1.42	2.28	5.03	0.11	0.17	1.51		•••		-1.92 -2.04	
													•••		
600-3053	GB				2.66	3.17	4.02	1.99	2.37	2.99				-0.52	
614-2230	GB	4.20			2.02	2.68	3.51	0.79	1.11	1.53	•••	•••	•••	-1.58	
640+2224	AO	4.20	6.31	11.33				0.24	0.54	1.26	•••	•••	•••	-2.08	
643-1224	GB	•••	•••	•••	11.31	13.02	14.50	4.06	4.70	5.38				-1.8	
713+0747	AO	•••	•••	•••				2.47	4.69	8.70	2.24	5.01	10.24	0.19	
713+0747	GB	•••	•••	•••	3.39	6.14	12.12	2.02	4.32	8.43	•••	•••	•••	-0.63	
738 + 0333	AO	•••	•••	•••	•••	•••	•••	0.37	0.48	0.82	0.26	0.43	0.65	-0.3	
741+1351	AO	1.79	2.60	4.64	•••	•••	•••	0.14	0.21	0.38	•••	•••	•••	-2.11	
744-1134	GB	•••	•••	•••	2.94	5.29	10.48	0.98	1.96	4.74		•••	•••	-1.7°	
747-4036	GB	•••	•••	•••	5.63	6.85	9.05	1.31	1.55	2.20	•••	•••	•••	-2.66	
832-0836	GB	•••	•••	•••	3.14	3.65	4.23	0.90	1.11	1.35		•••	•••	-2.13	
853 + 1303	AO	3.13	4.71	7.11	•••	•••	•••	0.24	0.43	0.59	•••	•••	•••	-2.03	
1855+09	AO	14.36	19.17	26.18	•••	• • •	•••	2.13	3.47	6.50	•••	•••	•••	-1.43	
903+0327	AO	•••	•••	•••	•••	•••	•••	0.63	0.69	0.79	0.45	0.52	0.58	-0.79	
909-3744	GB				1.54	3.01	5.15	0.55	1.03	2.17		•••		-1.92	
910+1256	AO							0.35	0.56	0.69	0.21	0.31	0.47	-1.66	
911+1347	AO	2.10	2.93	4.16		•••		0.51	0.86	1.26		•••		-1.04	
918-0642	GB				3.12	4.13	5.43	0.89	1.36	1.99		•••		-1.98	
923+2515	AO	2.04	2.56	3.36				0.18	0.28	0.49			•••	-1.8'	
1937+21	AO			•••				9.14	12.44	16.56	3.24	4.72	6.25	-2.72	
1937+21	GB				41.93	56.37	74.68	11.33	14.83	18.65				-2.39	
944+0907	AO	14.57	18.82	28.53				1.08	1.94	3.41				-1.92	
946+3417	AO							0.84	0.92	0.96	0.56	0.61	0.66	-1.13	
1953+29	AO	10.77	12.00	13.28				0.69	0.94	1.21				-2.10	
010-1323	GB				1.20	1.63	2.12	0.50	0.71	0.92				-1.49	
017+0603	AO							0.22	0.32	0.46	0.21	0.31	0.42	-0.09	
033+1734	AO	2.98	3.62	4.23				0.26	0.30	0.38				-2.11	
043+1711	AO	1.51	1.99	3.01				0.15	0.21	0.40				-1.9	
145-0750	GB			5.01	5.10	14.25	38.84	1.69	4.86	12.15			•••	-1.92	
214+3000	AO				5.10			0.28	0.38	0.70	0.20	0.35	0.51	-0.23	
229+2643	AO	2.19	3.61	7.96				0.28	0.38	0.70			0.51	-0.23	
234+0611	AO AO	0.72	0.90	1.82	•••		•••	0.22	0.41	0.70			•••	-0.83	
234+0011	AO AO	0.72	0.90	1.82			•••	0.12	1.15	2.83	0.40	0.76	1.14	-0.8. -1.10	

Table 6 (Continued)

PSR	Obs.		S_{430}		S_{430} S_{800}			S_{1400}			S_{2000}			
			(mJy)			(mJy)			(mJy)			(mJy)		Index
		16 ^a	50 ^a	84ª	16 ^a	50 ^a	84 ^a	16 ^a	50 ^a	84ª	16 ^a	50 ^a	84ª	
J2302+4442	GB		•••	•••	2.59	3.29	4.31	1.06	1.41	1.84		•••	•••	-1.51
J2317+1439	AO	4.81	7.20	9.96				0.26	0.45	0.80		•••		-2.35
J2322+2057	AO	1.37	1.94	3.54	•••	•••	•••	0.14	0.26	0.72	0.31	0.32	1.06	-1.70

Notes

 $_{\cdot}^{a}$ In flux density columns, 16, 50, and 84 refer to 16th, 50th, and 84th percentile of epoch-averaged flux density values.

b Calculated from S_{800} and S_{1400} for GB pulsars, S_{430} and S_{1400} for AO pulsars with 430 MHz data, and S_{1400} and S_{2000} for other pulsars.

source. The noise signals were checked against the continuum calibrator approximately once per month at each observatory. Thus, our flux density measurements depend directly on our assumptions about the continuum calibrator flux density.

For continuum calibration, we used the compact radio source J1445+0958 (B1442+101) for all GUPPI observations and all PUPPI observations after MJD 56619 (2013 November 29). We only used data calibrated with this source in the flux density analysis. The VLA calibrator manual gives the flux density of J1445+0958 as 2.60, 1.20, 0.73 0.40, and 0.10 Jy at wavelengths of 20.0, 6.0, 3.7, 2.0, and 0.7 cm, respectively. We modeled this using the analytic expression $\log S = \sum_{i=0}^{3} a_i (\log \nu_{\rm GHz})^i$, where $\nu_{\rm GHz}$ is the radio frequency in gigahertz and the coefficients for J1445+0958 are $a_0 = 0.389314$, $a_1 = -0.0280647$, $a_2 = -0.600809$, and $a_3 = 0.0262127$.

8.2. Data Checks and Cleaning

Flux density measurements are particularly susceptible to calibration errors, so we undertook further checks of the data used for this purpose.

The S/N of a pulsar observation is expected to be $S/N = SG/T_{sys}\sqrt{2Bt}\sqrt{(P-w)/w}$, where S, G, T_{sys} , B, t, P, and w are the pulsar flux, telescope gain, system temperature, bandwidth, observing time, pulse period, and pulse width, respectively, and where $\sqrt{(P-w)/w}$ is a proxy for a general pulse-shape-dependent factor. For a given telescope, receiver, and pulsar, at a given radio frequency, the ratio $(S/[S/N])\sqrt{2Bt}$ should be constant (after considering small variations due to radiometer noise and variations in G and T_{sys} due to telescope elevation). Radio-frequency interference, calibration errors, and other defects in the data can cause this ratio to vary. We used this to flag potentially discrepant flux density values. We removed any data point for which this ratio was less than 0.75 or more than 1.75 times the median value for that frequency and nearby frequencies at low S/N, with a gradually increasing allowed upper value for high S/N (analyzed over ranges of 100 MHz above 1 GHz, 50 MHz for the GBT 820 MHz receiver, and 10 MHz for the Arecibo 327 and 430 MHz receivers). At $\nu > 2300$ MHz, we used a lower limit on the ratio of 0.50 rather than 0.75. Further, we entirely eliminated any observation for which five or more individual flux values were flagged as potentially discrepant. These specific choices were based on empirical analysis of the data. They eliminated obvious outliers while allowing us to retain most of the flux density measurements.

8.3. Flux Density Measurement Results

For each epoch, we fit the observed set of narrowband flux values to a power law, $S_{\rm obs}(\nu) = S_{\nu_0} (\nu/\nu_0)^{\alpha}$. Here, S_{ν_0} is the fit flux at fiducial frequency ν_0 and α is the spectral index. We used fiducial frequencies of 430, 800, 1400, and 2000 MHz, chosen for their locations near the centers of the observing bands and, in some cases, because they are standard frequencies used in pulsar catalogs. We calculated separate values of S_{ν_0} and α for each receiver at each observing epoch (defined as observations within a three-day span).

For most pulsars, the values of α within these single-receiver, single-epoch fits varied widely due to diffractive scintillation within the receiver bands; we do not use those values further.

Table 6 reports the median observed flux density for each pulsar and each receiver, along with 16th and 84th percentile values. The table also includes spectral indexes calculated using the median flux density values in two bands (as specified in the table). For the two pulsars observed at both Arecibo and GBT (PSRs J1713+0747 and B1937+21), we analyzed the measurements from the observatories separately as a check against systematic errors. Their S_{1400} measurements show good agreement between the two observatories.

PSR J1713+0747 shows a significant difference between the spectral index calculated from Arecibo values of S_{1400} and S_{2000} and the spectral index calculated from GBT values of S_{800} and S_{1400} . This suggests that a single power law is not sufficient to model the flux density across a wide range of frequencies. PSR B1937+21 also shows a difference in spectral indexes between the two observatories, albeit somewhat smaller (and in the opposite direction) than that of J1713+0747.

Because our flux density analysis only includes measurements from observations that yielded good narrowband TOA values, it excludes observations in which the pulsar had a very low S/N or was not visible at all. This could potentially bias our measurements high (because low flux density values due to, e.g., extreme scintillation are excluded). Furthermore, we used a constant template profile for the narrowband TOA measurements, which assumes that the true profile shape does not evolve with frequency across the band; the amplitude, and thus the estimated flux density, will depend on the degree to which this assumption holds. We believe both of these factors only have a small effect in our reported measurements, but a detailed analysis of these biases is beyond the scope of the present work.

The spectral indexes of sources observed at Arecibo at 1400 and 2000 MHz tend to have smaller magnitudes than the spectral indexes of other pulsars. This is almost certainly a selection effect. We preferentially observe Arecibo pulsars with this combination of receivers, but only when the pulsar is strong enough to be consistently detected with high S/N at 2000 MHz. This implies that such sources have relatively high flux densities at 2000 MHz, and therefore relatively shallow spectra.

8.4. Comparison with Previous Work

A comparison between our S_{1400} measurements and previously reported values for 41 pulsars is given in Figure 5. There is some scatter in the values, likely attributable to scintillation-induced variations in flux density measurements, particularly in previous measurements that might be based on a small number of samples. The median ratio of S_{1400} from our measurements to the S_{1400} of previous measurements was 0.82, and the average value of this ratio was 1.19. The latter is evidently dominated by a few sources with the most significant discrepancies. The most significant outlier values are for PSR J1911+1347, for which we report a median $S_{1400} = 0.86$ mJy, while the previous reported value was 0.08 mJy, more than an order of magnitude lower (Lorimer et al. 2006); and for PSR J2317+1439, for which we report a median $S_{1400} = 0.45 \,\mathrm{mJy}$, while the previous reported value was 4 ± 1 mJy, more than an order of magnitude greater (Kramer et al. 1998). The reason for the relatively large discrepancies in reported values for these two pulsars is not known.

We made similar comparisons between our flux density measurements and cataloged values at 430 MHz (11 pulsars) and 2000 MHz (1 pulsar). The results were comparable to those at 1400 MHz: general agreement with modest scatter between new and previous measurements.

⁵⁴ https://science.nrao.edu/facilities/vla/observing/callist

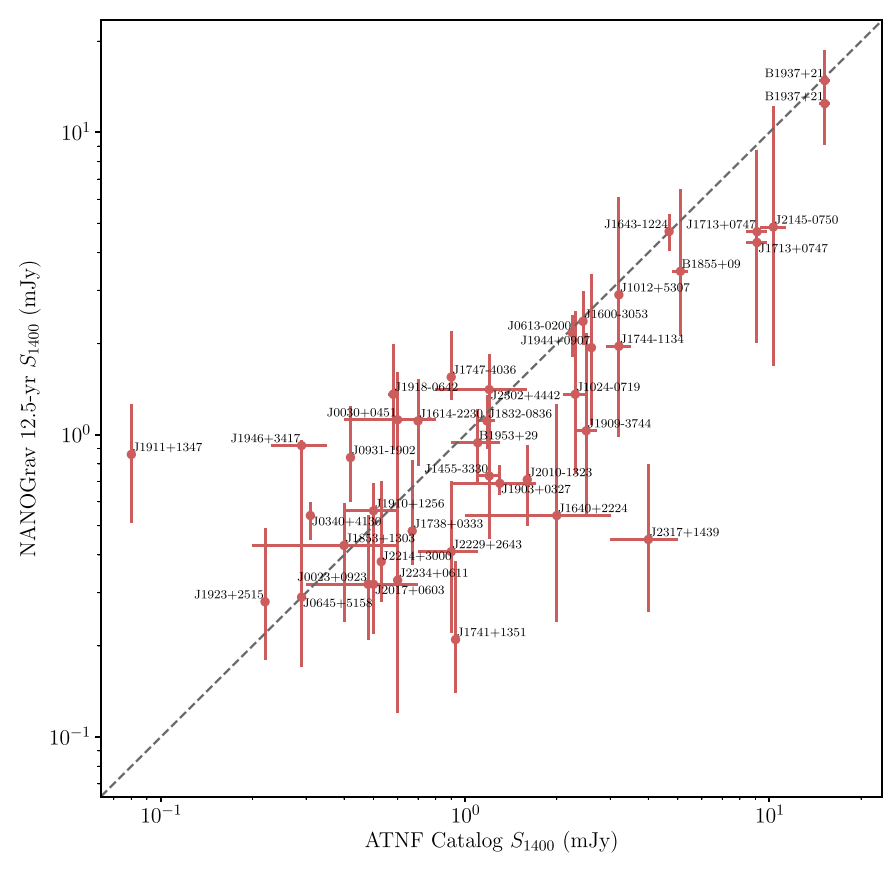


Figure 5. Comparison of 1400 MHz flux density measurements (S_{1400}) from the present paper (vertical axis) with values in the ATNF pulsar catalog (horizontal axis; Manchester et al. 2005, version 1.63). Vertical error bars indicate the central 68% of measured flux density values (Table 6). Horizontal error bars, where present, indicate the uncertainties reported in the ATNF pulsar catalog. Two pulsars are shown twice (J1713+0747 and B9137+21), with similar values, because we made separate analyses of our Arecibo and GBT measurements.

Table 7Comparison of Spectral Indexes

PSR	Obs.	NG12.5	Frail et al. (2016)			
		α	α	σ_{α}		
J0030+0451	AO	-1.39	-1.93	0.15		
J1643-1224	GB	-1.82	-1.64	0.06		
J1747-4036	GB	-2.66	-2.81	0.22		
B1937+21	AO	-2.72	-2.51	0.17		
B1937+21	GB	-2.39	-2.51	0.17		
J1944+0907	AO	-1.92	-3.03	0.06		
B1953+29	AO	-2.16	-1.77	0.09		
J2145-0750	GB	-1.92	-1.47	0.61		
J2317+1439	AO	-2.35	-0.86	0.12		

Shaifullah (2017, herein S2017) reports measurements of spectral indexes of a dozen MSPs at Arecibo using the 327 and 1400 MHz receivers. Of those, five MSPs were observed for a large number of epochs (thus mitigating scintillation issues). Within that group, two overlap with the present work, and both show good agreement with our measurements: for PSR J1453 +1902, we find $\alpha=-1.92$, and S2017 reports $\alpha=-1.7\pm0.4$; for J2322+2057, we find $\alpha=-1.70$, and S2017 reports $\alpha=-1.7\pm0.1$. (Other pulsars in S2017 with fewer observations show larger discrepancies.)

Frail et al. (2016) reported spectral indexes of many pulsars calculated by combining Giant Metrewave Radio Telescope (GMRT) 150 MHz observations with measurements in the

literature at other frequencies. A summary is presented in Table 7, which lists the spectral indexes from the present work (NG12.5), along with the spectral indexes and their uncertainties, σ_{α} reported by Frail et al. (2016). Many measurements are in agreement, but a few are not. It is not clear whether this is because of differences in observing frequency (and the possible inadequacy of a single power law to describe flux density) or whether it is caused by something else.

9. Summary and Conclusions

In this paper, we have introduced the NANOGrav 12.5 yr data set, which contains TOAs and timing models for 47 MSPs with baselines between \sim 2 and \sim 13 yr (Section 2). In particular, the present work follows in the footsteps of NANOGrav's three preceding data releases (NG5, NG9, and NG11). We have given the TOAs discussed in this paper the designation "narrowband" to distinguish them from the "wideband" data set that uses a number of new developments to process the same pulse profile data (see the parallel paper, Alam et al. 2020).

These data introduced two new pulsars into our PTA (PSRs J1946+3417 and J2322+2057) and extended our baseline by 1.5 yr. A number of new procedural changes and quality-control measures were introduced over NG11. In addition to the wideband processing, for this data set we:

1. Removed low-amplitude artifact images from the profile data that were introduced by the interleaved samplers of the ADCs (Section 2.3).

- 2. Automated and systematized the timing analysis procedure with Jupyter notebooks (Section 3).
- 3. Excised whole epochs of data based on their disproportionately large influence on timing fit χ^2 , as indicated by an F test (Section 2.5).
- 4. Identified and excised specious TOAs by examining calibration scans and flux densities (Section 2.5).
- 5. Introduced -cut flags that document why a TOA has been removed from the data set (Section 2.5).
- 6. Transitioned to the ENTERPRISE PTA analysis software for noise modeling (Section 3.3).
- Cross-checked timing results with the new TEMPO- and TEMPO2-independent pulsar timing software PINT (Section 4).
- 8. Included per-TOA flux density measurements (Section 8).

Some of these changes led to improvements in the white-noise-model parameters, as indicated by a reanalysis of the data in NG11 compared to the 11 yr "slice" of the present data set (Section 3.4). The red noise detected in 11 sources in NG11 continues to be present (Section 3.3). Red noise is also detected in an additional three pulsars—PSRs J1744–1134, J1853 +1303, and J2317+1439—the first and third of which are bright, precisely timed pulsars with some of the longest baselines in the data set. A number of other pulsars have subthreshold hints of red noise, which may become significant in future data sets.

Two of the main astrophysical results from this data set—the observation of a second chromatic ISM event in PSR J1713 +0747 (Lam et al. 2018a) and the discovery that PSR J0740 +6620 is the most massive, precisely measured neutron star known to date (Cromartie et al. 2020)—were published prior to the present work. Additionally, the entire data set was analyzed for pulse phase jitter in Lam et al. (2019). Deneva et al. (2019) used data from this release to compare the radio timing stability of PSR B1937+21 with that seen by the NICER X-ray instrument, and Stovall et al. (2019) used a superset of these observations to solve the 3D orbit of PSR J2234+0611. In Section 5, we highlighted a number of other new NANOGrav measurements, which include the first published measurements of trigonometric parallax for PSRs J1832-0836 and J2322 +2057, of \dot{x} for J0613-0200 and J2229+2643, and of h_3 indicating a marginally detected Shapiro delay in J2145–0750.

NANOGrav is committed to continued public data releases, both for individual studies of high-precision pulsar timing and for the sake of gravitational wave detection.⁵⁵ Analyses of these data to model a variety of gravitational wave signals will be presented in forthcoming publications, with our latest results from searching for a stochastic background presented in Arzoumanian et al. (2020). Furthermore, advanced noise modeling techniques in which bespoke models are applied to each pulsar are anticipated to further increase our sensitivity and will also be presented elsewhere (J. S. Simon et al. 2020, in preparation). Increasing the number of pulsars in the array has the largest impact on determining the prospects for detection of the stochastic background. To this end, we are already synthesizing our next data set, which will come with the single largest increase in the number of pulsars (\sim 50%) because we doubled the size of the array between NG5 and NG9. The concomitant increase in the sensitivity and complexity of our

PTA analyses promises to deliver an exciting upcoming few years of nanohertz gravitational wave astrophysics.

Author contributions. The alphabetical-order author list reflects the broad variety of contributions of authors to the NANOGrav project. Some specific contributions to this paper, particularly incremental work between NG11 and the present work, are as follows.

Z.A., H.B., P.T.B., H.T.C., M.E.D., P.B.D., T.D., R.D.F., E. C.F., E.F., P.A.G., M.L.J., M.A.L., D.R.L., R.S.L., M.A.M., C. N., D.J.N., T.T.P., S.M.R., K.S., I.H.S., J.K.S., R.S., S.J.V., and W.Z. each ran at least 10 sessions and/or 20 hr of observations for this project. M.F.A., K.E.B., K.C., R.S.C., R. L.C., W.F., Y.G., D.H., C.J., K.M., B.M.X.N., J.R., and M.T. were undergraduate observing-team leaders, supervised by F. C., T.D., D.L.K., J.K.S., and X.S.

P.T.B., P.B.D., M.E.D., M.T.L., J.L., M.A.M., T.T.P., and K.S. developed and refined procedures and computational tools for the timing pipeline. H.B., P.R.B., H.T.C., M.E.D., P.B.D., E.F., D.C.G., M.L.J., M.T.L., M.A.M., D.J.N., N.S.P., T.T.P., S.M.R., I.H.S., and K.S. generated and checked timing solutions for individual pulsars. M.E.D., P.B.D., P.A.G., M. T.L., D.J.N., T.T.P., and K.S. performed the various data quality checks described in Section 2.5.

M.T.L. developed the systematic pipeline for developing timing models. M.V. assisted in implementing the outlier analysis code into the 12.5 yr data set analysis. P.B.D. wrote observing proposals, performed calibration and TOA generation, coordinated the data flow, developed and implemented the methodology used to mitigate the artifact images in the data, and produced the finalized versions of the data files for public release. P.B.D. and K.S. coordinated GBT observations. M.E.D. coordinated the development of the data set and the writing of this paper, wrote much of the text, and coordinated observations at the Arecibo Observatory. D.J.N. and T.T.P also aided in coordination of data analyses and paper writing. J.S. and S.R.T. assisted in interpreting the red-noise modeling results. J.S.H. performed the noise parameter comparison between the 11 yr data set and 11 yr "slice" analysis of the 12.5 yr data set. J.L. undertook the comparison between PINT and TEMPO. S.C. performed the comparison of astrometric parameters between data sets. J.A.G. and D.J.N. produced the flux density analysis. M.E.D. and E.F. undertook the analysis of binary systems. T.T.P. and S.M.R. also contributed text, especially for the introduction and conclusion. H. T.C. and T.T.P. produced the timing residual plots in the Appendix. N.G.D. oversaw and maintained much of the computational infrastructure related and essential to this work, including installing and setting up the outlier analysis software, regularly updating TEMPO, and maintaining the server with the Jupyter notebooks used in our systematic analysis pipeline.

The NANOGrav project receives support from National Science Foundation (NSF) Physics Frontiers Center award number 1430284. The Arecibo Observatory is a facility of the NSF operated under cooperative agreement (#AST-1744119) by the University of Central Florida (UCF) in alliance with Universidad Ana G. Méndez (UAGM) and Yang Enterprises (YEI), Inc. The Green Bank Observatory is a facility of the NSF operated under cooperative agreement by Associated Universities, Inc. The National Radio Astronomy Observatory is a facility of the NSF operated under cooperative agreement by Associated Universities, Inc. Part of this research was carried out at the Jet Propulsion Laboratory, California Institute of Technology, under

⁵⁵ Data from this paper are available at http://data.nanograv.org and preserved on Zenodo at doi:10.5281/zenodo.4312297.

a contract with the National Aeronautics and Space Administration. Pulsar research at UBC is supported by an NSERC Discovery Grant and by the Canadian Institute for Advanced Research. T.T.P. acknowledges support from the MTA-ELTE Extragalactic Astrophysics Research Group, funded by the Hungarian Academy of Sciences (Magyar Tudományos Akadémia), that was used during the development of this research. W. W.Z. is supported by the CAS Pioneer Hundred Talents Program and the Strategic Priority Research Program of the Chinese Academy of Sciences grant No. XDB23000000.

We thank the telescope operators and all the staff at the Arecibo Observatory and the Green Bank Observatory for the essential role they played in collecting the data for this data release. We also thank the anonymous referee for their very useful comments that helped to improve the quality of this paper. The NANOGrav Collaboration dedicates this work to the Arecibo Observatory, its employees and staff, and the many students, teachers, and others who have drawn inspiration from it.

Facilities: Arecibo Observatory, Green Bank Observatory. Software: ENTERPRISE (Ellis et al. 2019), libstempo (Vallisneri 2020), matplotlib (Hunter 2007), nanopipe (Demorest 2018), piccard (van Haasteren 2016), PINT (Luo et al. 2019), PSRCHIVE (Hotan et al. 2004, van Straten et al. 2011), PTMCMC (Ellis & van Haasteren 2017), PyPulse (Lam 2017), Tempo (Nice et al. 2015), Tempo2 (Hobbs & Edwards 2012), tempo_utils.

Appendix Averaged Residuals

This appendix includes Figures 6–52 showing timing residuals and DM variations for each pulsar in our data set.

DM variations. In panel (a) of each of the appendix figures, we plot the mean-subtracted DM time series, where each point

represents a DM parameter in the DMX model (Section 3.2). The division of each timing baseline into DMX epochs is described in Section 3.2, and the epochs are typically six days in length or less (usually one day for Arecibo observations), except in the earliest data. The mean-subtracted DM values are plotted in part because it allows us to segregate the uncertainty in the average DM, which arises due to covariance with the FD parameters and template pulse profiles, from the uncertainties in the DMX parameters that are shown in the figures.

Timing residuals. As described in Section 2, each observation comprises many simultaneously obtained narrowband TOAs. We plot the residual arrival times (observed minus that predicted from the timing model) for each pulsar in multiple ways described below. In each residual plot, linear and quadratic trends have been removed, as they are completely covariant with the pulsar's rotation frequency and frequency derivative in the timing model, and hence would be absorbed.

Residuals from every TOA measurement are plotted in panel (b) of each figure. The color of each point encodes the receiver as in Figure 1: 327 MHz (red), 430 MHz (orange), 820 MHz (green), 1400 MHz (lighter blue for AO, darker blue for the GBT), 2100 MHz (purple). The predominant data acquisition back-end instrument over any given time period is indicated at the top of each figure, and vertical dashed lines indicate the times at which instruments changed. Averaged residuals of simultaneously measured TOAs are shown in panels (c) and (d); these were computed using the procedure described in Appendix D of NG9. The full vertical range of these residuals is shown in panel (c), while panel (d) shows a close-up of the low residuals. For pulsars with red noise above our defined threshold, red-noise Bayes factor B > 100 (Table 2), panel (e) shows whitened timing residuals, which have the red-noise contribution subtracted from the averaged residuals.

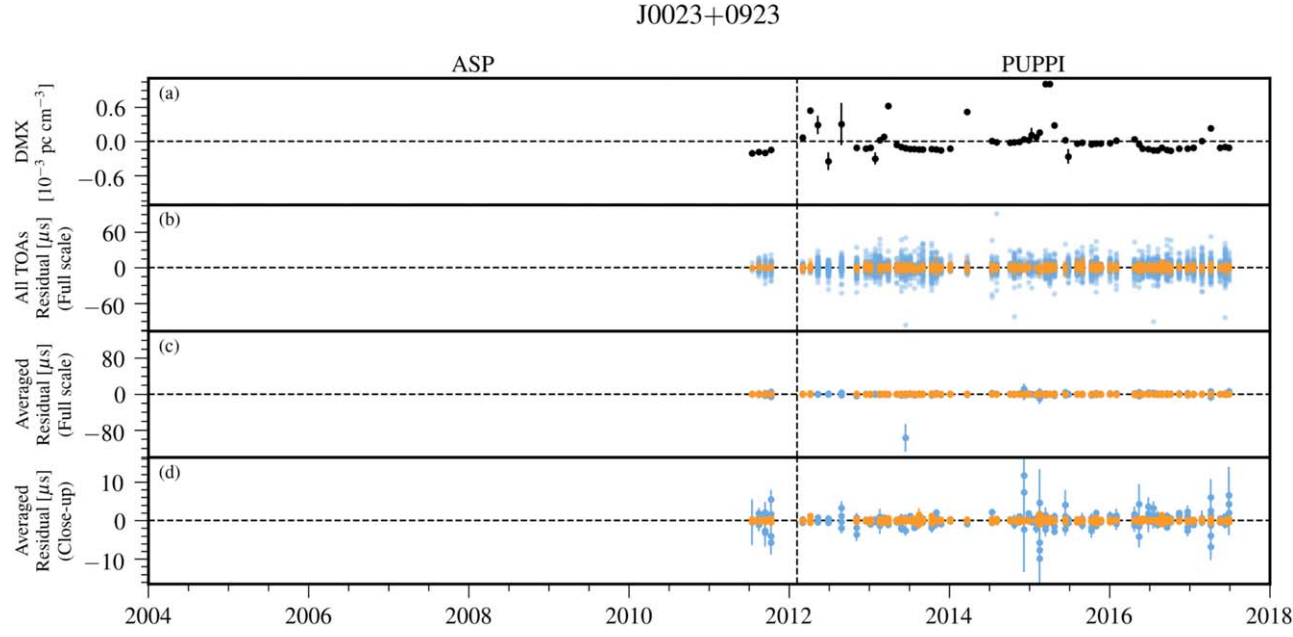


Figure 6. Timing residuals and DM variations for PSR J0023+0923. See the Appendix text for details. In the residual plots, colored points indicate the receiver of each observation: 430 MHz (orange) and 1.4 GHz (light blue). (a) Variations in DMX. (b) Residual arrival times for all TOAs. Points are semitransparent; dark regions arise from the overlap of many points. (c), (d) Average residual arrival times shown full scale (panel c) and close-up of low residuals (panel d).

⁵⁶ https://github.com/demorest/tempo_utils, git commit 51e0d9c on 2018 July 17.

J0030 + 0451

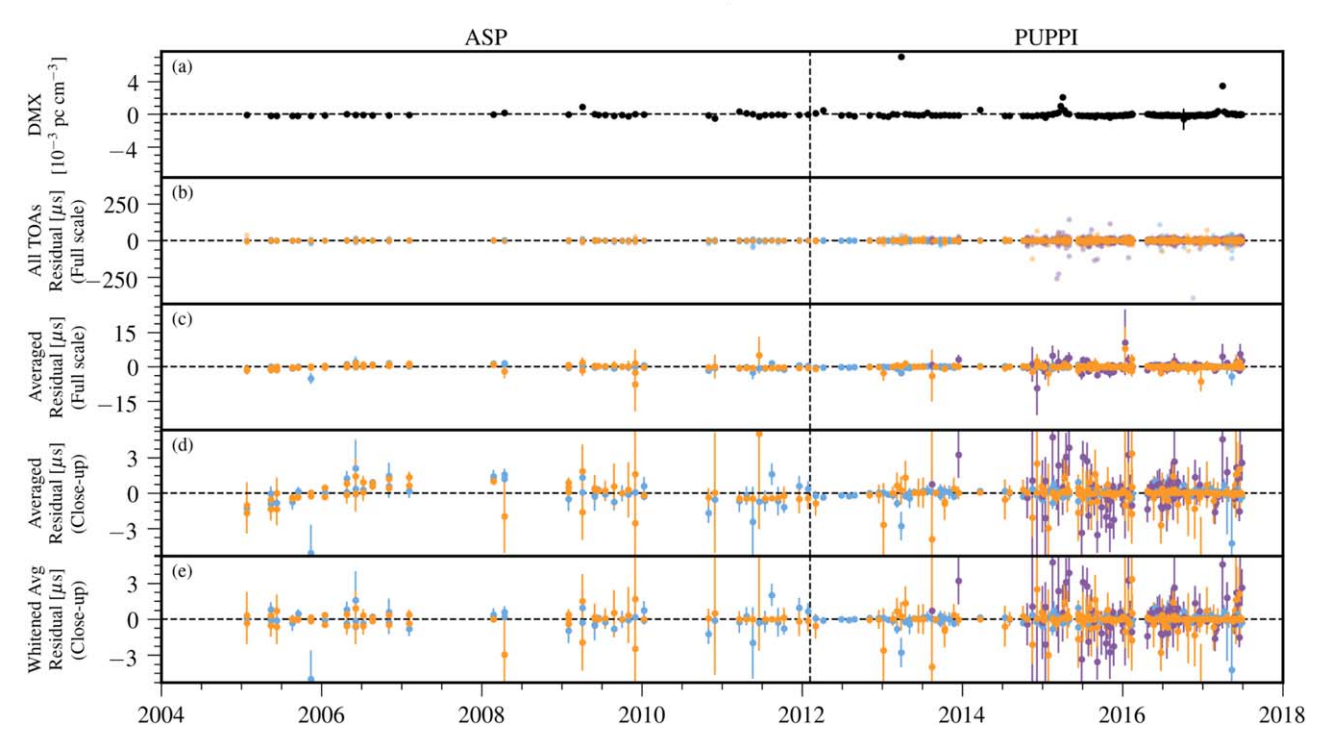


Figure 7. Timing residuals and DM variations for PSR J0030+0451. See the Appendix text for details. In residual plots, colored points indicate the receiver of each observation: 430 MHz (orange), 1.4 GHz (light blue), and 2.1 GHz (purple). (a) Variations in DMX. (b) Residual arrival times for all TOAs. Points are semitransparent; dark regions arise from the overlap of many points. (c), (d) Average residual arrival times shown full scale (panel c) and close-up of low residuals (panel d). (e) Whitened average residual arrival times after removing the red-noise model (close-up of low residuals).

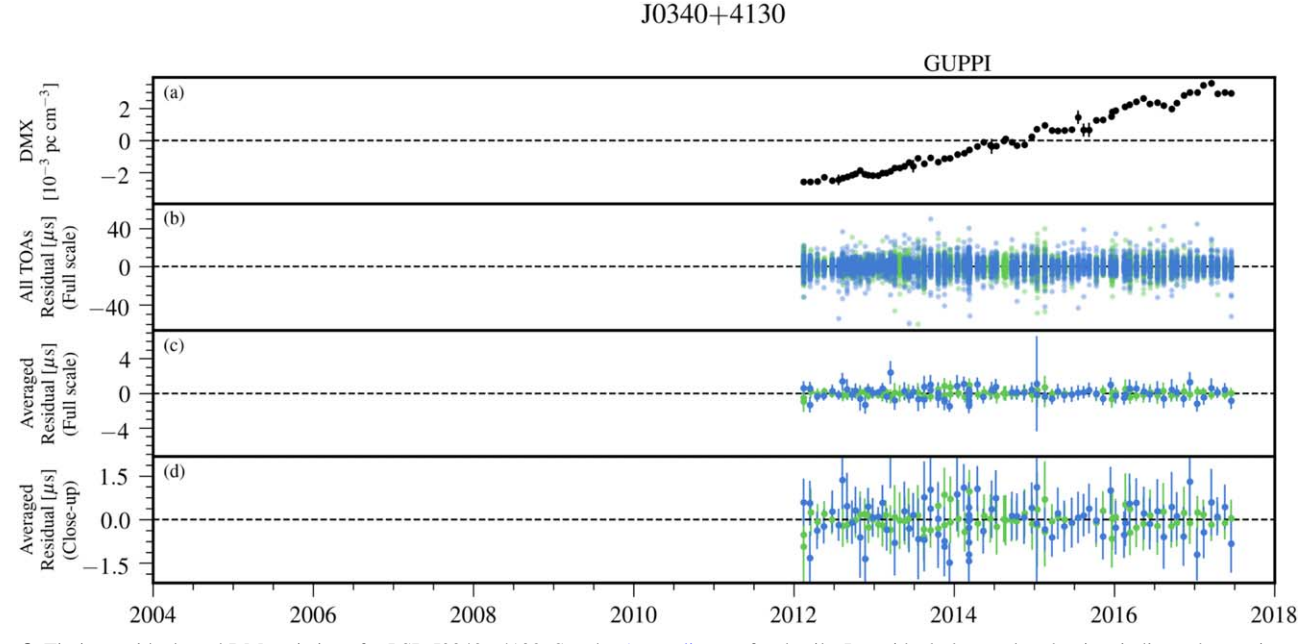


Figure 8. Timing residuals and DM variations for PSR J0340+4130. See the Appendix text for details. In residual plots, colored points indicate the receiver of each observation: 820 MHz (green) and 1.4 GHz (dark blue). (a) Variations in DMX. (b) Residual arrival times for all TOAs. Points are semitransparent; dark regions arise from the overlap of many points. (c), (d) Average residual arrival times shown full scale (panel c) and close-up of low residuals (panel d).

J0613-0200

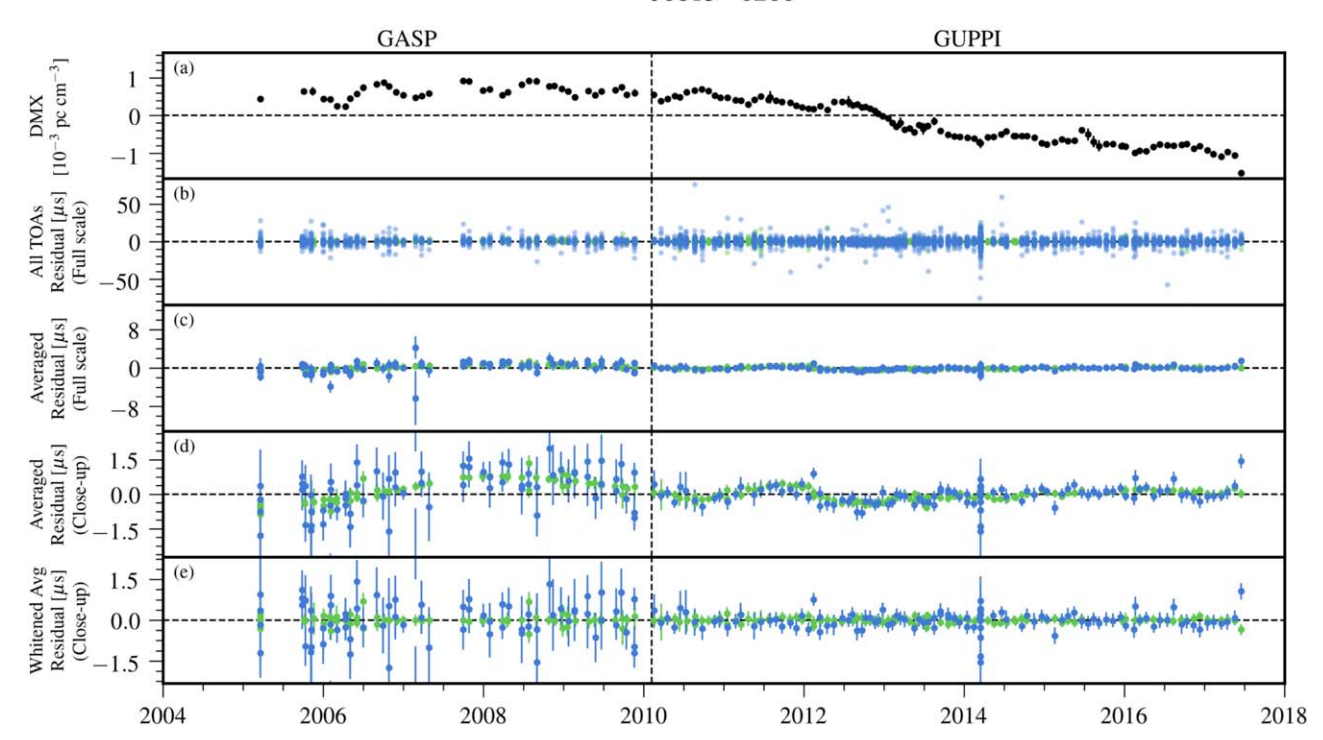


Figure 9. Timing residuals and DM variations for PSR J0613—0200. See the Appendix text for details. In residual plots, colored points indicate the receiver of each observation: 820 MHz (green) and 1.4 GHz (dark blue). (a) Variations in DMX. (b) Residual arrival times for all TOAs. Points are semitransparent; dark regions arise from the overlap of many points. (c), (d) Average residual arrival times shown full scale (panel c) and close-up of low residuals (panel d). (e) Whitened average residual arrival times after removing the red-noise model (close-up of low residuals).

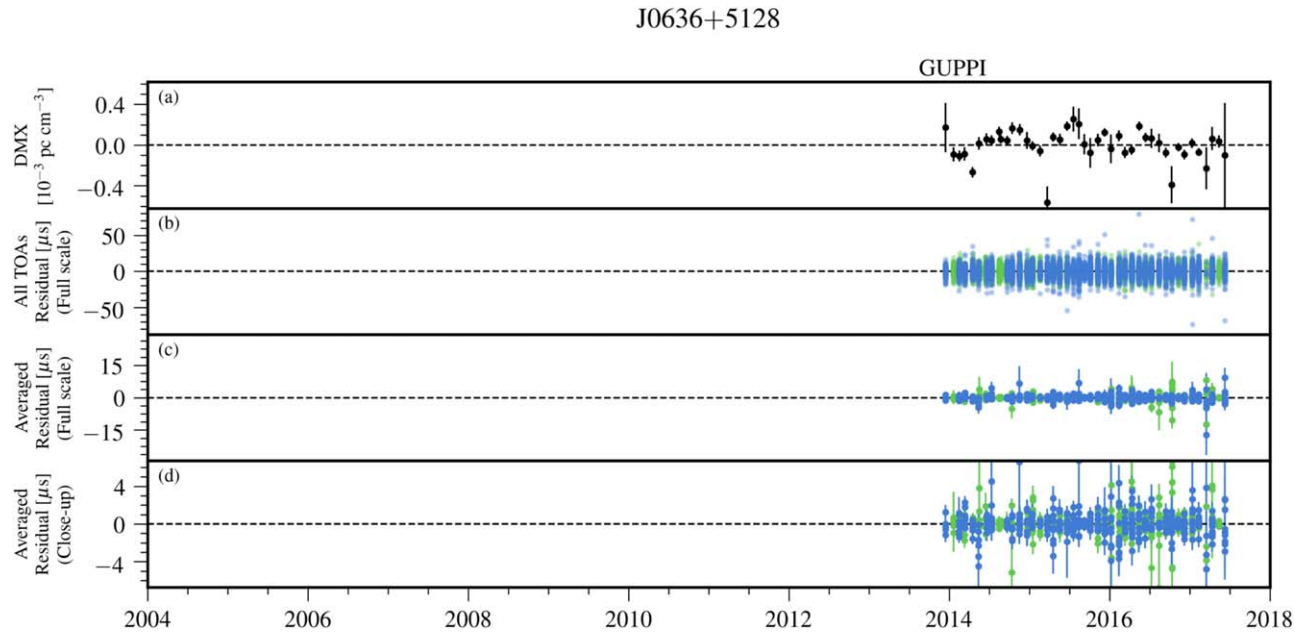


Figure 10. Timing residuals and DM variations for PSR J0636+5128. See the Appendix text for details. In residual plots, colored points indicate the receiver of each observation: 820 MHz (green) and 1.4 GHz (dark blue). (a) Variations in DMX. (b) Residual arrival times for all TOAs. Points are semitransparent; dark regions arise from the overlap of many points. (c), (d) Average residual arrival times shown full scale (panel c) and close-up of low residuals (panel d).

J0645+5158

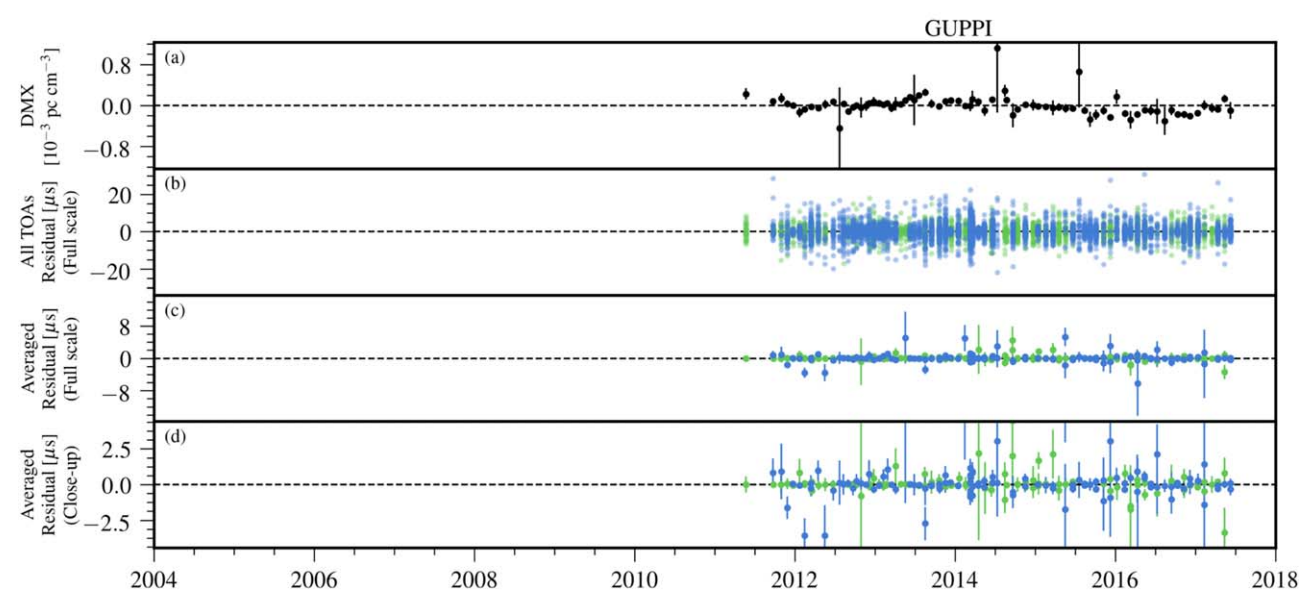


Figure 11. Timing residuals and DM variations for PSR J0645+5158. See the Appendix text for details. In residual plots, colored points indicate the receiver of each observation: 820 MHz (green) and 1.4 GHz (dark blue). (a) Variations in DMX. (b) Residual arrival times for all TOAs. Points are semitransparent; dark regions arise from the overlap of many points. (c), (d) Average residual arrival times shown full scale (panel c) and close-up of low residuals (panel d).

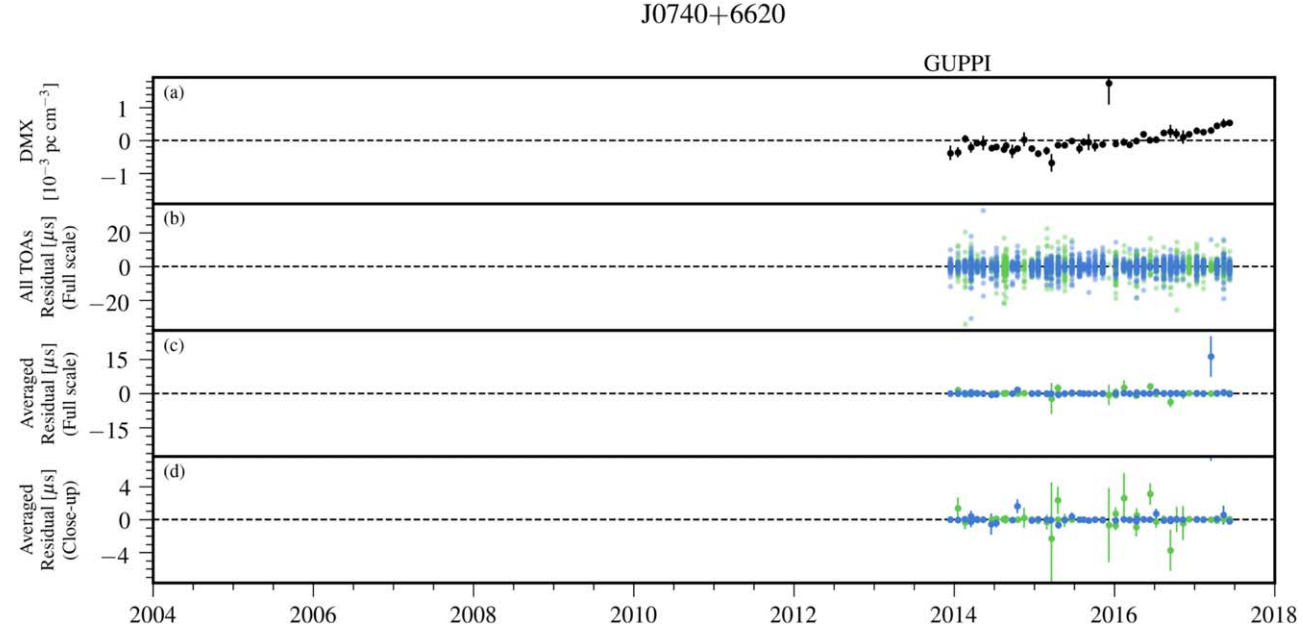


Figure 12. Timing residuals and DM variations for PSR J0740+6620. See the Appendix text for details. In residual plots, colored points indicate the receiver of each observation: 820 MHz (green) and 1.4 GHz (dark blue). (a) Variations in DMX. (b) Residual arrival times for all TOAs. Points are semitransparent; dark regions arise from the overlap of many points. (c), (d) Average residual arrival times shown full scale (panel c) and close-up of low residuals (panel d).

J0931-1902

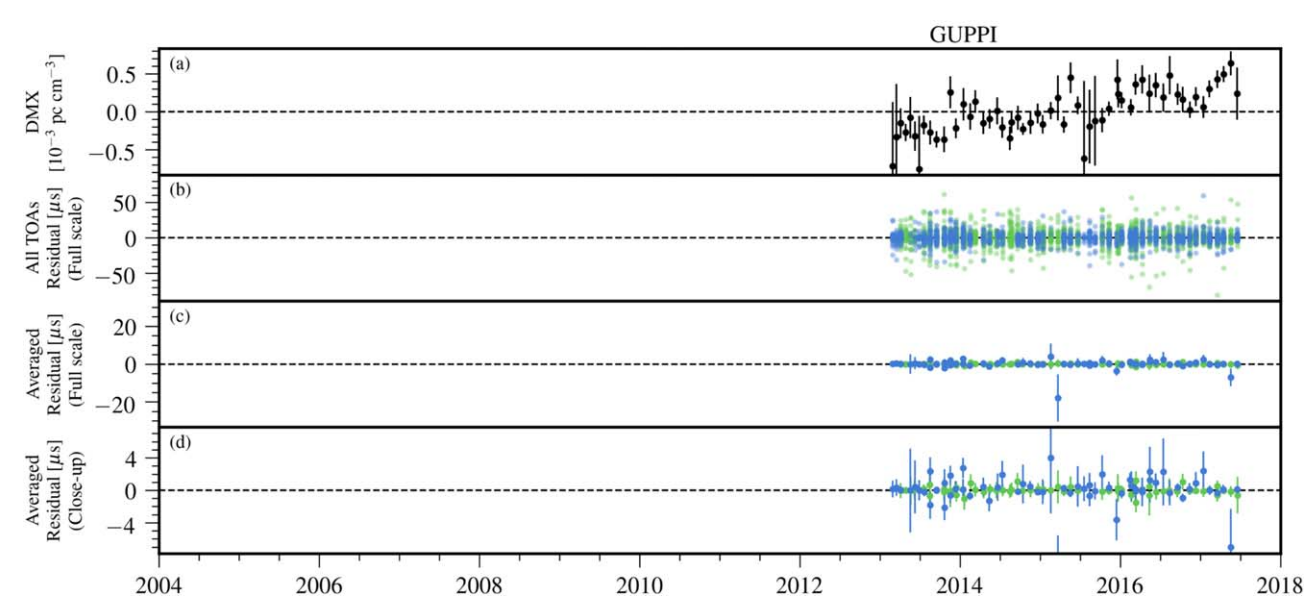


Figure 13. Timing residuals and DM variations for PSR J0931–1902. See the Appendix text for details. In residual plots, colored points indicate the receiver of each observation: 820 MHz (green) and 1.4 GHz (dark blue). (a) Variations in DMX. (b) Residual arrival times for all TOAs. Points are semitransparent; dark regions arise from the overlap of many points. (c), (d) Average residual arrival times shown full scale (panel c) and close-up of low residuals (panel d).

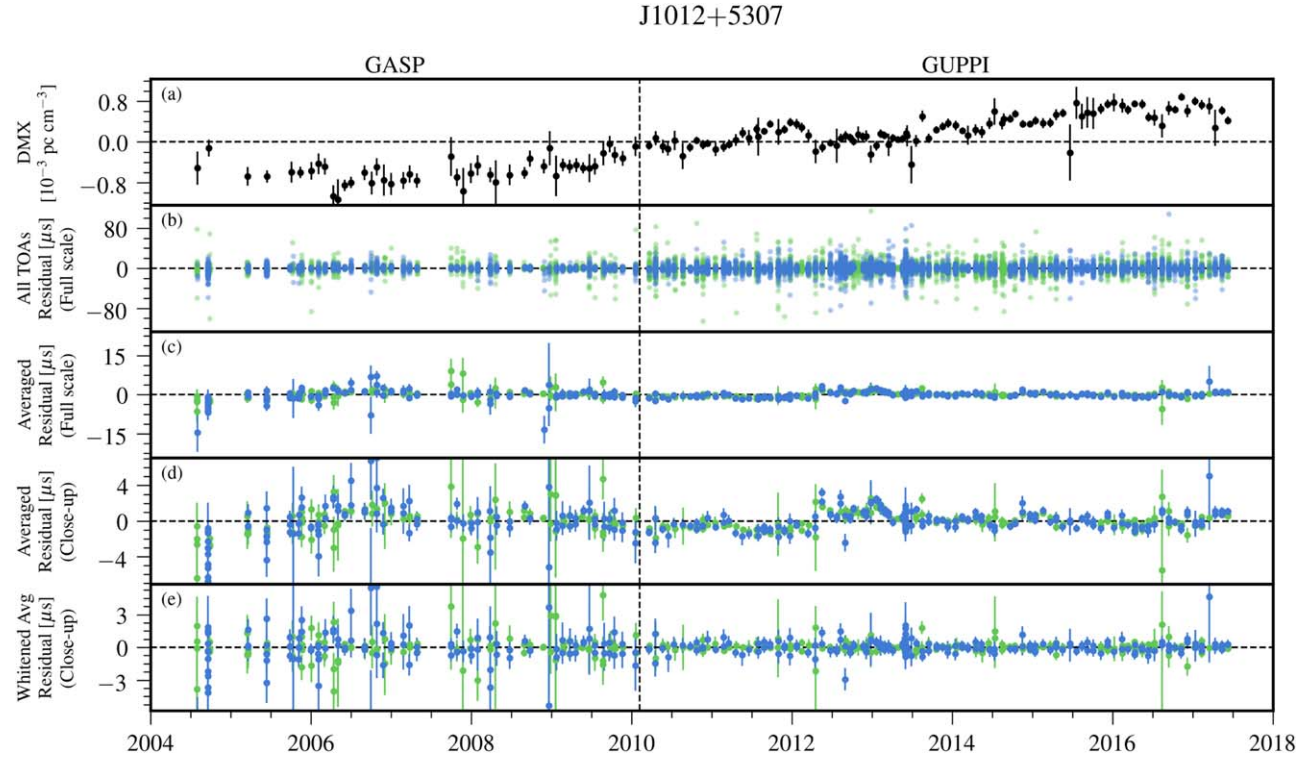


Figure 14. Timing residuals and DM variations for PSR J1012+5307. See the Appendix text for details. In residual plots, colored points indicate the receiver of each observation: 820 MHz (green) and 1.4 GHz (dark blue). (a) Variations in DMX. (b) Residual arrival times for all TOAs. Points are semitransparent; dark regions arise from the overlap of many points. (c), (d) Average residual arrival times shown full scale (panel c) and close-up of low residuals (panel d). (e) Whitened average residual arrival times after removing the red-noise model (close-up of low residuals).

J1024-0719

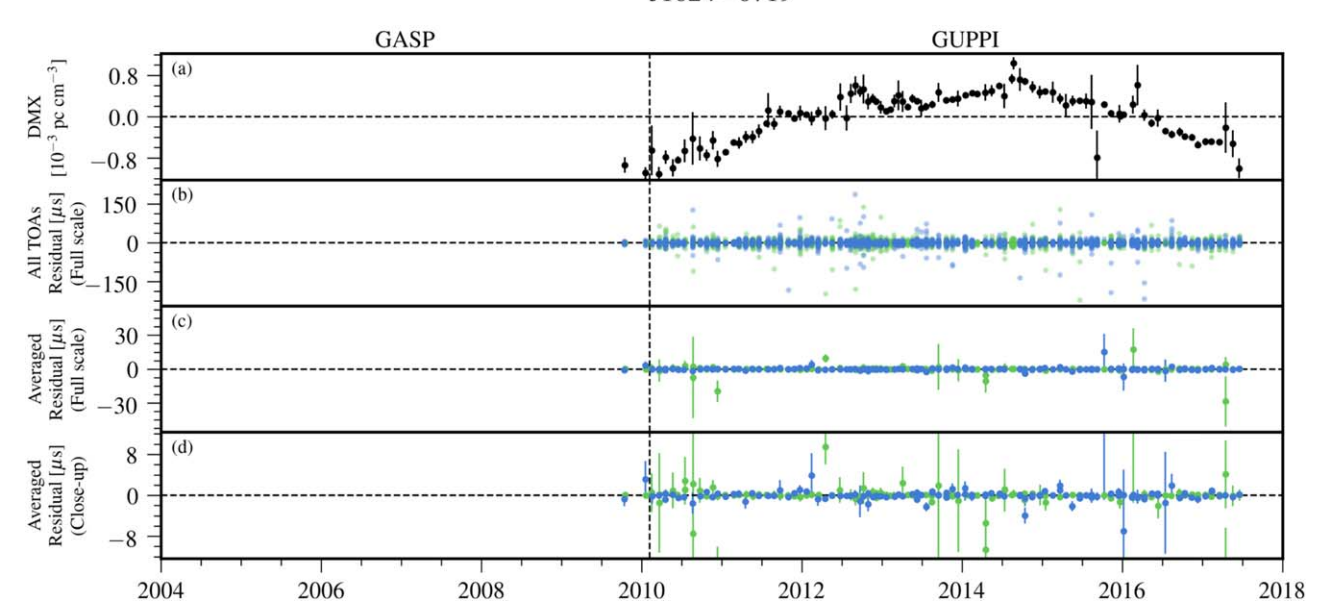


Figure 15. Timing residuals and DM variations for PSR J1024-0719. See the Appendix text for details. In residual plots, colored points indicate the receiver of each observation: 820 MHz (green) and 1.4 GHz (dark blue). (a) Variations in DMX. (b) Residual arrival times for all TOAs. Points are semitransparent; dark regions arise from the overlap of many points. (c), (d) Average residual arrival times shown full scale (panel c) and close-up of low residuals (panel d).

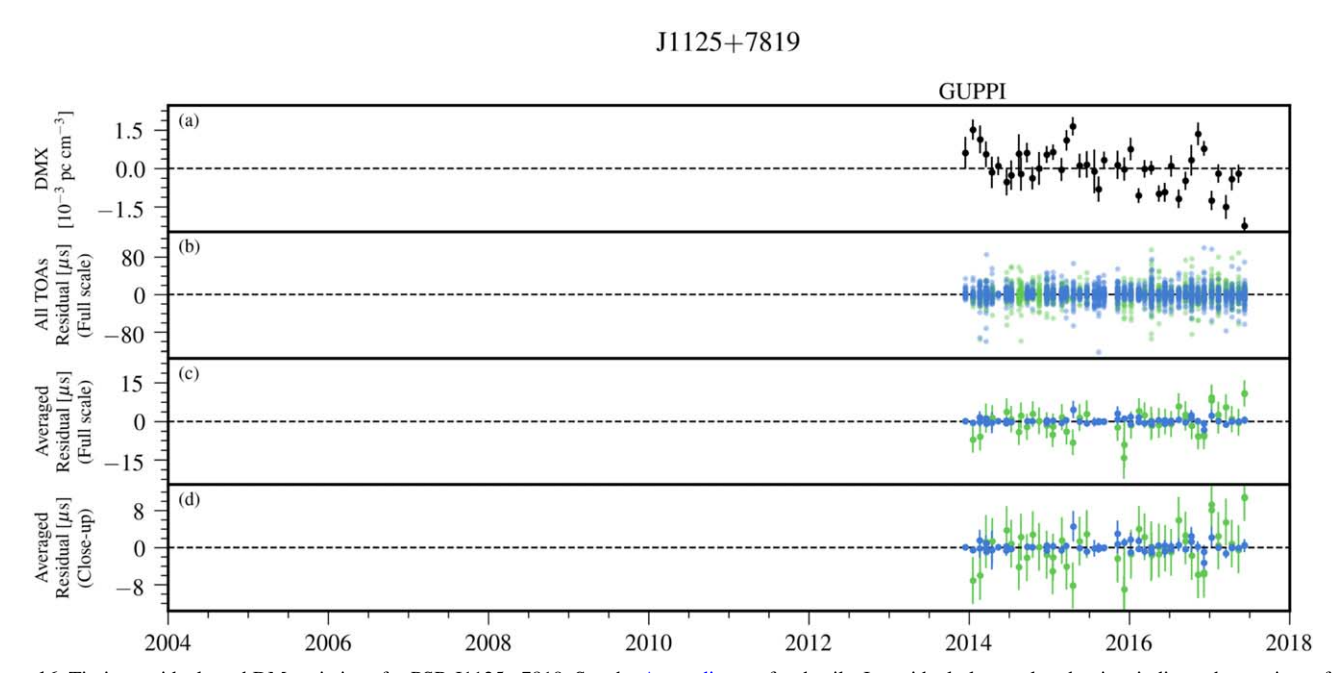


Figure 16. Timing residuals and DM variations for PSR J1125+7819. See the Appendix text for details. In residual plots, colored points indicate the receiver of each observation: 820 MHz (green) and 1.4 GHz (dark blue). (a) Variations in DMX. (b) Residual arrival times for all TOAs. Points are semitransparent; dark regions arise from the overlap of many points. (c), (d) Average residual arrival times shown full scale (panel c) and close-up of low residuals (panel d).

J1453+1902

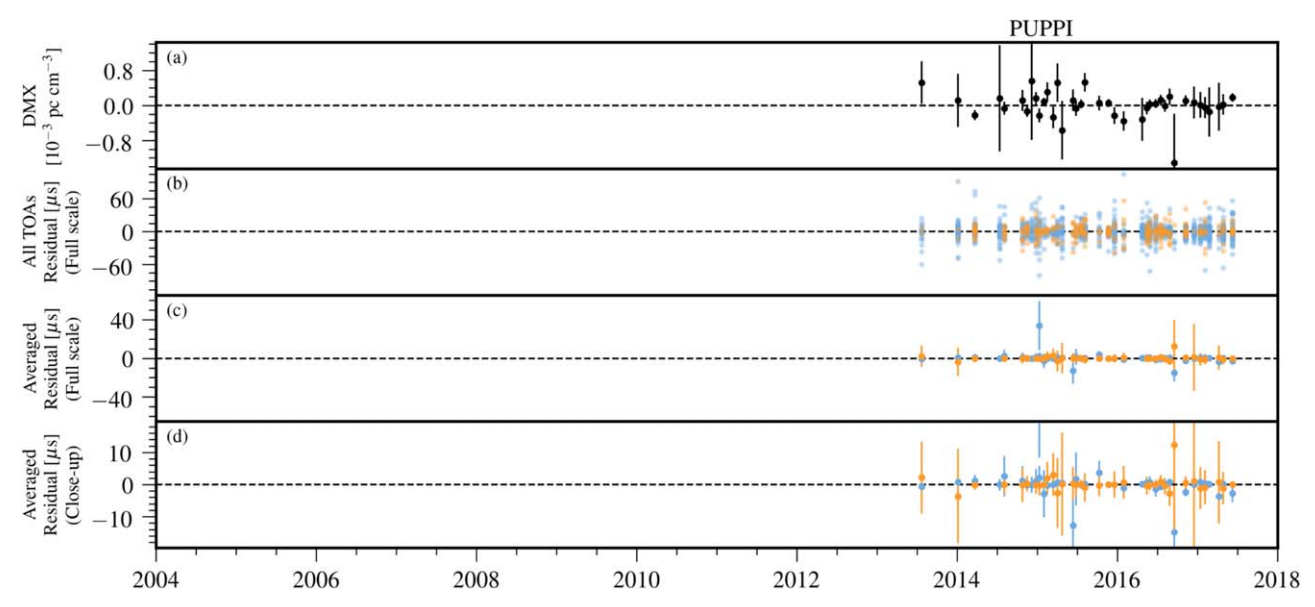


Figure 17. Timing residuals and DM variations for PSR J1453+1902. See the Appendix text for details. In residual plots, colored points indicate the receiver of each observation: 430 MHz (orange) and 1.4 GHz (light blue). (a) Variations in DMX. (b) Residual arrival times for all TOAs. Points are semitransparent; dark regions arise from the overlap of many points. (c), (d) Average residual arrival times shown full scale (panel c) and close-up of low residuals (panel d).

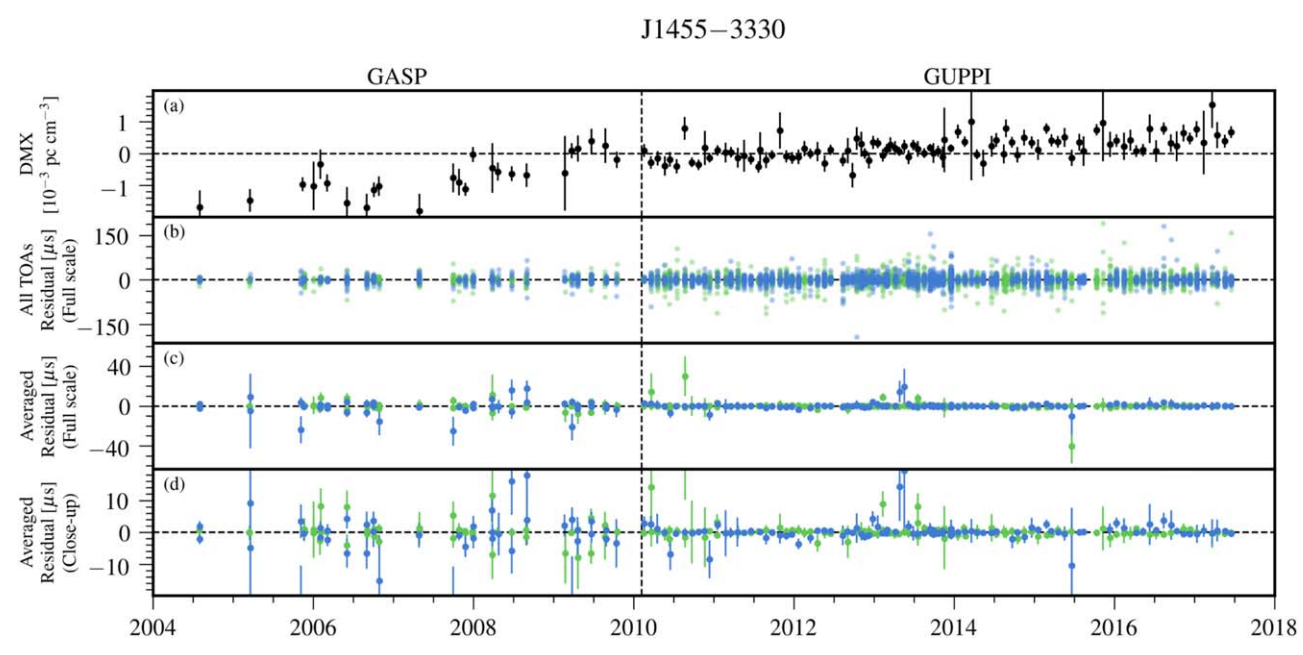


Figure 18. Timing residuals and DM variations for PSR J1455–3330. See the Appendix text for details. In residual plots, colored points indicate the receiver of each observation: 820 MHz (green) and 1.4 GHz (dark blue). (a) Variations in DMX. (b) Residual arrival times for all TOAs. Points are semitransparent; dark regions arise from the overlap of many points. (c), (d) Average residual arrival times shown full scale (panel c) and close-up of low residuals (panel d).



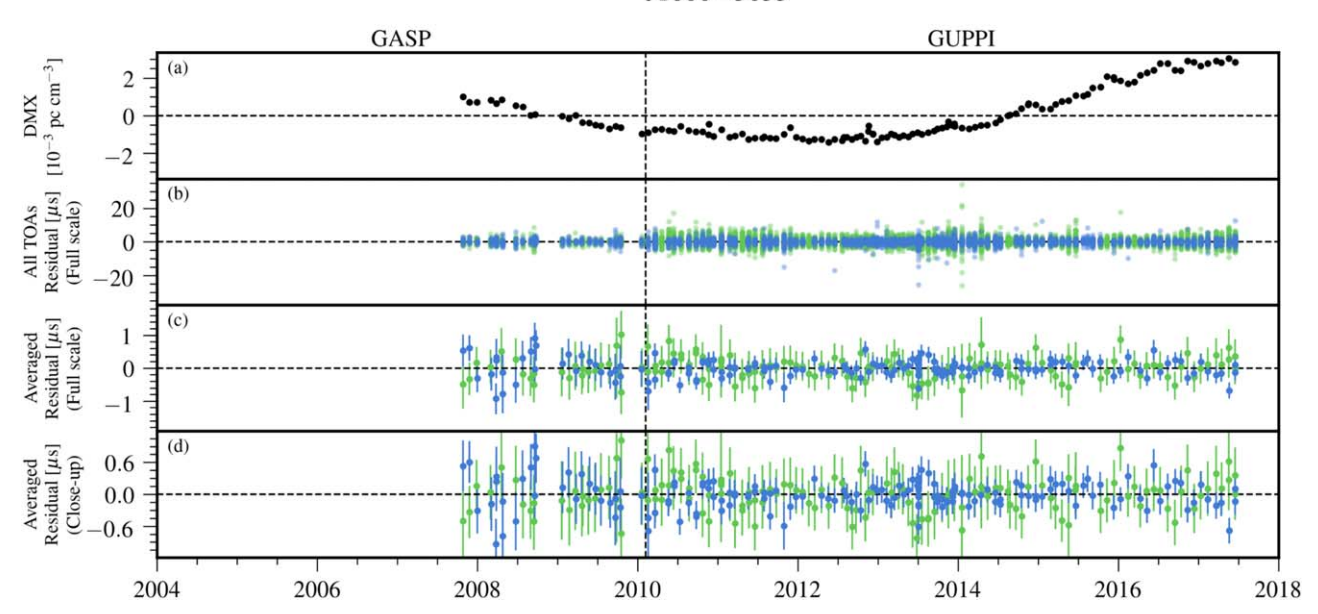


Figure 19. Timing residuals and DM variations for PSR J1600—3053. See the Appendix text for details. In residual plots, colored points indicate the receiver of each observation: 820 MHz (green) and 1.4 GHz (dark blue). (a) Variations in DMX. (b) Residual arrival times for all TOAs. Points are semitransparent; dark regions arise from the overlap of many points. (c), (d) Average residual arrival times shown full scale (panel c) and close-up of low residuals (panel d).

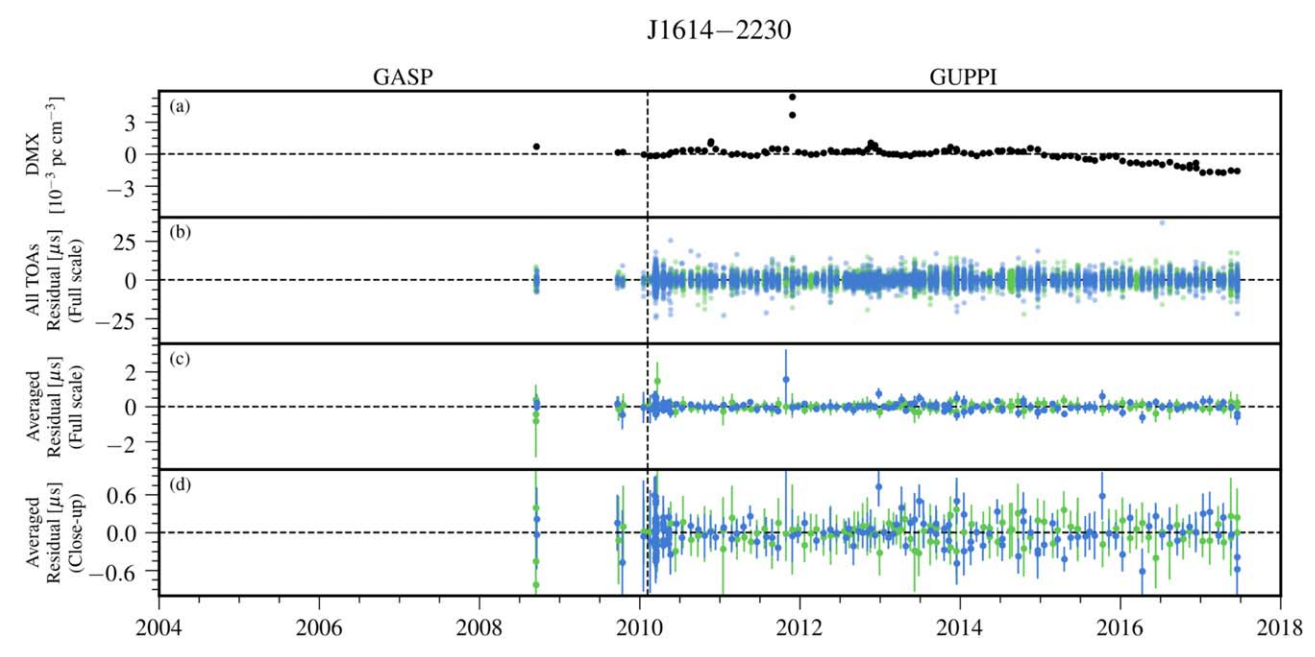


Figure 20. Timing residuals and DM variations for PSR J1614–2230. See the Appendix text for details. In residual plots, colored points indicate the receiver of each observation: 820 MHz (green) and 1.4 GHz (dark blue). (a) Variations in DMX. (b) Residual arrival times for all TOAs. Points are semitransparent; dark regions arise from the overlap of many points. (c), (d) Average residual arrival times shown full scale (panel c) and close-up of low residuals (panel d).

J1640 + 2224

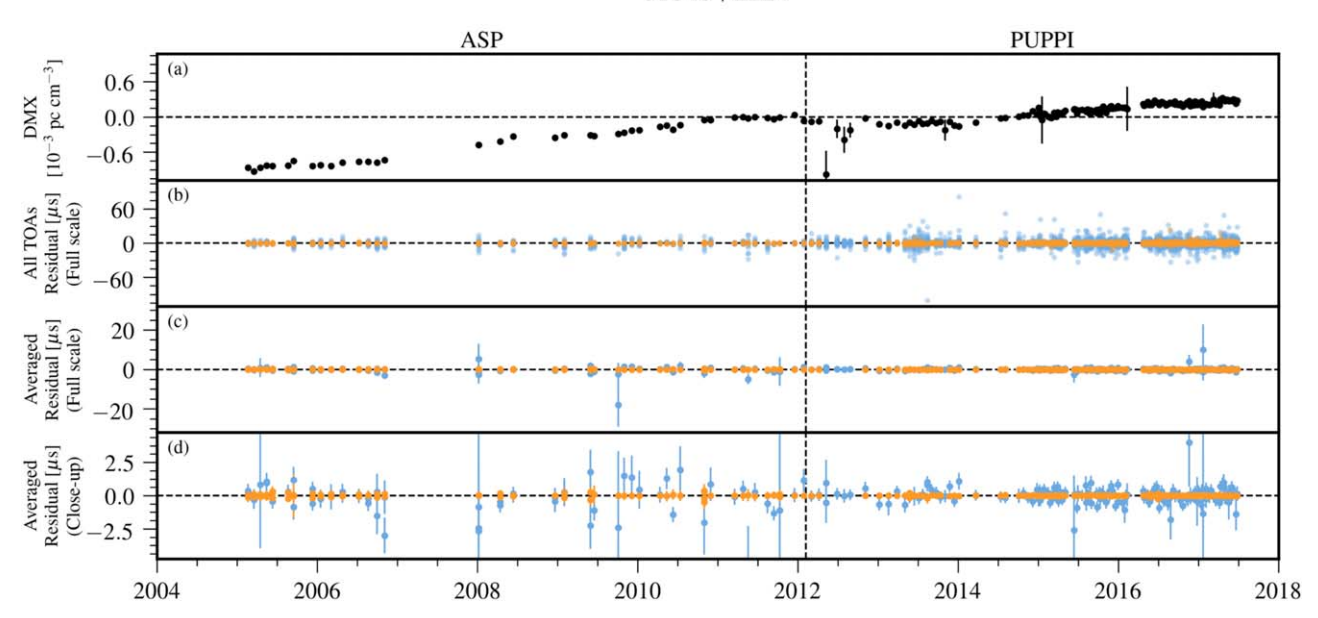


Figure 21. Timing residuals and DM variations for PSR J1640+2224. See the Appendix text for details. In residual plots, colored points indicate the receiver of each observation: 430 MHz (orange) and 1.4 GHz (light blue). (a) Variations in DMX. (b) Residual arrival times for all TOAs. Points are semitransparent; dark regions arise from the overlap of many points. (c), (d) Average residual arrival times shown full scale (panel c) and close-up of low residuals (panel d).

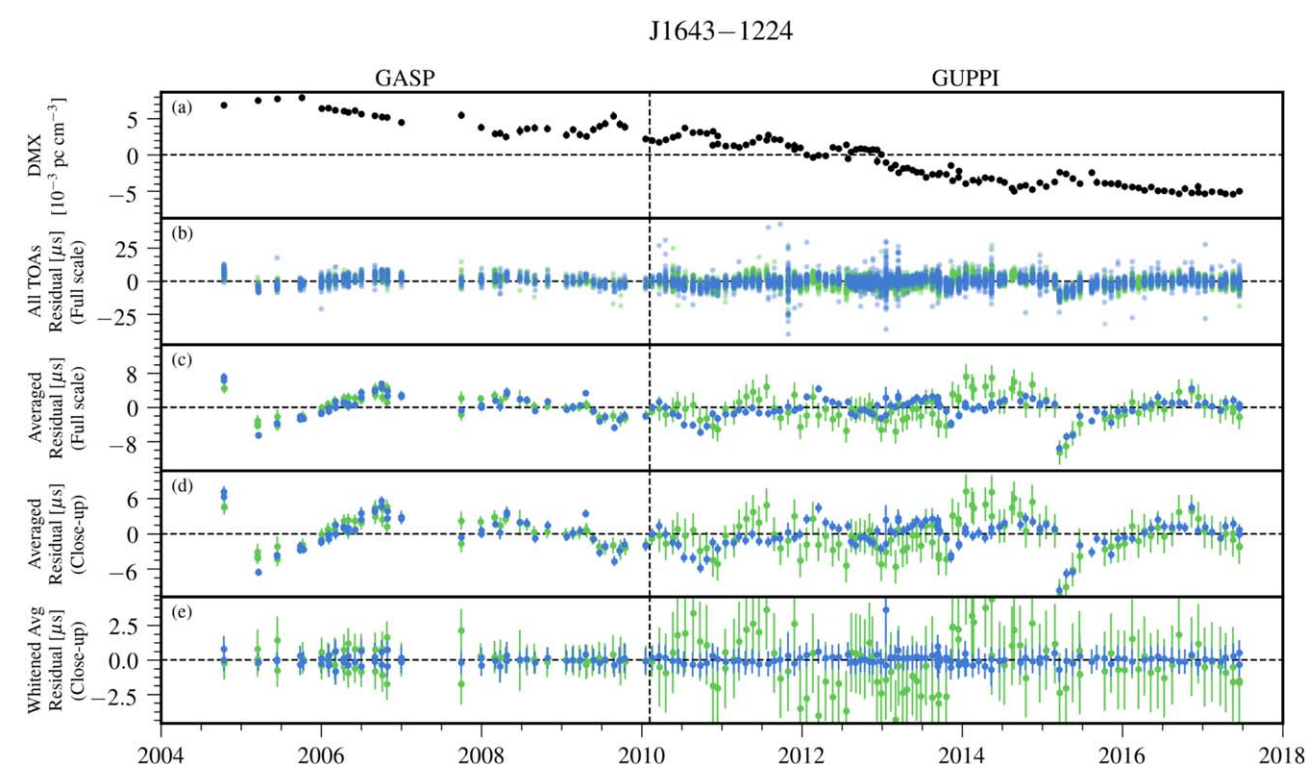


Figure 22. Timing residuals and DM variations for PSR J1643–1224. See the Appendix text for details. In residual plots, colored points indicate the receiver of each observation: 820 MHz (green) and 1.4 GHz (dark blue). (a) Variations in DMX. (b) Residual arrival times for all TOAs. Points are semitransparent; dark regions arise from the overlap of many points. (c), (d) Average residual arrival times shown full scale (panel c) and close-up of low residuals (panel d). (e) Whitened average residual arrival times after removing the red-noise model (close-up of low residuals).

J1713 + 0747

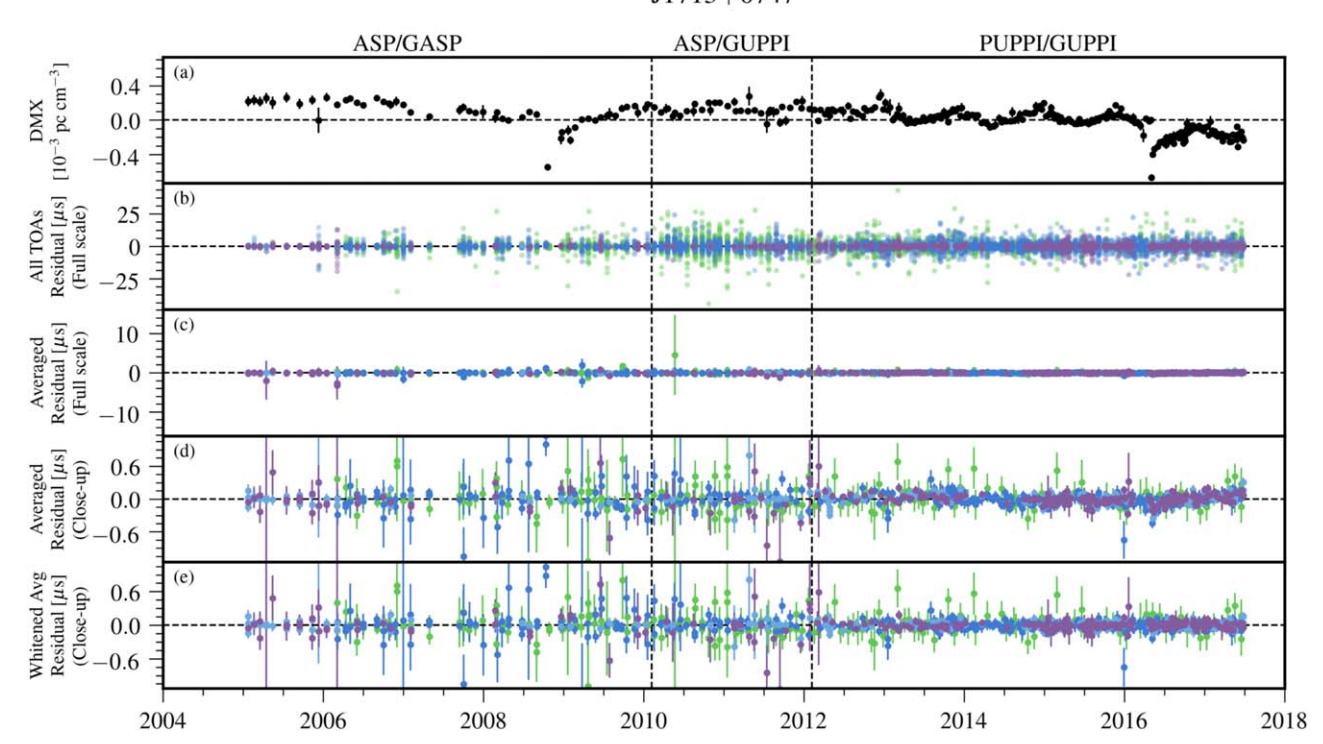


Figure 23. Timing residuals and DM variations for PSR J1713+0747. See the Appendix text for details. In residual plots, colored points indicate the receiver of each observation: 820 MHz (Green), 1.4 GHz (dark blue), 1.4 GHz (light blue), and 2.1 GHz (Purple). (a) Variations in DMX. (b) Residual arrival times for all TOAs. Points are semitransparent; dark regions arise from the overlap of many points. (c), (d) Average residual arrival times shown full scale (panel c) and close-up of low residuals (panel d). (e) Whitened average residual arrival times after removing the red-noise model (close-up of low residuals).

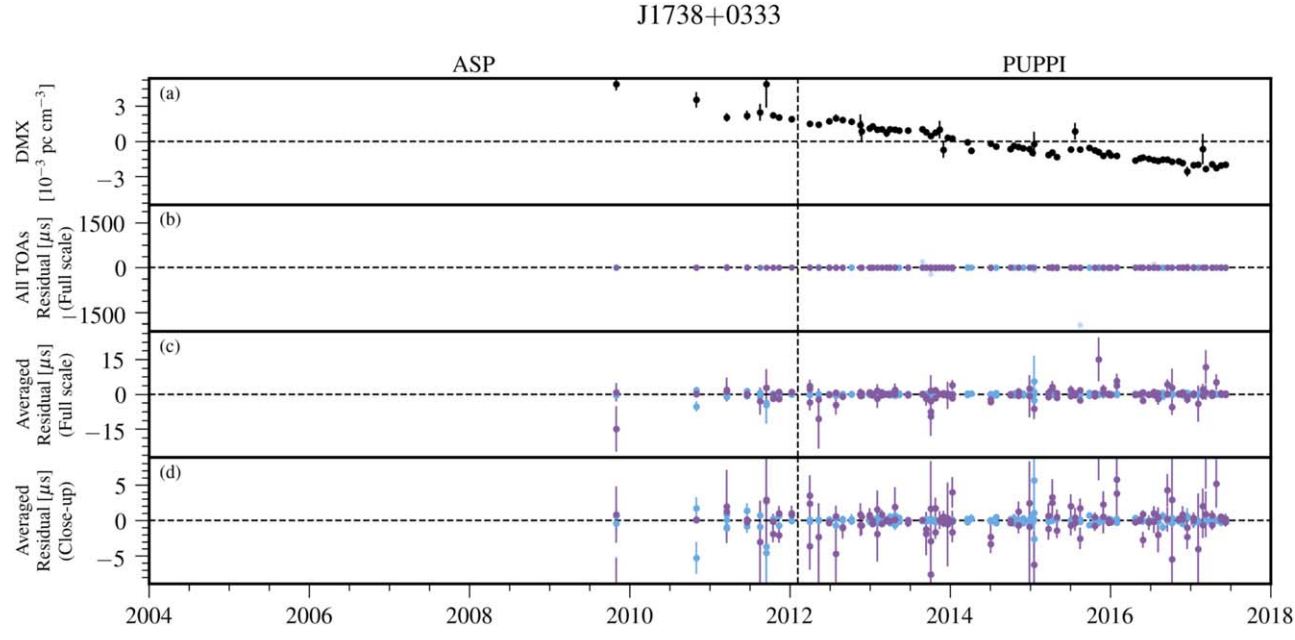


Figure 24. Timing residuals and DM variations for PSR J1738+0333. See the Appendix text for details. In residual plots, colored points indicate the receiver of each observation: 1.4 GHz (light blue) and 2.1 GHz (Purple). (a) Variations in DMX. (b) Residual arrival times for all TOAs. Points are semitransparent; dark regions arise from the overlap of many points. (c), (d) Average residual arrival times shown full scale (panel c) and close-up of low residuals (panel d).

J1741+1351

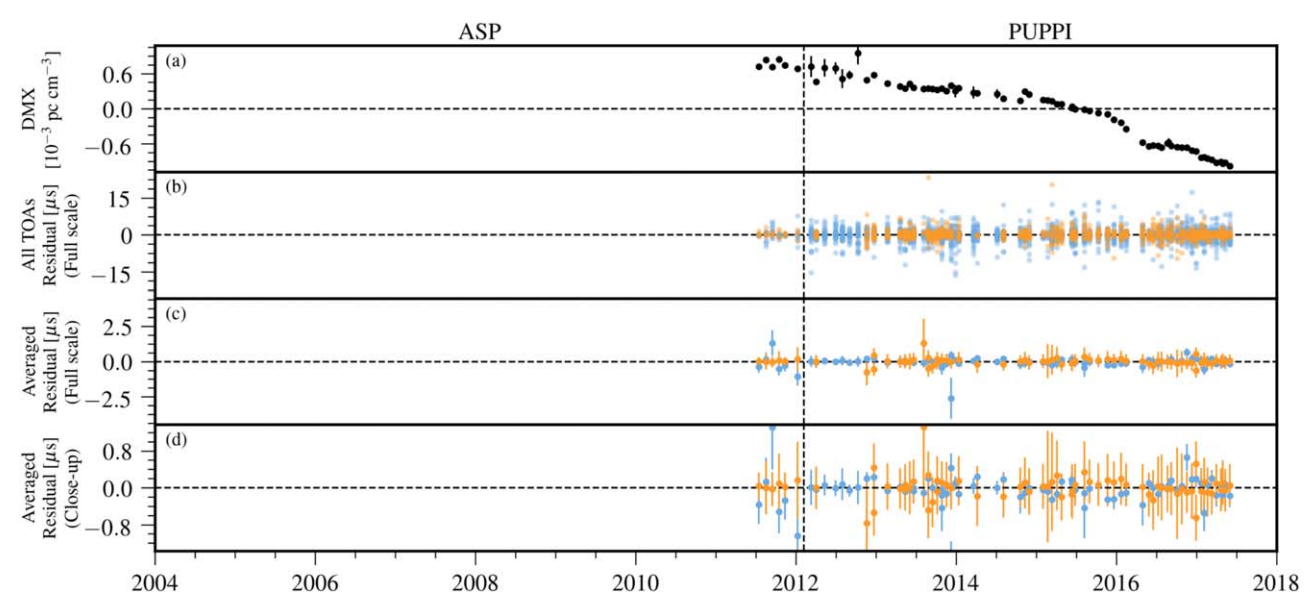


Figure 25. Timing residuals and DM variations for PSR J1741+1351. See the Appendix text for details. In residual plots, colored points indicate the receiver of each observation: 430 MHz (orange) and 1.4 GHz (light blue). (a) Variations in DMX. (b) Residual arrival times for all TOAs. Points are semitransparent; dark regions arise from the overlap of many points. (c), (d) Average residual arrival times shown full scale (panel c) and close-up of low residuals (panel d).

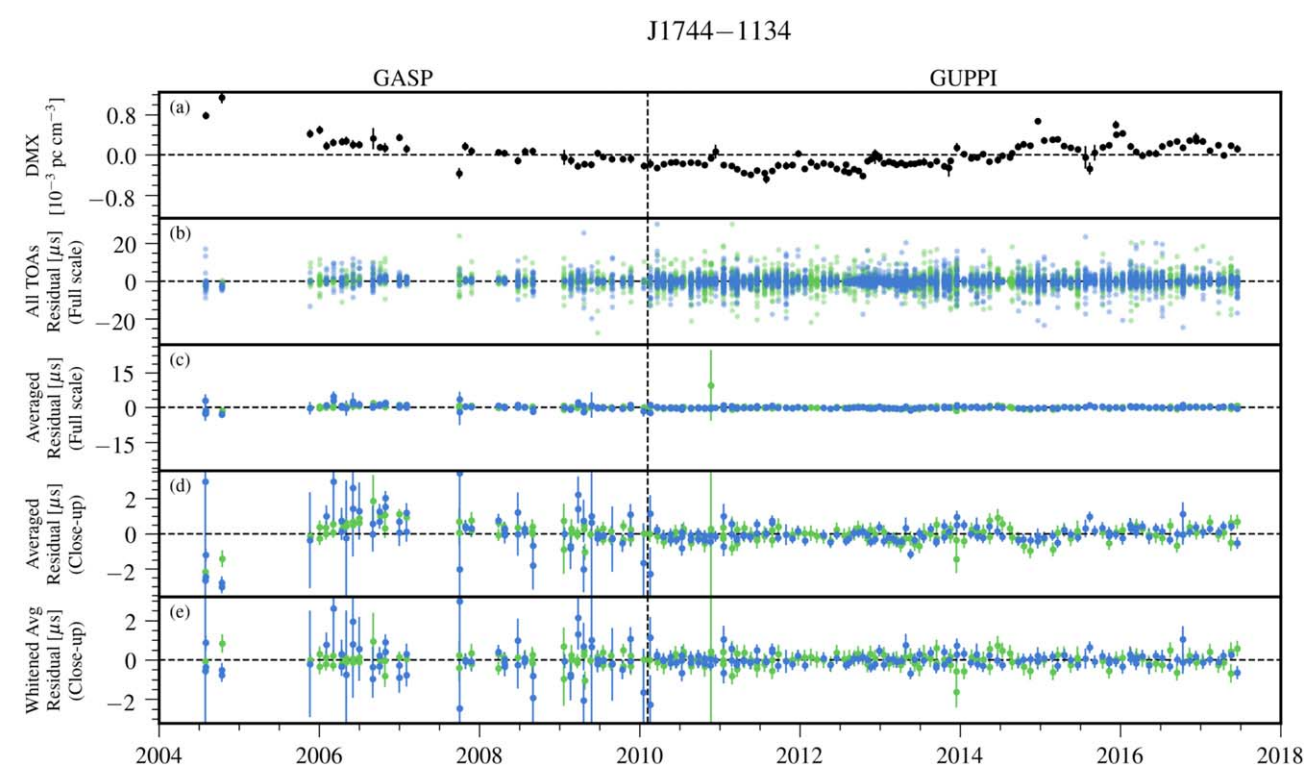


Figure 26. Timing residuals and DM variations for PSR J1744–1134. See the Appendix text for details. In residual plots, colored points indicate the receiver of each observation: 820 MHz (green) and 1.4 GHz (dark blue). (a) Variations in DMX. (b) Residual arrival times for all TOAs. Points are semitransparent; dark regions arise from the overlap of many points. (c), (d) Average residual arrival times shown full scale (panel c) and close-up of low residuals (panel d). (e) Whitened average residual arrival times after removing the red-noise model (close-up of low residuals).

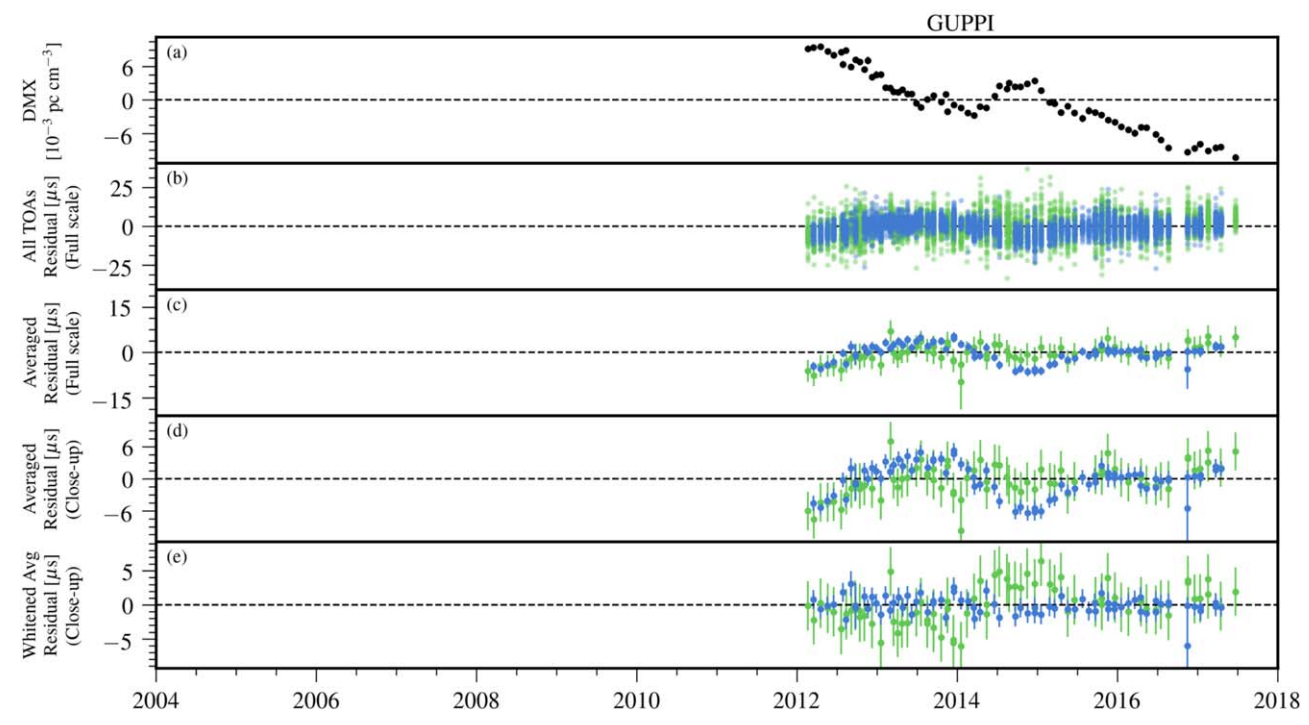


Figure 27. Timing residuals and DM variations for PSR J1747—4036. See the Appendix text for details. In residual plots, colored points indicate the receiver of each observation: 820 MHz (green) and 1.4 GHz (dark blue). (a) Variations in DMX. (b) Residual arrival times for all TOAs. Points are semitransparent; dark regions arise from the overlap of many points. (c), (d) Average residual arrival times shown full scale (panel c) and close-up of low residuals (panel d). (e) Whitened average residual arrival times after removing the red-noise model (close-up of low residuals).

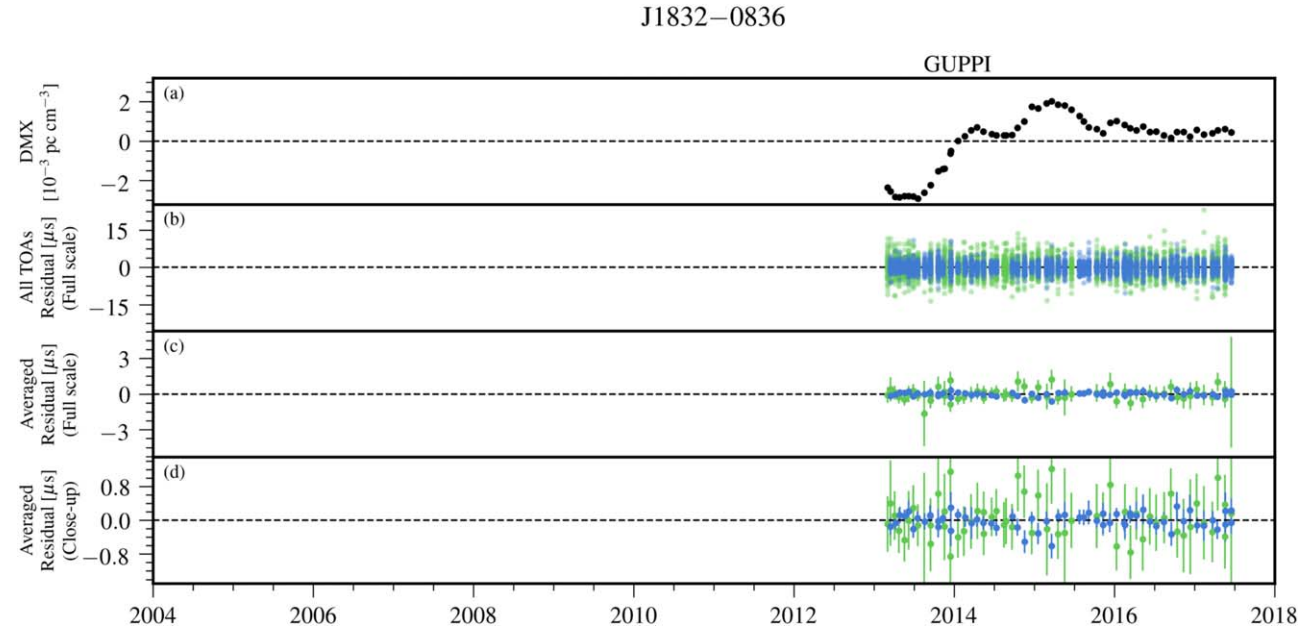


Figure 28. Timing residuals and DM variations for PSR J1832–0836. See the Appendix text for details. In residual plots, colored points indicate the receiver of each observation: 820 MHz (green) and 1.4 GHz (dark blue). (a) Variations in DMX. (b) Residual arrival times for all TOAs. Points are semitransparent; dark regions arise from the overlap of many points. (c), (d) Average residual arrival times shown full scale (panel c) and close-up of low residuals (panel d).

J1853+1303

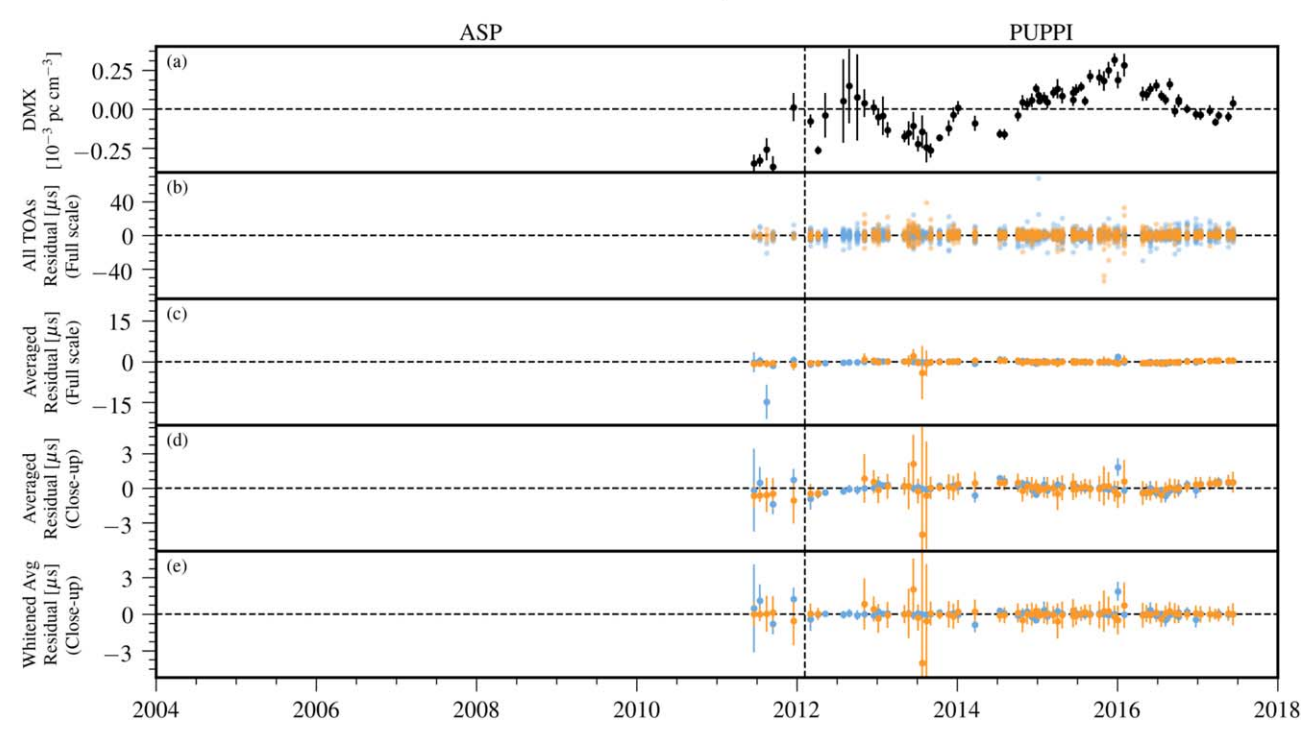


Figure 29. Timing residuals and DM variations for PSR J1853+1303. See the Appendix text for details. In residual plots, colored points indicate the receiver of each observation: 430 MHz (orange) and 1.4 GHz (light blue). (a) Variations in DMX. (b) Residual arrival times for all TOAs. Points are semitransparent; dark regions arise from the overlap of many points. (c), (d) Average residual arrival times shown full scale (panel c) and close-up of low residuals (panel d). (e) Whitened average residual arrival times after removing the red-noise model (close-up of low residuals).

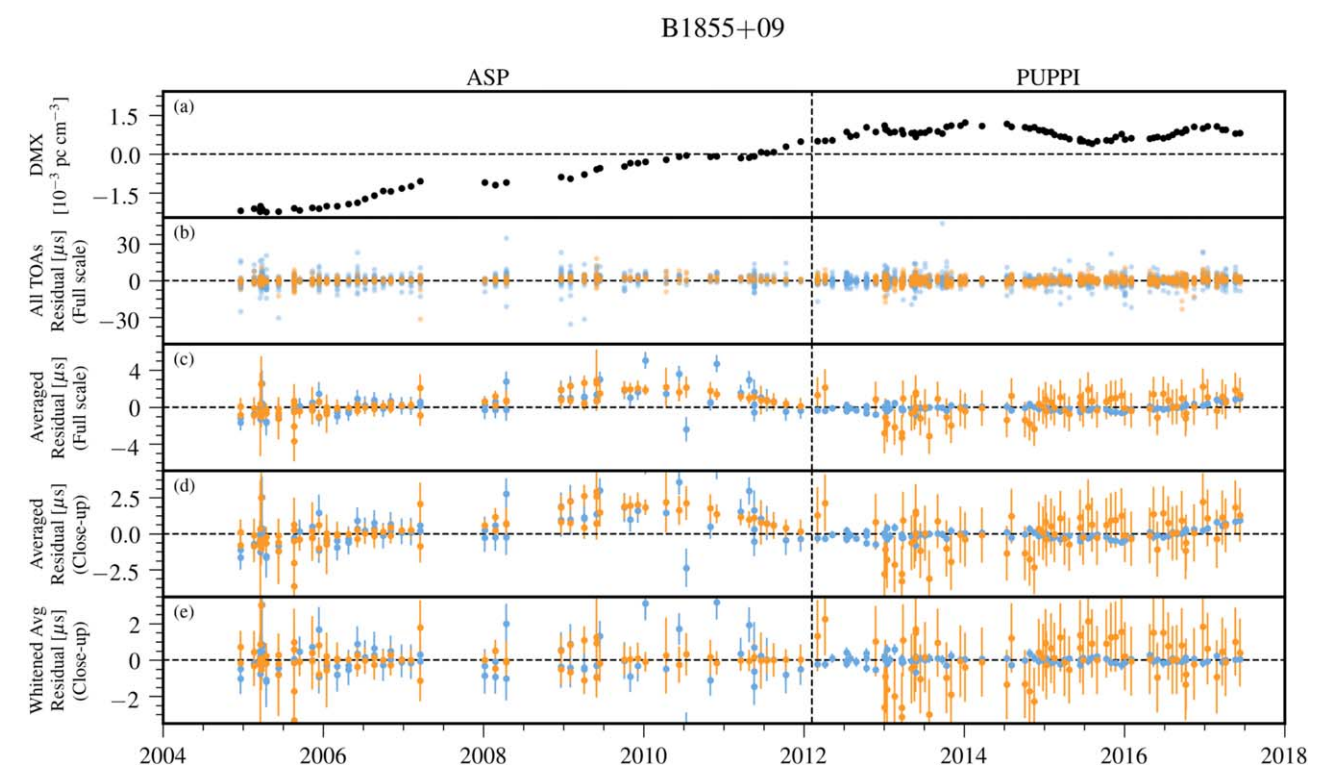


Figure 30. Timing residuals and DM variations for PSR B1855+09. See the Appendix text for details. In residual plots, colored points indicate the receiver of each observation: 430 MHz (orange) and 1.4 GHz (light blue). (a) Variations in DMX. (b) Residual arrival times for all TOAs. Points are semitransparent; dark regions arise from the overlap of many points. (c), (d) Average residual arrival times shown full scale (panel c) and close-up of low residuals (panel d). (e) Whitened average residual arrival times after removing the red-noise model (close-up of low residuals).

J1903+0327

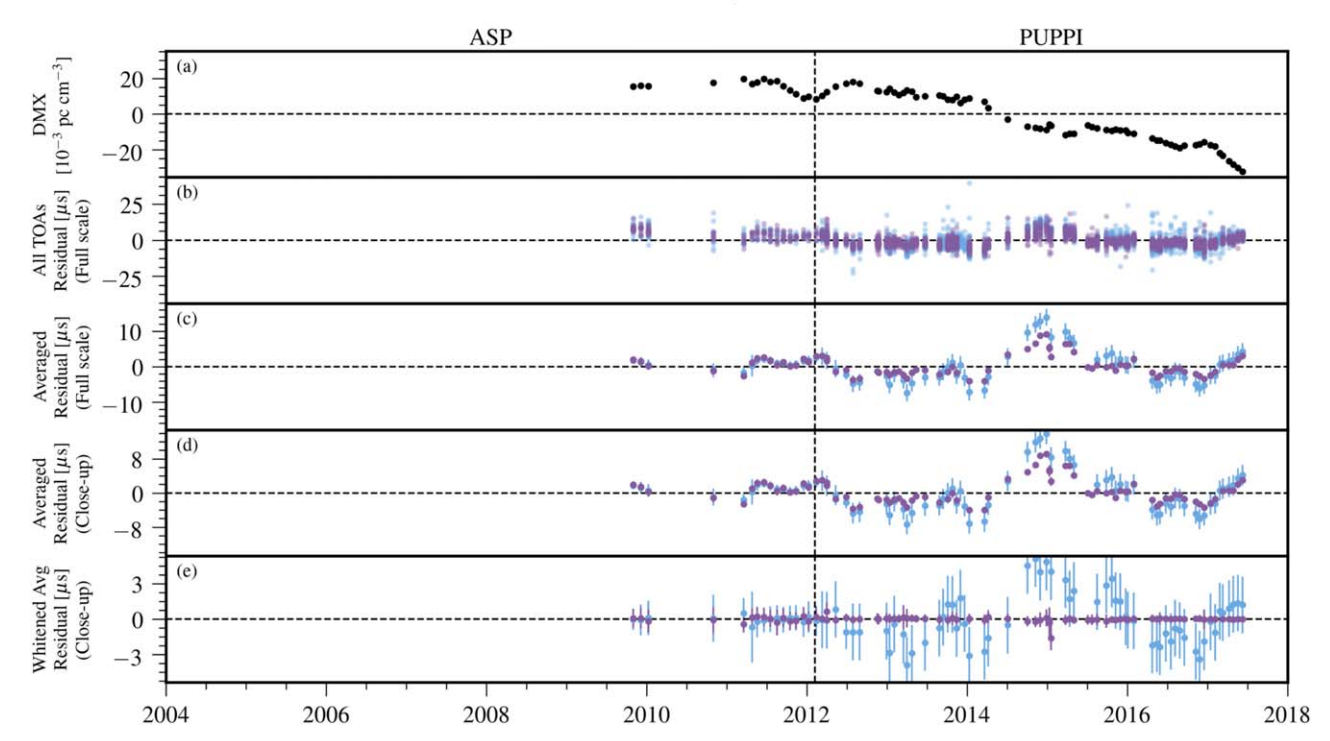


Figure 31. Timing residuals and DM variations for PSR J1903+0327. See the Appendix text for details. In residual plots, colored points indicate the receiver of each observation: 1.4 GHz (light blue) and 2.1 GHz (Purple). (a) Variations in DMX. (b) Residual arrival times for all TOAs. Points are semitransparent; dark regions arise from the overlap of many points. (c), (d) Average residual arrival times shown full scale (panel c) and close-up of low residuals (panel d). (e) Whitened average residual arrival times after removing the red-noise model (close-up of low residuals).

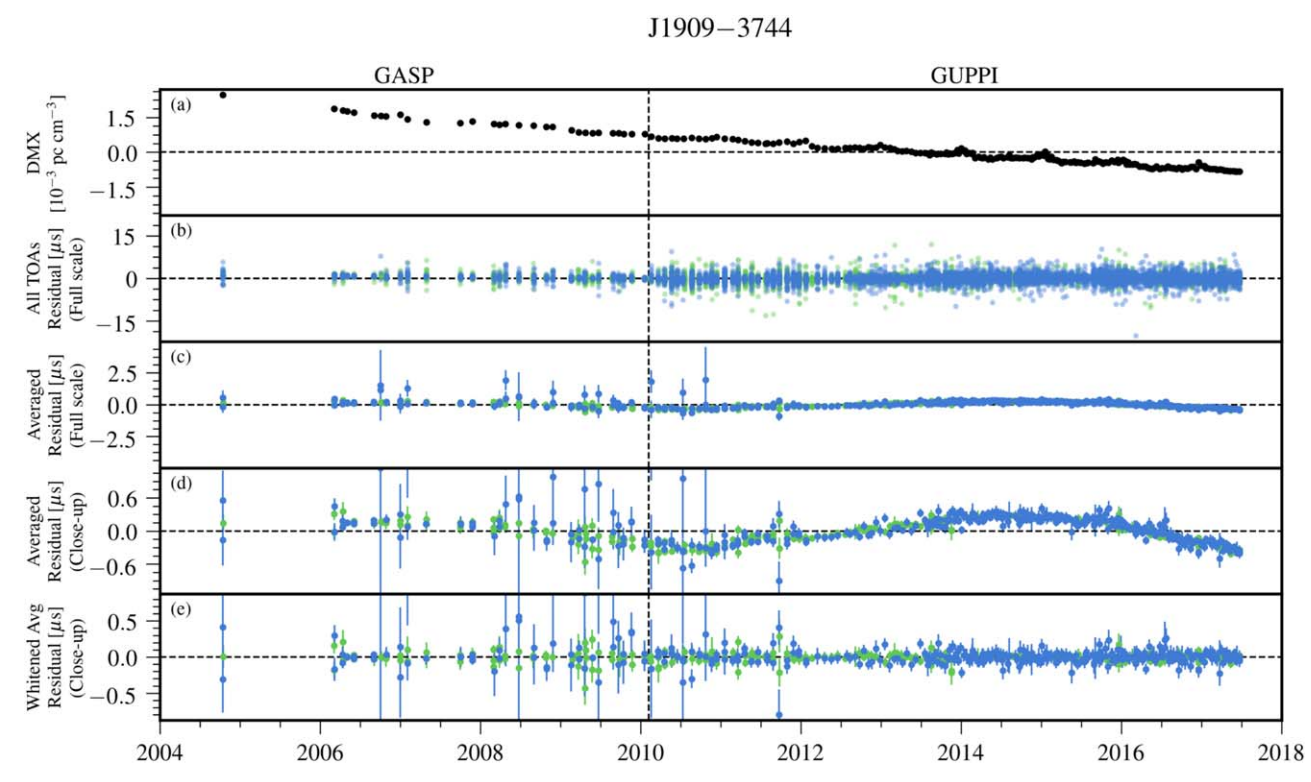


Figure 32. Timing residuals and DM variations for PSR J1909—3744. See the Appendix text for details. In residual plots, colored points indicate the receiver of each observation: 820 MHz (green) and 1.4 GHz (dark blue). (a) Variations in DMX. (b) Residual arrival times for all TOAs. Points are semitransparent; dark regions arise from the overlap of many points. (c), (d) Average residual arrival times shown full scale (panel c) and close-up of low residuals (panel d). (e) Whitened average residual arrival times after removing the red-noise model (close-up of low residuals).

J1910+1256

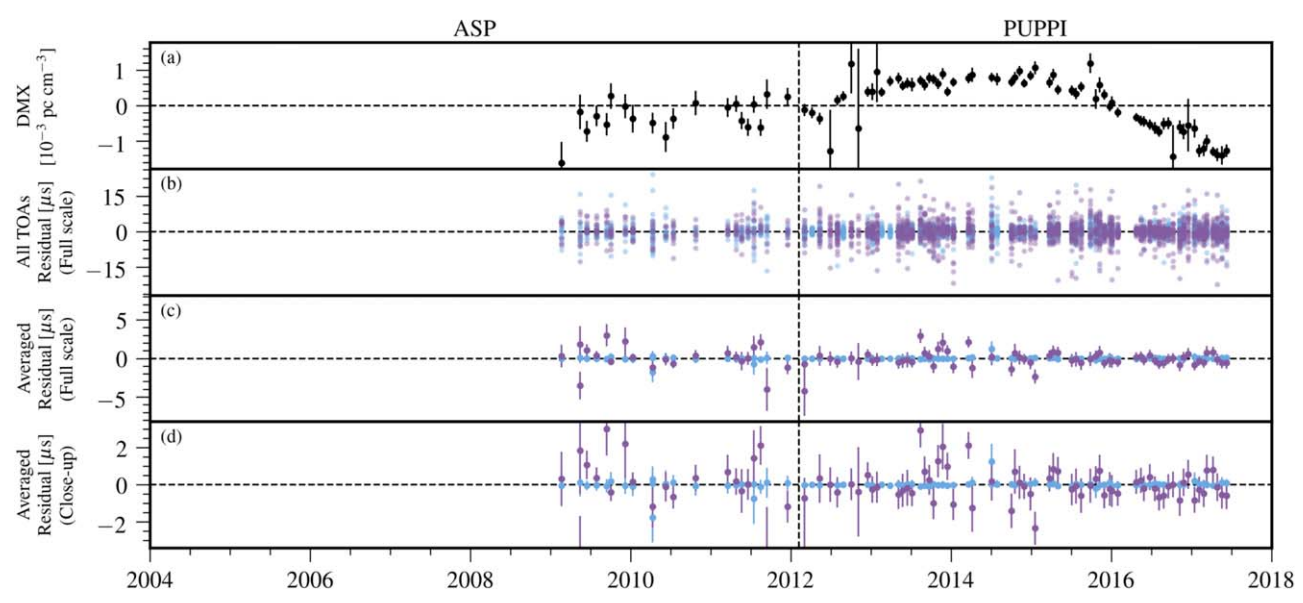


Figure 33. Timing residuals and DM variations for PSR J1910+1256. See the Appendix text for details. In residual plots, colored points indicate the receiver of each observation: 1.4 GHz (light blue) and 2.1 GHz (Purple). (a) Variations in DMX. (b) Residual arrival times for all TOAs. Points are semitransparent; dark regions arise from the overlap of many points. (c), (d) Average residual arrival times shown full scale (panel c) and close-up of low residuals (panel d).

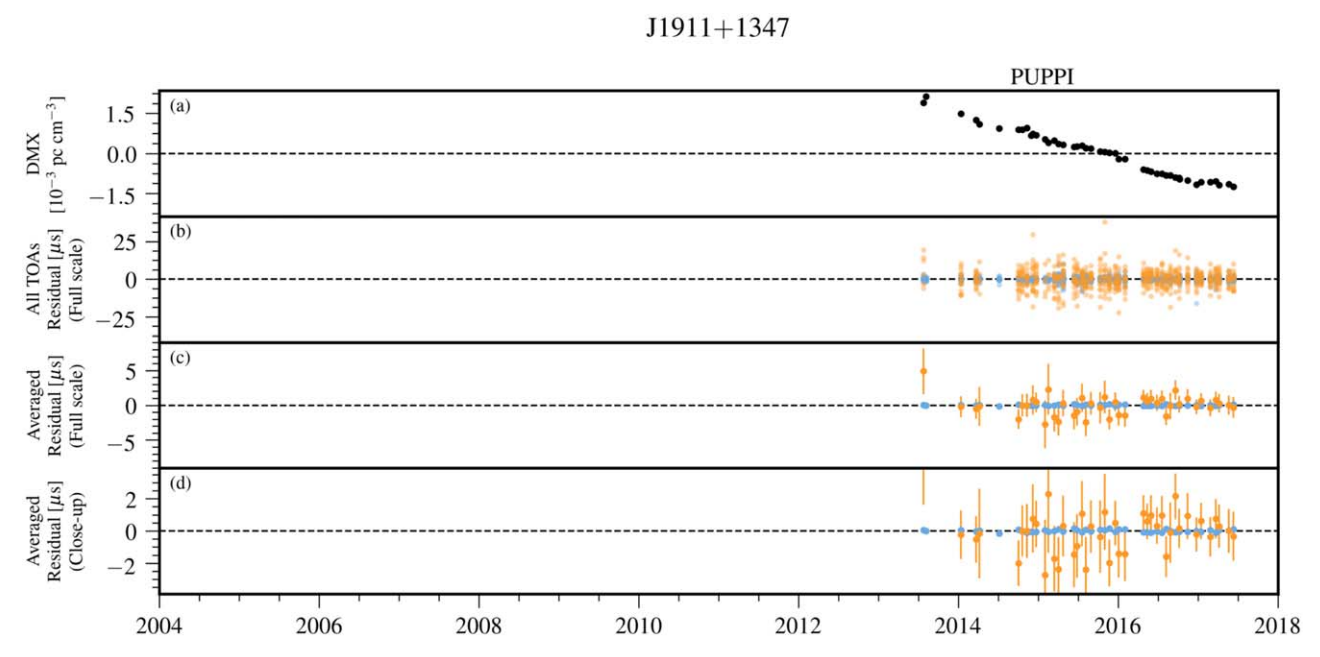


Figure 34. Timing residuals and DM variations for PSR J1911+1347. See the Appendix text for details. In residual plots, colored points indicate the receiver of each observation: 430 MHz (orange) and 1.4 GHz (light blue). (a) Variations in DMX. (b) Residual arrival times for all TOAs. Points are semitransparent; dark regions arise from the overlap of many points. (c), (d) Average residual arrival times shown full scale (panel c) and close-up of low residuals (panel d).

J1918-0642

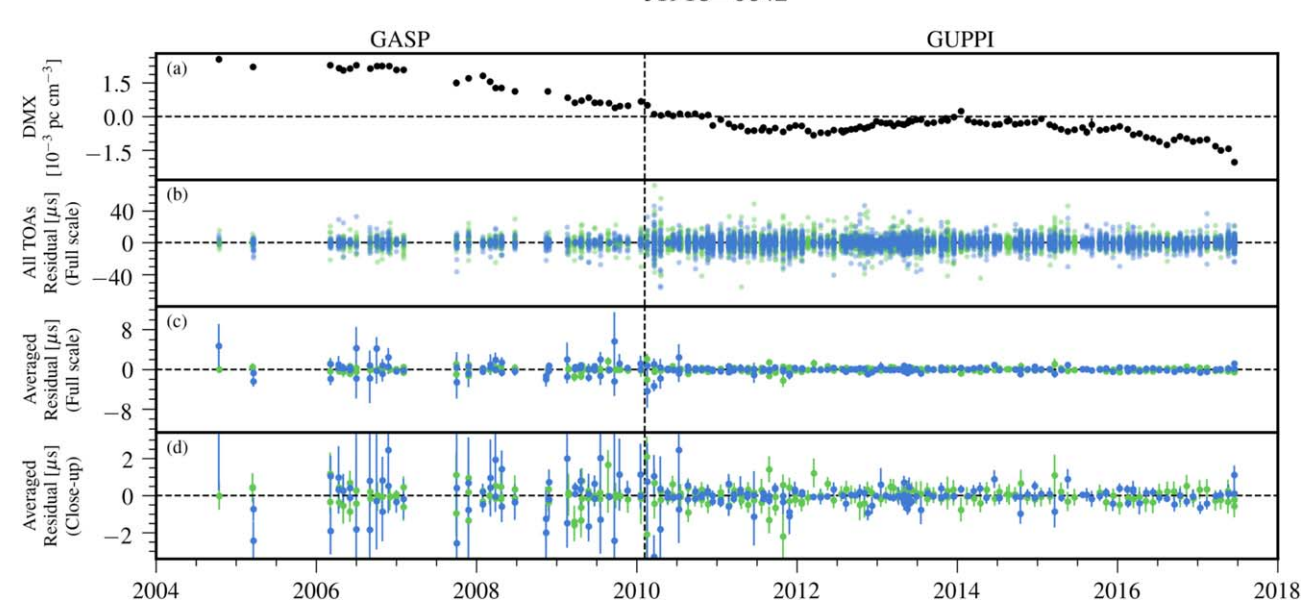


Figure 35. Timing residuals and DM variations for PSR J1918–0642. See the Appendix text for details. In residual plots, colored points indicate the receiver of each observation: 820 MHz (green) and 1.4 GHz (dark blue). (a) Variations in DMX. (b) Residual arrival times for all TOAs. Points are semitransparent; dark regions arise from the overlap of many points. (c), (d) Average residual arrival times shown full scale (panel c) and close-up of low residuals (panel d).

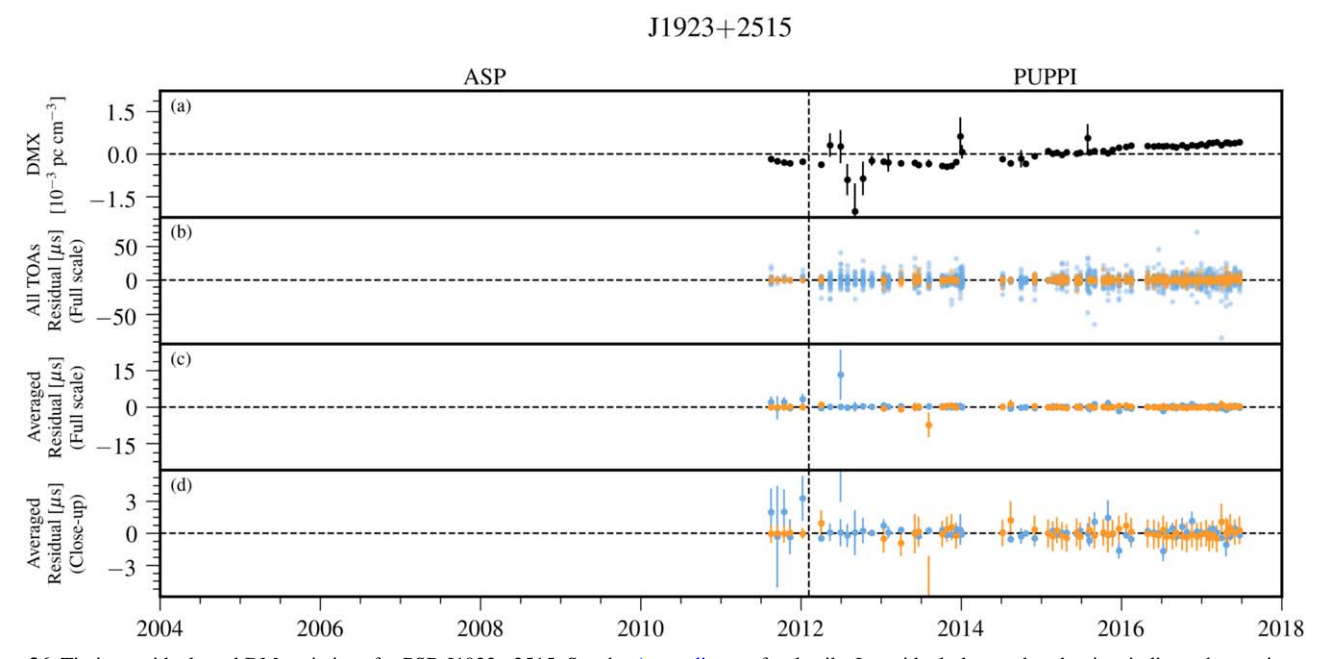


Figure 36. Timing residuals and DM variations for PSR J1923+2515. See the Appendix text for details. In residual plots, colored points indicate the receiver of each observation: 430 MHz (orange) and 1.4 GHz (light blue). (a) Variations in DMX. (b) Residual arrival times for all TOAs. Points are semitransparent; dark regions arise from the overlap of many points. (c), (d) Average residual arrival times shown full scale (panel c) and close-up of low residuals (panel d).



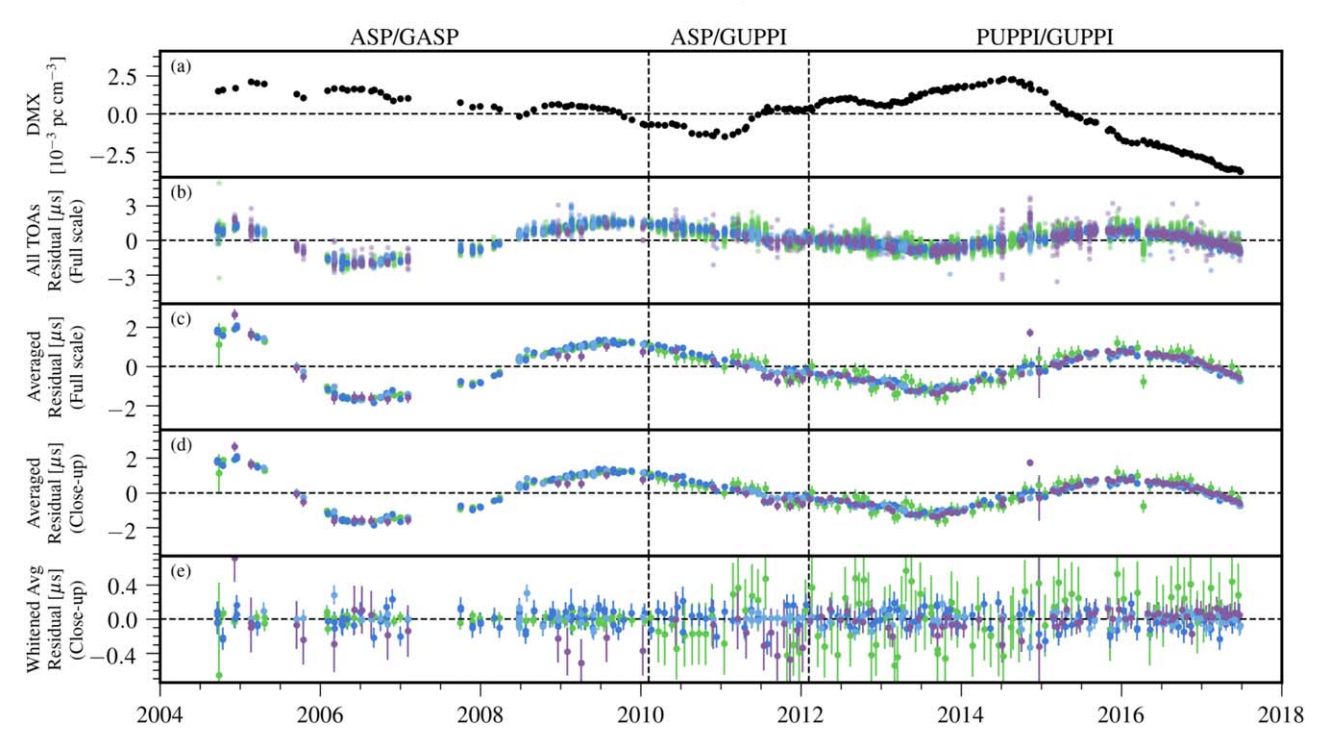


Figure 37. Timing residuals and DM variations for PSR B1937+21. See the Appendix text for details. In residual plots, colored points indicate the receiver of each observation: 820 MHz (Green), 1.4 GHz (dark blue), 1.4 GHz (light blue), and 2.1 GHz (Purple). (a) Variations in DMX. (b) Residual arrival times for all TOAs. Points are semitransparent; dark regions arise from the overlap of many points. (c), (d) Average residual arrival times shown full scale (panel c) and close-up of low residuals (panel d). (e) Whitened average residual arrival times after removing the red-noise model (close-up of low residuals).

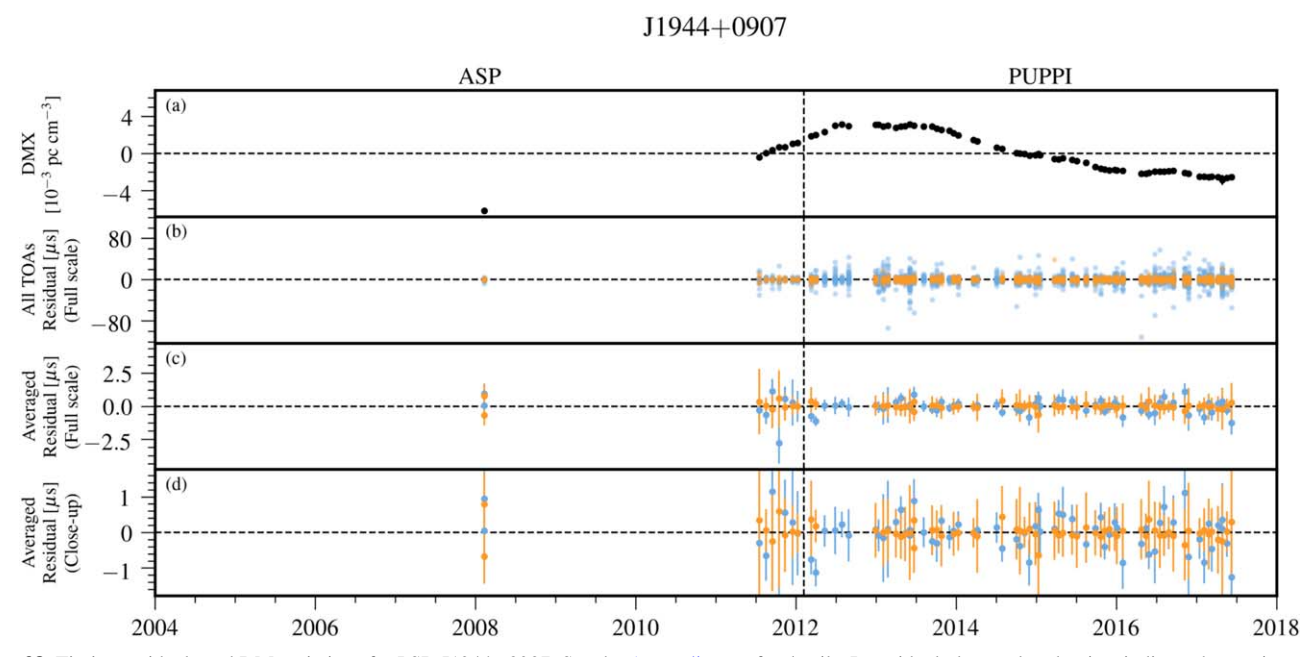


Figure 38. Timing residuals and DM variations for PSR J1944+0907. See the Appendix text for details. In residual plots, colored points indicate the receiver of each observation: 430 MHz (orange) and 1.4 GHz (light blue). (a) Variations in DMX. (b) Residual arrival times for all TOAs. Points are semitransparent; dark regions arise from the overlap of many points. (c), (d) Average residual arrival times shown full scale (panel c) and close-up of low residuals (panel d).

J1946+3417

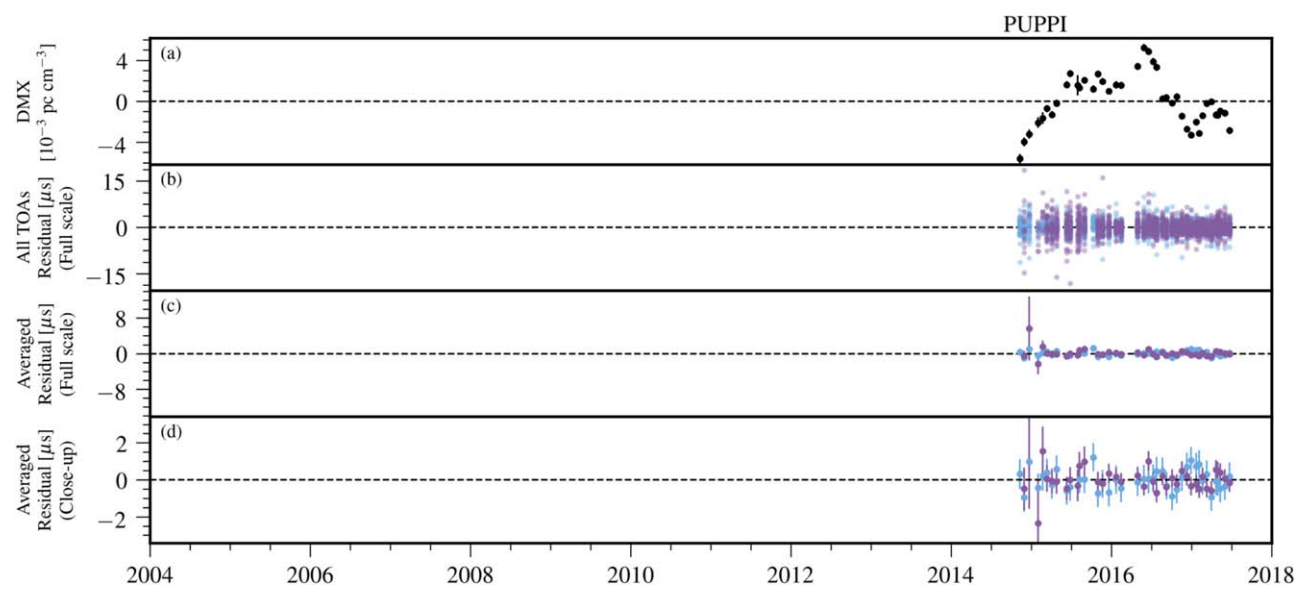


Figure 39. Timing residuals and DM variations for PSR J1946+3417. See the Appendix text for details. In residual plots, colored points indicate the receiver of each observation: 1.4 GHz (light blue) and 2.1 GHz (Purple). (a) Variations in DMX. (b) Residual arrival times for all TOAs. Points are semitransparent; dark regions arise from the overlap of many points. (c), (d) Average residual arrival times shown full scale (panel c) and close-up of low residuals (panel d).

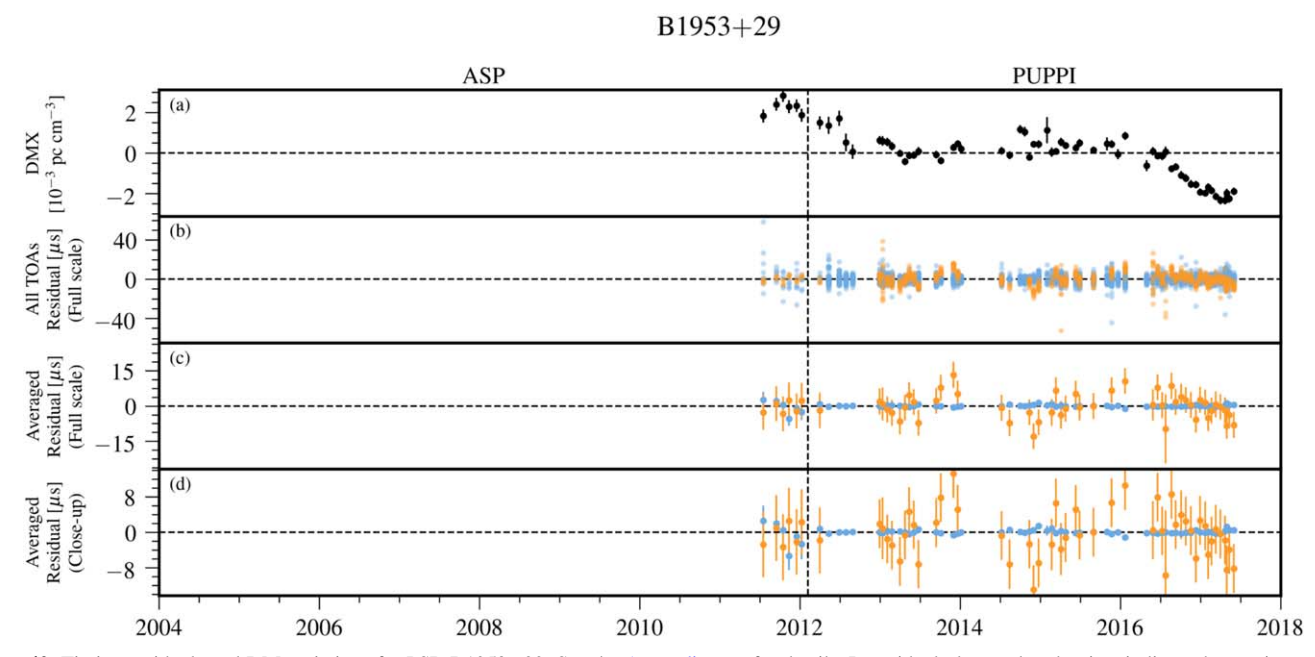


Figure 40. Timing residuals and DM variations for PSR B1953+29. See the Appendix text for details. In residual plots, colored points indicate the receiver of each observation: 430 MHz (orange) and 1.4 GHz (light blue). (a) Variations in DMX. (b) Residual arrival times for all TOAs. Points are semitransparent; dark regions arise from the overlap of many points. (c), (d) Average residual arrival times shown full scale (panel c) and close-up of low residuals (panel d).



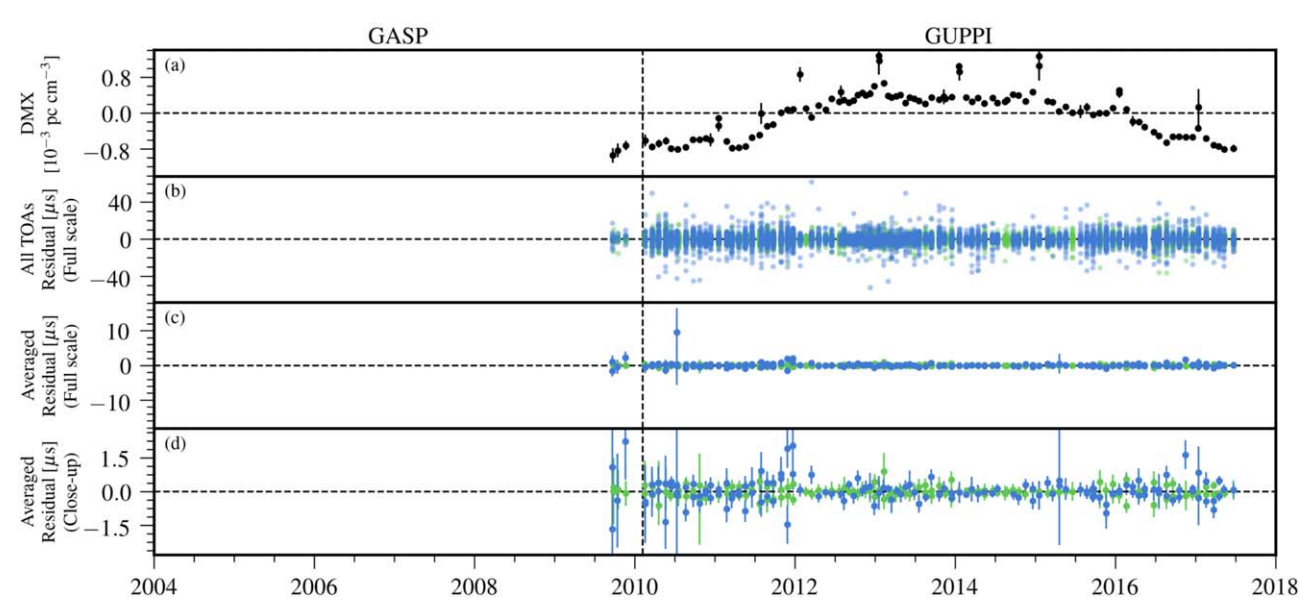


Figure 41. Timing residuals and DM variations for PSR J2010-1323. See the Appendix text for details. In residual plots, colored points indicate the receiver of each observation: 820 MHz (green) and 1.4 GHz (dark blue). (a) Variations in DMX. (b) Residual arrival times for all TOAs. Points are semitransparent; dark regions arise from the overlap of many points. (c), (d) Average residual arrival times shown full scale (panel c) and close-up of low residuals (panel d).

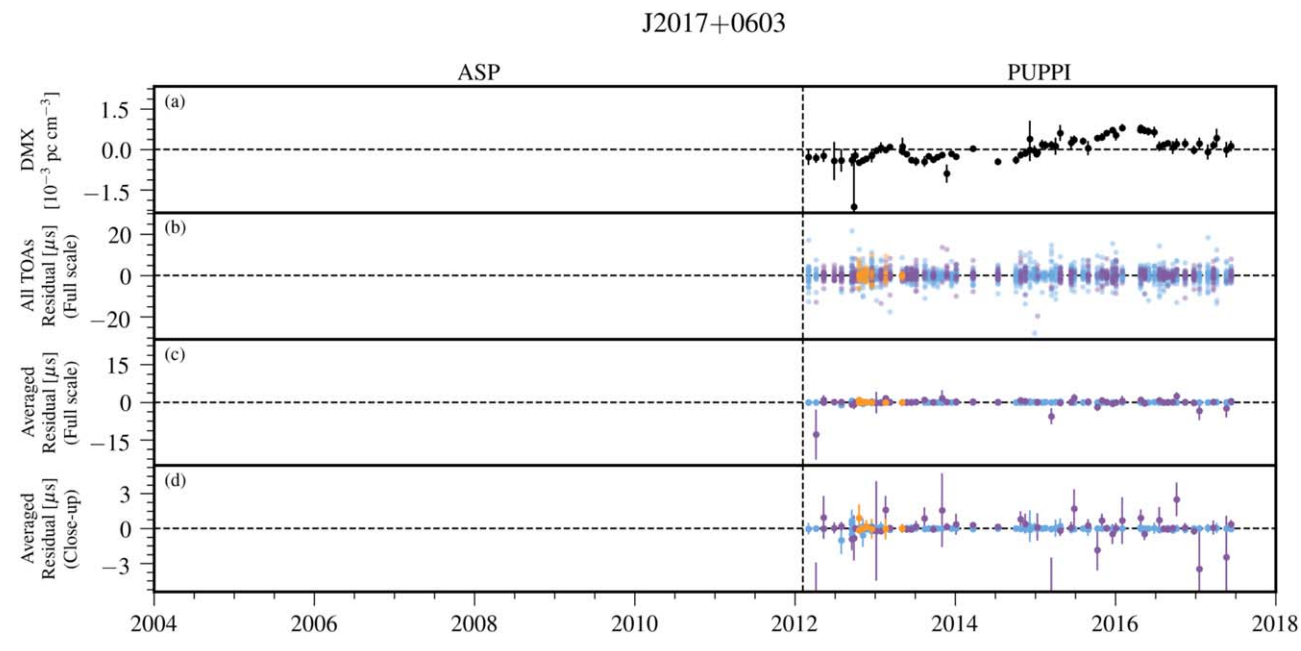


Figure 42. Timing residuals and DM variations for PSR J2017+0603. See the Appendix text for details. In residual plots, colored points indicate the receiver of each observation: 430 MHz (orange), 1.4 GHz (light blue), and 2.1 GHz (Purple). (a) Variations in DMX. (b) Residual arrival times for all TOAs. Points are semitransparent; dark regions arise from the overlap of many points. (c), (d) Average residual arrival times shown full scale (panel c) and close-up of low residuals (panel d).

J2033+1734

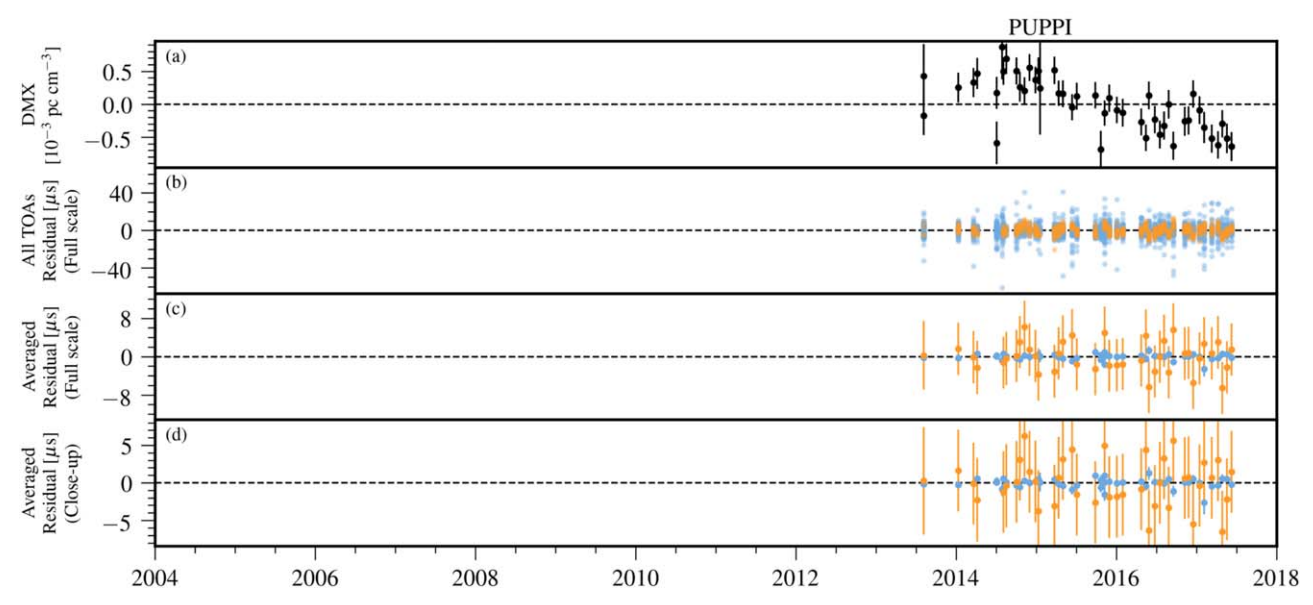


Figure 43. Timing residuals and DM variations for PSR J2033+1734. See the Appendix text for details. In residual plots, colored points indicate the receiver of each observation: 430 MHz (orange) and 1.4 GHz (light blue). (a) Variations in DMX. (b) Residual arrival times for all TOAs. Points are semitransparent; dark regions arise from the overlap of many points. (c), (d) Average residual arrival times shown full scale (panel c) and close-up of low residuals (panel d).

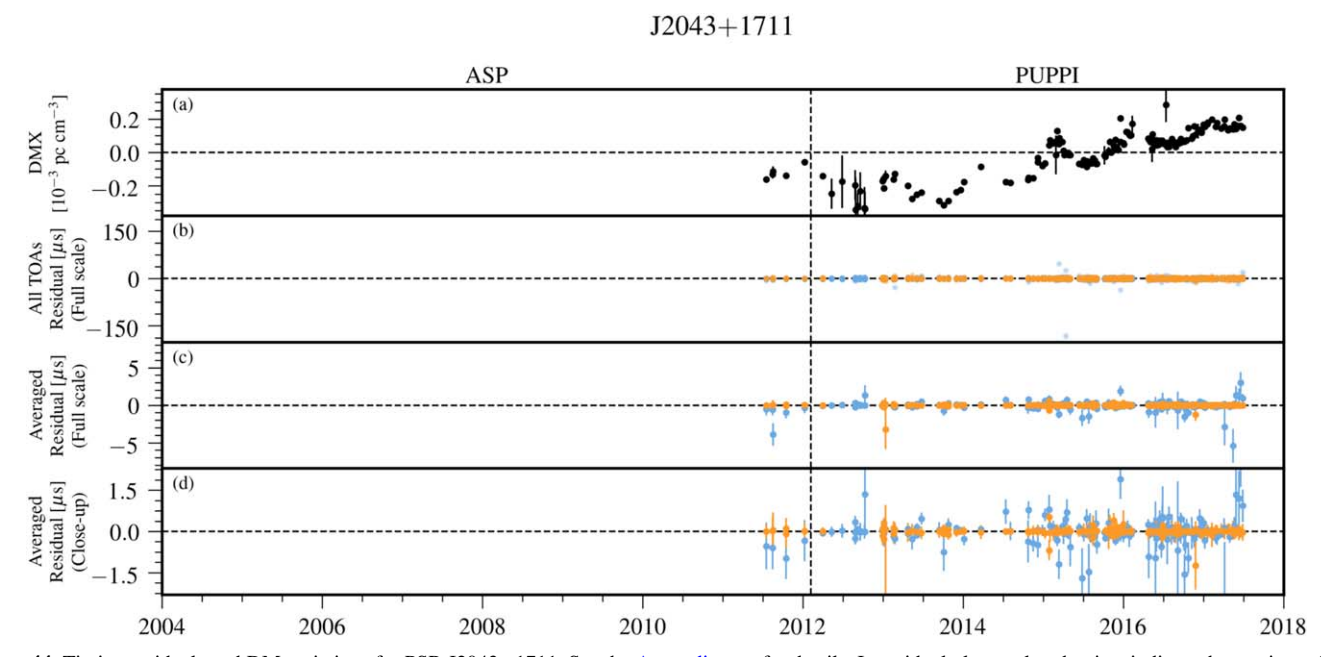


Figure 44. Timing residuals and DM variations for PSR J2043+1711. See the Appendix text for details. In residual plots, colored points indicate the receiver of each observation: 430 MHz (orange) and 1.4 GHz (light blue). (a) Variations in DMX. (b) Residual arrival times for all TOAs. Points are semitransparent; dark regions arise from the overlap of many points. (c), (d) Average residual arrival times shown full scale (panel c) and close-up of low residuals (panel d).

J2145-0750

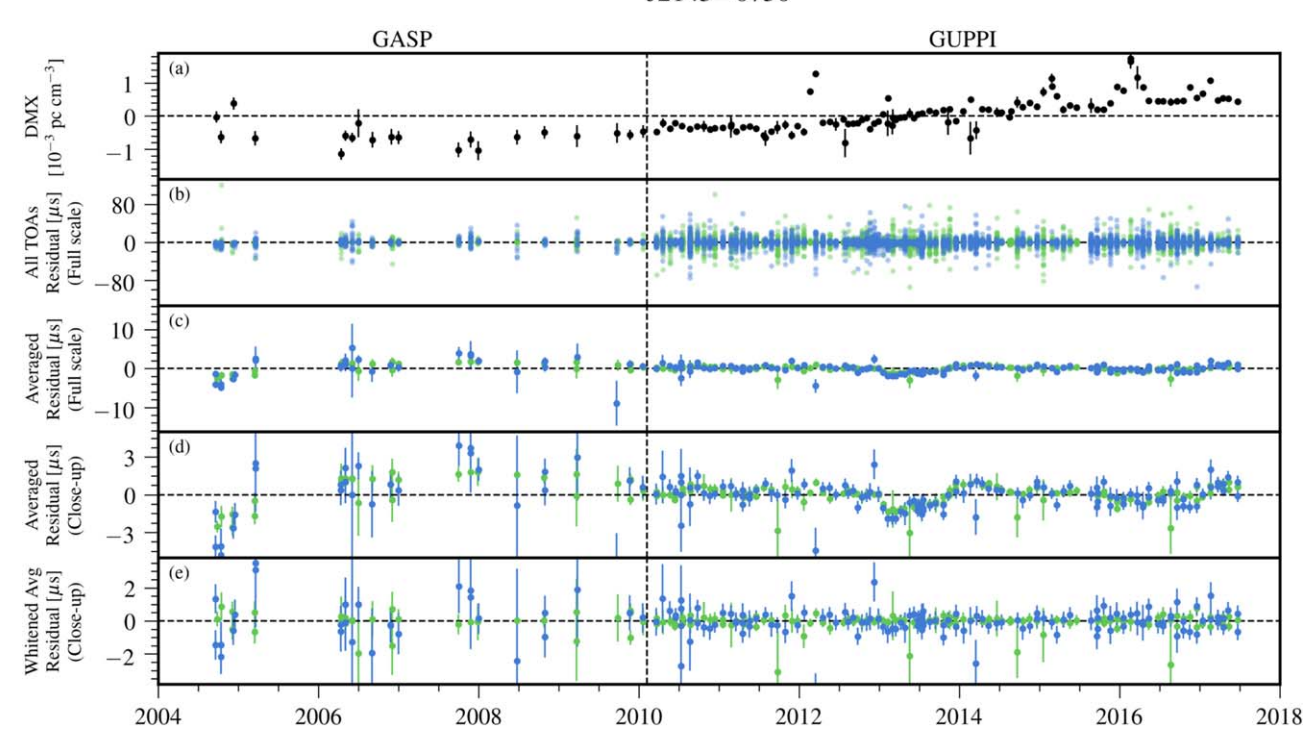


Figure 45. Timing residuals and DM variations for PSR J2145-0750. See the Appendix text for details. In residual plots, colored points indicate the receiver of each observation: 820 MHz (green) and 1.4 GHz (dark blue). (a) Variations in DMX. (b) Residual arrival times for all TOAs. Points are semitransparent; dark regions arise from the overlap of many points. (c), (d) Average residual arrival times shown full scale (panel c) and close-up of low residuals (panel d). (e) Whitened average residual arrival times after removing the red-noise model (close-up of low residuals).

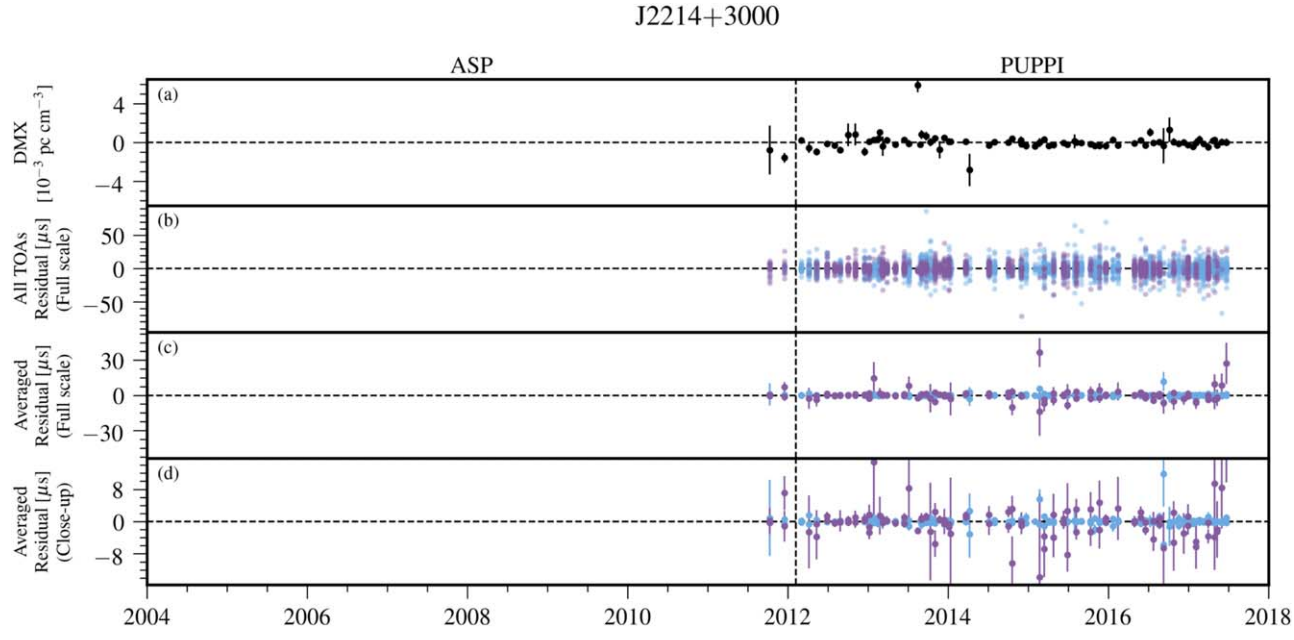


Figure 46. Timing residuals and DM variations for PSR J2214+3000. See the Appendix text for details. In residual plots, colored points indicate the receiver of each observation: 1.4 GHz (light blue) and 2.1 GHz (Purple). (a) Variations in DMX. (b) Residual arrival times for all TOAs. Points are semitransparent; dark regions arise from the overlap of many points. (c), (d) Average residual arrival times shown full scale (panel c) and close-up of low residuals (panel d).

J2229+2643

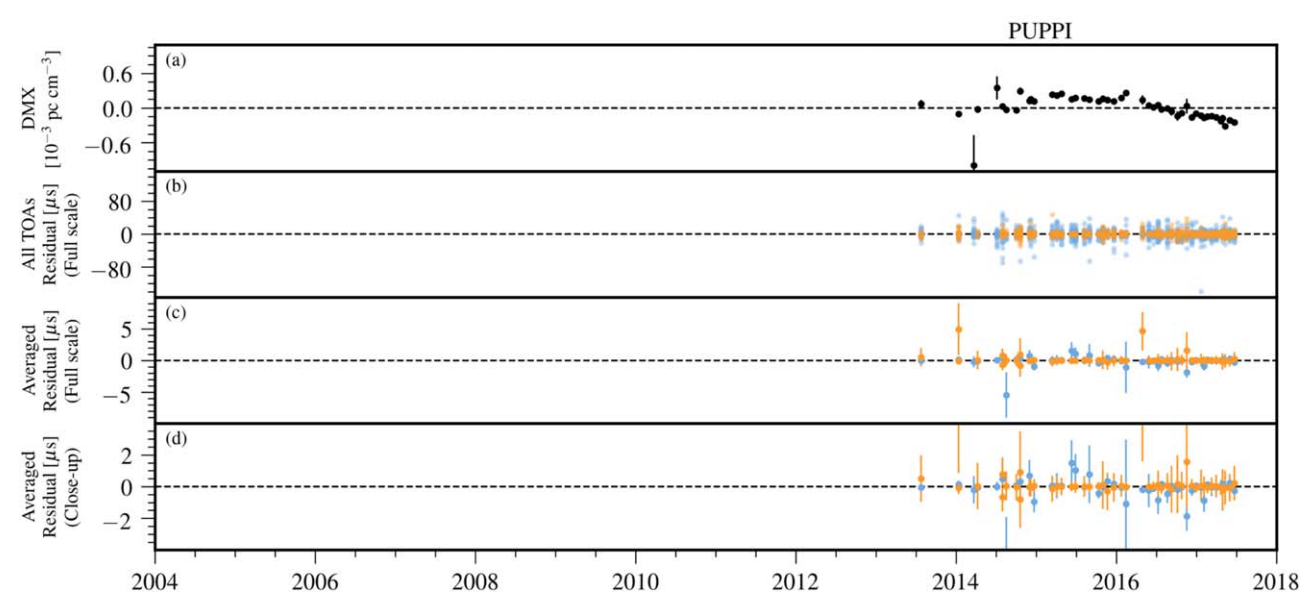


Figure 47. Timing residuals and DM variations for PSR J2229+2643. See the Appendix text for details. In residual plots, colored points indicate the receiver of each observation: 430 MHz (orange) and 1.4 GHz (light blue). (a) Variations in DMX. (b) Residual arrival times for all TOAs. Points are semitransparent; dark regions arise from the overlap of many points. (c), (d) Average residual arrival times shown full scale (panel c) and close-up of low residuals (panel d).



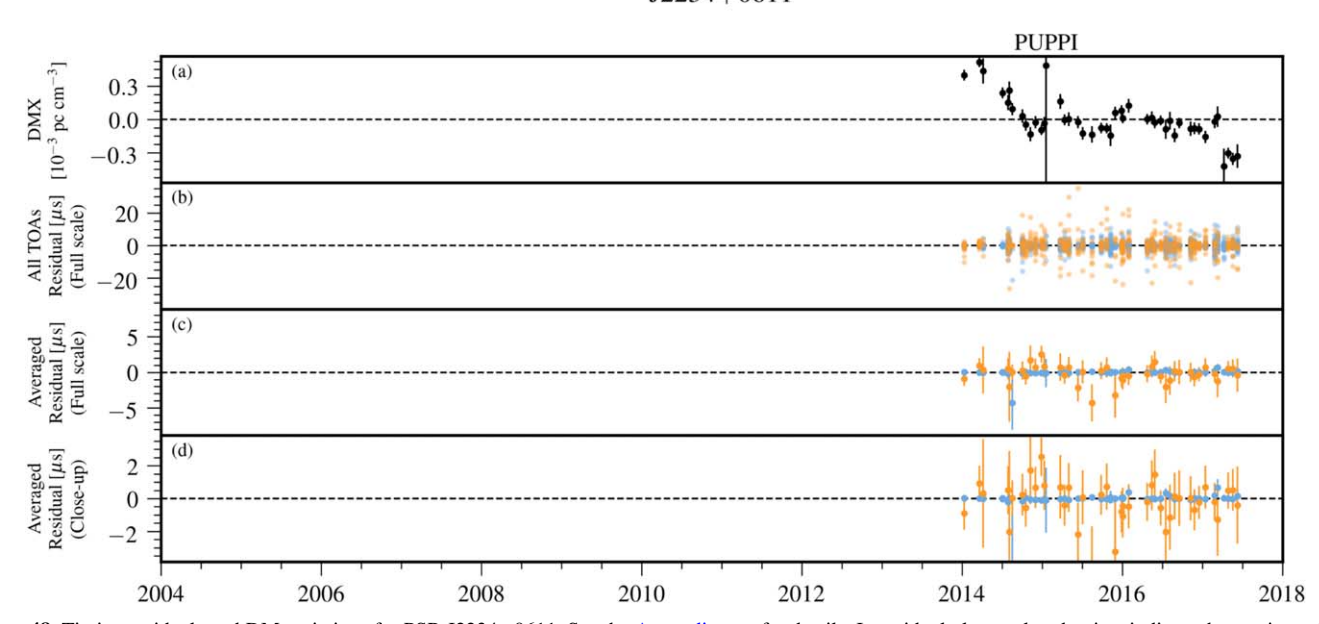


Figure 48. Timing residuals and DM variations for PSR J2234+0611. See the Appendix text for details. In residual plots, colored points indicate the receiver of each observation: 430 MHz (orange) and 1.4 GHz (light blue). (a) Variations in DMX. (b) Residual arrival times for all TOAs. Points are semitransparent; dark regions arise from the overlap of many points. (c), (d) Average residual arrival times shown full scale (panel c) and close-up of low residuals (panel d).

J2234+0944

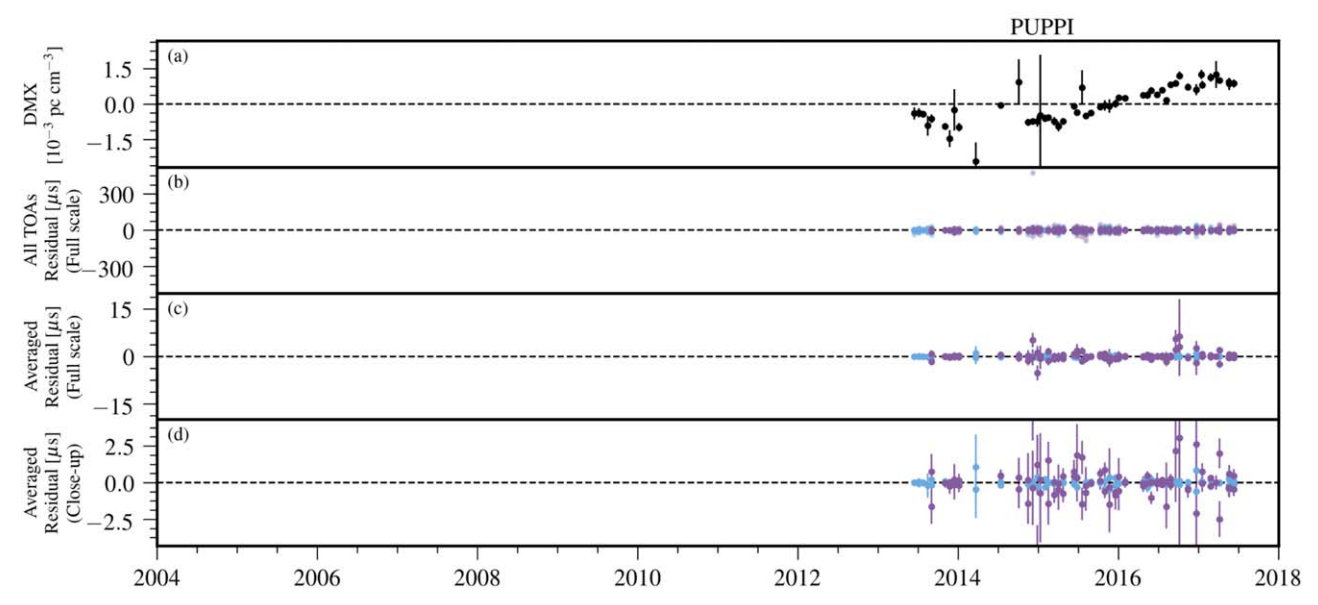


Figure 49. Timing residuals and DM variations for PSR J2234+0944. See the Appendix text for details. In residual plots, colored points indicate the receiver of each observation: 1.4 GHz (light blue) and 2.1 GHz (Purple). (a) Variations in DMX. (b) Residual arrival times for all TOAs. Points are semitransparent; dark regions arise from the overlap of many points. (c), (d) Average residual arrival times shown full scale (panel c) and close-up of low residuals (panel d).

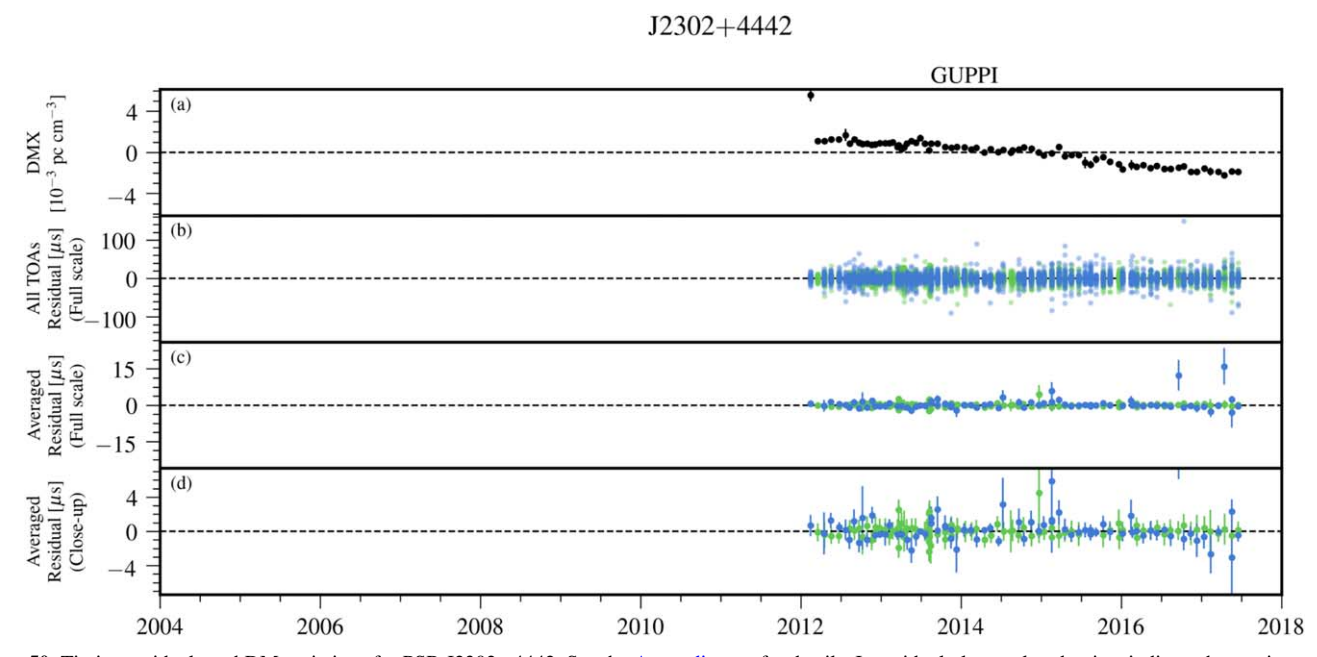


Figure 50. Timing residuals and DM variations for PSR J2302+4442. See the Appendix text for details. In residual plots, colored points indicate the receiver of each observation: 820 MHz (green) and 1.4 GHz (dark blue). (a) Variations in DMX. (b) Residual arrival times for all TOAs. Points are semitransparent; dark regions arise from the overlap of many points. (c), (d) Average residual arrival times shown full scale (panel c) and close-up of low residuals (panel d).

J2317+1439

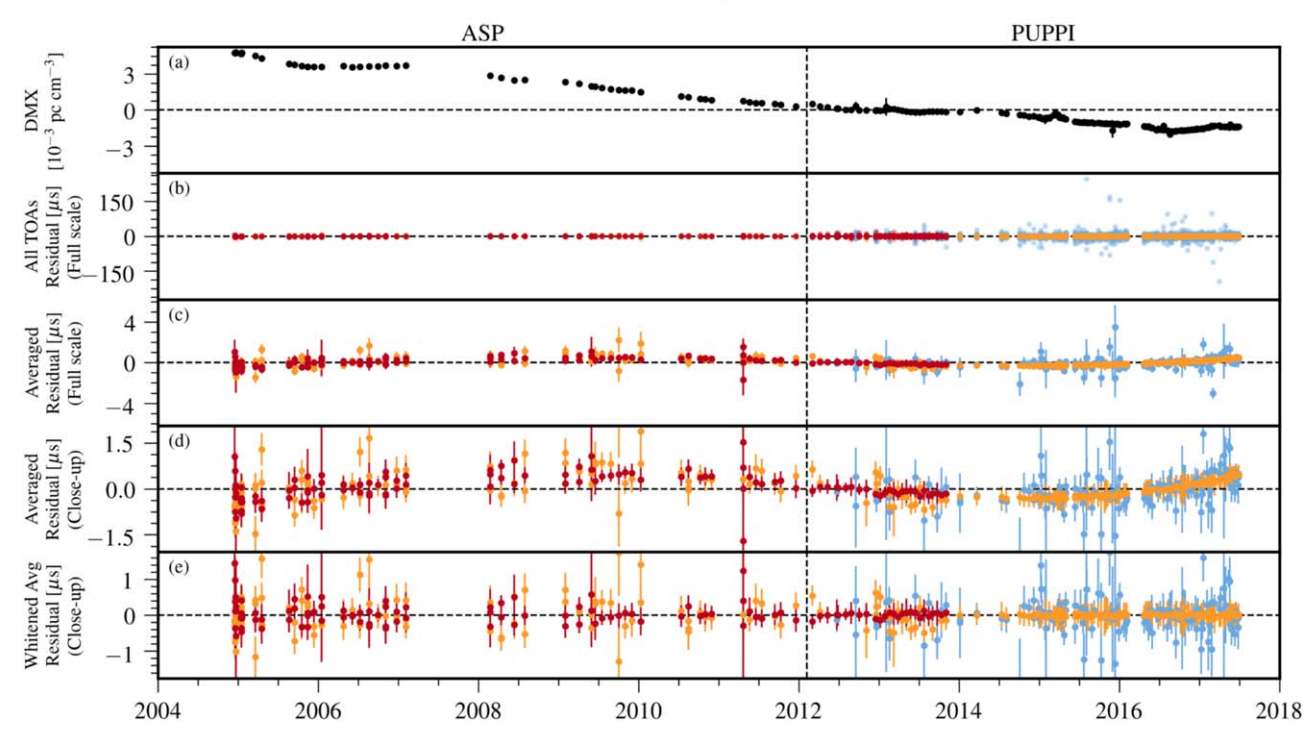


Figure 51. Timing residuals and DM variations for PSR J2317+1439. See the Appendix text for details. In residual plots, colored points indicate the receiver of each observation: 327 MHz (red), 430 MHz (orange), and 1.4 GHz (light blue). (a) Variations in DMX. (b) Residual arrival times for all TOAs. Points are semitransparent; dark regions arise from the overlap of many points. (c), (d) Average residual arrival times shown full scale (panel c) and close-up of low residuals (panel d). (e) Whitened average residual arrival times after removing the red-noise model (close-up of low residuals).

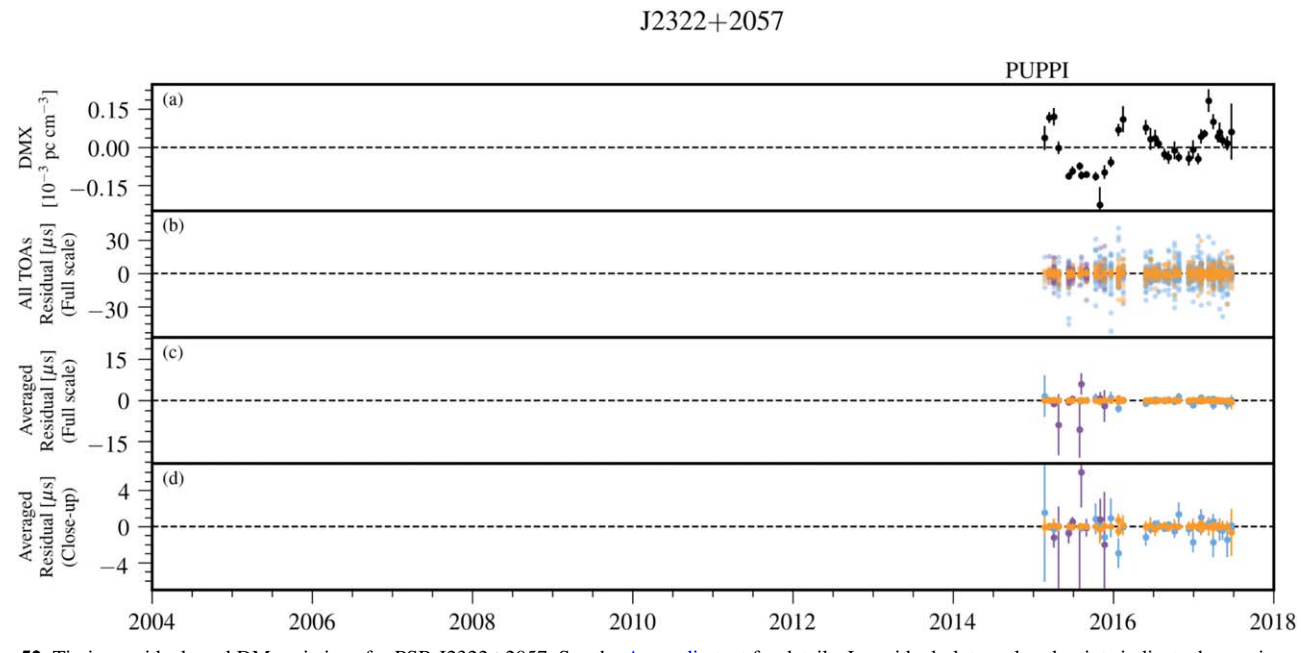


Figure 52. Timing residuals and DM variations for PSR J2322+2057. See the Appendix text for details. In residual plots, colored points indicate the receiver of each observation: 430 MHz (orange), 1.4 GHz (light blue), and 2.1 GHz (purple). (a) Variations in DMX. (b) Residual arrival times for all TOAs. Points are semitransparent; dark regions arise from the overlap of many points. (c), (d) Average residual arrival times shown full scale (panel c) and close-up of low residuals (panel d).

```
ORCID iDs
Md F. Alam https://orcid.org/0000-0003-2449-5426
Paul T. Baker https://orcid.org/0000-0003-2745-753X
Harsha Blumer https://orcid.org/0000-0003-4046-884X
Paul R. Brook https://orcid.org/0000-0003-3053-6538
Sarah Burke-Spolaor https://orcid.org/0000-0003-
4052-7838
Shami Chatterjee https://orcid.org/0000-0002-2878-1502
James M. Cordes https://orcid.org/0000-0002-4049-1882
Neil J. Cornish https://orcid.org/0000-0002-7435-0869
Fronefield Crawford https://orcid.org/0000-0002-
2578-0360
H. Thankful Cromartie https://orcid.org/0000-0002-
6039-692X
Megan E. DeCesar https://orcid.org/0000-0002-2185-1790
Paul B. Demorest https://orcid.org/0000-0002-6664-965X
Timothy Dolch  https://orcid.org/0000-0001-8885-6388
Robert D. Ferdman https://orcid.org/0000-0002-2223-1235
Elizabeth C. Ferrara https://orcid.org/0000-0001-7828-7708
William Fiore https://orcid.org/0000-0001-5645-5336
Emmanuel Fonseca https://orcid.org/0000-0001-8384-5049
Nathan Garver-Daniels https://orcid.org/0000-0001-
6166-9646
Peter A. Gentile https://orcid.org/0000-0001-8158-683X
Deborah C. Good https://orcid.org/0000-0003-1884-348X
Jordan A. Gusdorff https://orcid.org/0000-0001-6609-2997
Daniel Halmrast  https://orcid.org/0000-0003-2289-2575
Jeffrey S. Hazboun https://orcid.org/0000-0003-2742-3321
Ross J. Jennings https://orcid.org/0000-0003-1082-2342
Cody Jessup  https://orcid.org/0000-0002-4188-6827
Megan L. Jones https://orcid.org/0000-0001-6607-3710
Andrew R. Kaiser https://orcid.org/0000-0002-3654-980X
David L. Kaplan https://orcid.org/0000-0001-6295-2881
Luke Zoltan Kelley https://orcid.org/0000-0002-6625-6450
Joey Shapiro Key https://orcid.org/0000-0003-0123-7600
Michael T. Lam https://orcid.org/0000-0003-0721-651X
Duncan R. Lorimer https://orcid.org/0000-0003-1301-966X
Jing Luo https://orcid.org/0000-0001-5373-5914
Ryan S. Lynch https://orcid.org/0000-0001-5229-7430
Dustin R. Madison https://orcid.org/0000-0003-2285-0404
Maura A. McLaughlin https://orcid.org/0000-0001-
7697-7422
Chiara M. F. Mingarelli https://orcid.org/0000-0002-
4307-1322
Cherry Ng https://orcid.org/0000-0002-3616-5160
David J. Nice https://orcid.org/0000-0002-6709-2566
Timothy T. Pennucci https://orcid.org/0000-0001-
5465-2889
Nihan S. Pol https://orcid.org/0000-0002-8826-1285
Joshua Ramette https://orcid.org/0000-0002-4709-6236
Scott M. Ransom https://orcid.org/0000-0001-5799-9714
Paul S. Ray https://orcid.org/0000-0002-5297-5278
Brent J. Shapiro-Albert https://orcid.org/0000-0002-
Xavier Siemens https://orcid.org/0000-0002-7778-2990
```

```
Stephen R. Taylor https://orcid.org/0000-0003-0264-1453
Michael Tripepi https://orcid.org/0000-0002-4657-9826
Michael Vallisneri https://orcid.org/0000-0002-4162-0033
Sarah J. Vigeland https://orcid.org/0000-0003-4700-9072
Caitlin A. Witt https://orcid.org/0000-0002-6020-9274
Weiwei Zhu https://orcid.org/0000-0001-5105-4058
```

References

```
Aggarwal, K., Arzoumanian, Z., Baker, P. T., et al. 2019, ApJ, 880, 116
Aggarwal, K., Arzoumanian, Z., Baker, P. T., et al. 2020, ApJ, 889, 38
Alam, M. F., Arzoumanian, Z., Baker, P. T., et al. 2020, ApJS, 252, 5
Arzoumanian, Z., Baker, P. T., Blumer, H., et al. 2020, arXiv:2009.04496
Arzoumanian, Z., Baker, P. T., Brazier, A., et al. 2018a, ApJ, 859, 47
Arzoumanian, Z., Brazier, A., Burke-Spolaor, S., et al. 2014, ApJ, 794, 141
Arzoumanian, Z., Brazier, A., Burke-Spolaor, S., et al. 2015, ApJ, 813, 65
Arzoumanian, Z., Brazier, A., Burke-Spolaor, S., et al. 2018b, ApJS, 235, 37
Bak Nielsen, A.-S., Janssen, G. H., Shaifullah, G., et al. 2020, MNRAS,
  494, 2591
Barr, E. D., Freire, P. C. C., Kramer, M., et al. 2017, MNRAS, 465, 1711
Burke-Spolaor, S., Taylor, S. R., Charisi, M., et al. 2019, A&ARv, 27, 5
Cromartie, H. T., Fonseca, E., Ransom, S. M., et al. 2020, NatAs, 4, 72
Damour, T., & Deruelle, N. 1985, Ann. Inst. Henri Poincaré Phys. Théor.,
  43, 107
Damour, T., & Deruelle, N. 1986, Ann. Inst. Henri Poincaré Phys. Théor.,
   44, 263
Damour, T., & Taylor, J. H. 1992, PhRvD, 45, 1840
Deller, A. T., Goss, W. M., Brisken, W. F., et al. 2019, ApJ, 875, 100
Deller, A. T., Vigeland, S. J., Kaplan, D. L., et al. 2016, ApJ, 828, 8
Demorest, P. B. 2007, PhD Thesis, Univ. California, Berkeley
Demorest, P. B. 2018, nanopipe: Calibration and Data Reduction Pipeline for
   Pulsar Timing, Astrophysics Source Code Library, ascl:1803.004
Demorest, P. B., Ferdman, R. D., Gonzalez, M. E., et al. 2013, ApJ, 762, 94
Deneva, J. S., Ray, P. S., Lommen, A., et al. 2019, ApJ, 874, 160
Desvignes, G., Caballero, R. N., Lentati, L., et al. 2016, MNRAS, 458, 3341
Dickey, J. M. 1971, Ann. Math. Stat., 42, 204
Ding, H., Deller, A. T., Freire, P., et al. 2020, ApJ, 896, 85
DuPlain, R., Ransom, S., Demorest, P., et al. 2008, Proc. SPIE, 7019, 70191D
Ellis, J. A., Vallisneri, M., Taylor, S. R., & Baker, P. T. 2019, ENTERPRISE:
   Enhanced Numerical Toolbox Enabling a Robust PulsaR Inference SuitE
   v2.0, Astrophysics Source Code Library, ascl:1912.015
Ellis, J., & van Haasteren, R. 2017, jellis18/PTMCMCSampler: Official
   Release v1.0.0, Zenodo, doi:10.5281/zenodo.1037579
Fonseca, E., Pennucci, T. T., Ellis, J. A., et al. 2016, ApJ, 832, 167
Ford, J. M., Demorest, P., & Ransom, S. 2010, Proc. SPIE, 7740, 77400A
Frail, D. A., Jagannathan, P., Mooley, K. P., & Intema, H. T. 2016, ApJ,
   829, 119
Freire, P. C. C., & Wex, N. 2010, MNRAS, 409, 199
Gonzalez, M. E., Stairs, I. H., Ferdman, R. D., et al. 2011, ApJ, 743, 102
Hazboun, J. S., Simon, J., Taylor, S. R., et al. 2020, ApJ, 890, 108
Hobbs, G., Archibald, A., Arzoumanian, Z., et al. 2010, CQGra, 27, 084013
Hobbs, G., & Edwards, R. 2012, Tempo2: Pulsar Timing Package v2019.01.1,
   Astrophysics Source Code Library, ascl:1210.015
Hotan, A. W., van Straten, W., & Manchester, R. N. 2004, PASA, 21, 302
Hunter, J. D. 2007, CSE, 9, 90
Jones, M. L., McLaughlin, M. A., Lam, M. T., et al. 2017, ApJ, 841, 125
Kerr, M., Reardon, D. J., Hobbs, G., et al. 2020, PASA, 37, e020
Kopeikin, S. M. 1995, ApJL, 439, L5
Kopeikin, S. M. 1996, ApJL, 467, L93
Kramer, M., Xilouris, K. M., Lorimer, D. R., et al. 1998, ApJ, 501, 270
Kurosawa, N., Kobayashi, H., Maruyama, K., Sugawara, H., & Kobayashi, K.
                                  . I, 48, 261
Lam, M. T. 2017, PyPulse: PSRFITS handler, Astrophysics Source Code
  Library, ascl:1706.011
Lam, M. T., Cordes, J. M., Chatterjee, S., et al. 2016, ApJ, 819, 155
Lam, M. T., Ellis, J. A., Grillo, G., et al. 2018a, ApJ, 861, 132
Lam, M. T., McLaughlin, M. A., Arzoumanian, Z., et al. 2019, ApJ, 872, 193
Lam, M. T., McLaughlin, M. A., Cordes, J. M., Chatterjee, S., &
  Lazio, T. J. W. 2018b, ApJ, 861, 12
Lange, C., Camilo, F., Wex, N., et al. 2001, MNRAS, 326, 274
Lattimer, J. M. 2019, Univ, 5, 159
Liu, K., Desvignes, G., Cognard, I., et al. 2014, MNRAS, 443, 3752
Lorimer, D. R., Faulkner, A. J., Lyne, A. G., et al. 2006, MNRAS, 372,
```

```
Luo, J., Ransom, S., Demorest, P., et al. 2019, PINT: High-precision Pulsar Timing Analysis Package v0.5.7, Astrophysics Source Code Library, ascl:1902.007
Luo, J., Ransom, S. M., Demorest, P. B., et al. 2020, arXiv:2012.00074
Madison, D. R., Cordes, J. M., Arzoumanian, Z., et al. 2019, ApJ, 872, 150
Manchester, R. N., Hobbs, G. B., Teoh, A., & Hobbs, M. 2005, AJ, 129, 1993
Matthews, A. M., Nice, D. J., Fonseca, E., et al. 2016, ApJ, 818, 92
Nice, D., Demorest, P., Stairs, I., et al. 2015, Tempo: Pulsar Timing Data Analysis v13.000, Astrophysics Source Code Library, ascl:1509.002
Nice, D. J., & Taylor, J. H. 1995, ApJ, 441, 429
Osłowski, S., van Straten, W., Hobbs, G. B., Bailes, M., & Demorest, P. 2011, MNRAS, 418, 1258
Pennucci, T. T. 2019, ApJ, 871, 34
```

Pennucci, T. T., Demorest, P. B., & Ransom, S. M. 2014, ApJ, 790, 93Perera, B. B. P., DeCesar, M. E., Demorest, P. B., et al. 2019, MNRAS, 490, 4666

Perrodin, D., & Sesana, A. 2018, in The Physics and Astrophysics of Neutron Stars, ed. L. Rezzolla et al. (Cham: Springer), 95

Stars, ed. L. Rezzolla et al. (Cham: Springer), 95
Ransom, S., Brazier, A., Chatterjee, S., et al. 2019, BAAS, 51, 195
Ransom, S. M., Ray, P. S., Camilo, F., et al. 2011, ApJL, 727, L16
Reardon, D. J., Hobbs, G., Coles, W., et al. 2016, MNRAS, 455, 1751
Renevey, C. 2019, arXiv:1905.13720

Shaifullah, G. 2017, PhD thesis, Universität Bielefeld Shannon, R. M., Osłowski, S., Dai, S., et al. 2014, MNRAS, 443, 1463 Siemens, X., Ellis, J., Jenet, F., & Romano, J. D. 2013, CQGra, 30, 224015 Splaver, E. M., Nice, D. J., Stairs, I. H., Lommen, A. N., & Backer, D. C. 2005, ApJ, 620, 405

Stovall, K., Freire, P. C. C., Antoniadis, J., et al. 2019, ApJ, 870, 74
Stovall, K., Lynch, R. S., Ransom, S. M., et al. 2014, ApJ, 791, 67
Taylor, S. R., Vallisneri, M., Ellis, J. A., et al. 2016, ApJL, 819, L6
Vallisneri, M. 2020, libstempo: Python Wrapper for Tempo2 v2.3.4, Astrophysics Source Code Library, ascl:2002.017

Vallisneri, M., & van Haasteren, R. 2017, MNRAS, 466, 4954

van Haasteren, R. 2016, Piccard: Pulsar Timing Data Analysis Package v0.9-sp, Astrophysics Source Code Library, ascl:1610.001

van Straten, W., Demorest, P., Khoo, J., et al. 2011, PSRCHIVE: Development Library for the Analysis of Pulsar Astronomical Data v2012-12+, Astrophysics Source Code Library, ascl:1105.014

Verbiest, J. P. W., Bailes, M., Coles, W. A., et al. 2009, MNRAS, 400, 951
Verbiest, J. P. W., Weisberg, J. M., Chael, A. A., Lee, K. J., & Lorimer, D. R. 2012, ApJ, 755, 39

Wang, J. B., Coles, W. A., Hobbs, G., et al. 2017, MNRAS, 469, 425 Weisberg, J. M., & Huang, Y. 2016, ApJ, 829, 55